Fluorescence Study of the Microenvironment of Pyrene Molecules Loaded into Polycaprolactone-*block*-poly(ethylene oxide) Polymer Nanoparticles and Implications for Drug Delivery

by

Anupjot Singh Khokhar
B. Tech., Indian Institute of Technology Guwahati, 2018

A Thesis Submitted in Partial Fulfillment
of the Requirements for the Degree of

MASTER OF SCIENCE

in the Department of Chemistry

University of Victoria

Supervisory Committee

Fluorescence Study of the Microenvironment of Pyrene Molecules Loaded into Polycaprolactone-*block*-poly(ethylene oxide) Polymer Nanoparticles and Implications for Drug Delivery

by

Anupjot Singh Khokhar
B. Tech., Indian Institute of Technology Guwahati, 2018

Supervisory Committee

Dr. Matthew Moffitt, Department of Chemistry
Supervisor

Dr. Cornelia Bohne, Department of Chemistry
Department Member

Abstract

Supervisory Committee

Dr. Matthew Moffitt, Department of Chemistry
Supervisor

Dr. Cornelia Bohne, Department of Chemistry
Department Member

Polymer nanoparticles (PNPs) come across as the next generation drug delivery vehicles owing to their advantages such as biocompatibility, improved therapeutic efficacy and reduced toxicity. These biodegradable nanocarriers can encapsulate potent drugs and deliver them specifically to tumor cells with minimal effect on peripheral healthy tissues. In this thesis, we provide further understanding about how the microenvironment of the PNP core (polarity) which is a critical parameter for drug delivery properties, is affected by various chemical and structural features of the PNPs, including mean size, internal crystallinity, and drug loading. The role of interactions between encapsulated drugs and polymer nanoparticles is established by using a model hydrophobic probe such as pyrene (Py) which is sensitive to the polarity of the microenvironment and gives both qualitative and quantitative information in form of its fluorescence. We investigate the changing internal microenvironment of encapsulated hydrophobic molecules by applying a combination of chemical- and flow-based experimental variables to obtain a set of pyrene-loaded PNPs (Py-PNPs) with a wide range of properties, which are characterized using additional techniques, including dynamic light scattering (DLS), transmission electron microscopy (TEM), and powder x-ray diffraction (XRD).

We investigated specifically the effects of copolymer composition, initial Py:copolymer loading ratio, r_{Py}, on-chip water content, and microfluidic flow rate, Q on the structural properties of PNPs and pyrene fluorescence intensity ratios. For instance, the effect of initial Py:copolymer loading ratio, r_{Py}, showed some clear impacts of increasing loading ratio on the particle size and size distributions leading to decrease in particle size and increase in polydispersity. Moreover, changes in r_{Py} lead to non-monotonic changes both in encapsulation of pyrene and PNP microenvironment changes tracked by intensity ratios. In addition, these experiments went on to establish the relationship between the structural features of nanoparticles at the colloidal length scale (10 – 100 nm) to the molecular scale (partitioning, viscosity, diffusion) which we believe are critical for drug delivery properties of nanoparticles.

Table of Contents

List of Figures

List of Charts and Tables

Acknowledgements

I would like to express my sincere gratitude to my supervisor Dr. Matthew Moffitt for his encouraging support, extensive help and constant motivation throughout my graduate studies. His profound knowledge of science sparked discussions and feedback without which this thesis would not have been possible. I am very grateful to all things you have taught me. Thanks for bestowing me with such a wonderful opportunity to work on this project.

I would also give my thanks to my department committee member, Dr. Cornelia Bohne, for her constant help and encouragement. Thank you for all productive discussions and allowing me to use the Bohne facility while taking part in this collaborative project.

In addition, I would like to acknowledge NSERC PoND (Polymer Nanoparticles for Drug Delivery) and UVic Chemistry department for giving me this opportunity and constant funding support throughout.

My sincere thanks to my parents, sister and all my family members for their constant nurturing. I would also like to thank my friend Dr. Saksham Sharma for his research insights and extensive help.

Thanks to all my labmates in Moffitt group (current and past): Sun Kly, Talita de Francesco, Liza Silverman, Yuhang Huang for all the assitance, training and insightful suggestions. I would like to especially thank Talita for her help on acquiring all the TEM images. Besides, I would also like to thank my labmates in Bohne group, Jessy Oake, Ankur Awasthi, Guan Wang for training, help and suggestions throughout.

Last and definitely not least, I would like to thank all the faculty and staff in Chemistry department, thank you for your help and making workplace environment so wonderful.

Dedication

This thesis is dedicated to the Almighty and all my loved ones.

Chapter 1 Introduction

1.1. Background and Motivation

In recent years, there has been an increasing interest in designing and developing next-generation drug delivery vehicles that have improved therapeutic properties for biomedical applications.[1–4] Nanoparticles, in general, are colloidal drug delivery systems that are constructed from various materials including polymers, lipids, metals, inorganic, etc. and encapsulate therapeutic agent in nanosized particles.[5] Lipid-based nanoparticles became a commercially viable approach in encapsulating hydrophobic drugs and increasing their efficacy in aqueous environments.[6] However, polymer nanoparticles (PNPs) emerged as a robust delivery system that allowed ease of functionalization and broad diversity in chemical and structure properties.[7,8] PNPs have been successful in delivering many active pharmaceutical ingredients (API, such as potent drugs) to tumor cells both actively and passively.[9,10] PNPs gained further attention because of their ease of synthesis, biodegradability, controlled release, bioavailability and enhanced therapeutic efficiency of API.[11] A list of FDA approved drug-delivery materials includes poly(glycolactic acid), poly(caprolactone) and several other polymer materials used to produce nanoparticles.[11,12] The drug delivery applications of PNPs are dependent on their multiscale structure, size and morphologies. For instance, PNPs with sizes in range of 10 – 100 nm are found to be favorable for better biodistribution (via enhanced permeability and retention effect in tumors) and in-vivo circulation times.[9]

The self-assembly of amphiphilic block copolymers in aqueous media leads to formation of PNPs (sometimes called polymer micelles or micellar aggregates).[13,14] The self-assembly process is a thermodynamically spontaneous process that occurs when amphiphilic blocks dissolved in an organic solvent (such as THF, DMSO, DMF) are introduced to water above a critical concentration (termed as critical water content or cwc). Water drives the formation of PNPs as it is a non-solvent for hydrophobic blocks. This general strategy has been applied using different pathways for PNP synthesis, including direct dissolution in water, solvent exchange using dialysis, solvent evaporation and nanoprecipitation.[15] Nanoprecipitation involves fast mixing of a solution of copolymer in a polar organic solvent with water, usually by injecting the copolymer solution into an excess volume of water in a beaker or vial (bulk method).[15] Using the bulk nanoprecipitation method, PNP sizes and morphologies are largely determined by chemical parameters, including initial solvent type and copolymer concentration.

Microfluidics, or lab-on-a-chip, is defined as controlling fluid flow in a reactor where the volume ranges from 10^{-8} to 10^{-6} L with length scales ranging from 10^{-6} to 10^{-4} meters. Microfluidic approach to PNP preparation offers numerous advantages over other methods, including high-throughput screening of process parameters and formulation conditions, in addition to optimization of the properties of PNPs by varying physical or chemical variables during the synthesis. In our group, we have shown that improved control over the multiscale structure of PNPs along with their drug delivery characteristics (drug loading, release rates, in-vitro EC_{50} values, etc) is provided using on-chip nanoprecipitation followed by exposure to flow-tunable shear forces in a two-phase segmented microfluidic reactor.[16,17] Briefly, localized high-shear "hot spots" at the boundaries of gas-liquid and liquid-solid interfaces have been shown to provide "top-down" control of the size, morphology, internal crystallinity, and drug delivery properties of PNPs through simple changes in flow rate.[18,19] At the same time, additional "bottom-up" control over the properties of PNPs can be applied by varying chemical conditions such as hydrophobic block length, initial drug-to-copolymer ratio and water content.[20,21]

Fluorescent dyes have been deployed as model hydrophobic probes for the development of block copolymer and lipid-based nanocarriers. [22–25] It has been found that structural features of nanoparticles at the colloidal length scale (10 – 100 nm) and nanoscale (1 – 10 nm) are known to impact drug delivery properties of nanoparticles.[15,26–28] For instance, nanoparticle size and morphology (colloidal length scale) strongly influence biodistribution via enhanced permeability and retention effect in tumors and circulation time.[15,26,27] On the other hand, internal crystallinity (nanoscale) of nanoparticles plays a critical role in drug release, stability, and flexibility.[15,28] The effects of structural features of nanoparticles on the local environment of drug molecules can be probed by utilizing the photophysical properties of dyes, since they can serve as hydrophobic surrogates of encapsulated drugs and are sensitive to the changing confined microenvironment characteristics (such as polarity, microviscosity, diffusion, binding affinity).[29,30]

The objective of this thesis is to provide further understanding about how the microenvironment of the PNP core (polarity) is affected by various chemical and structural features of the PNPs, including mean size, internal crystallinity, and drug loading. To this end, we use the dye pyrene as a surrogate for an encapsulated hydrophobic drug, and measure the fluorescence properties of the dye in various samples of pyrene-loaded polycaprolactone-*block*-poly(ethylene oxide) (PCL-*b*-PEO) PNPs (Py-PNPs) prepared using a two-phase gas-liquid microfluidic reactor. We apply a combination of chemical- and flow-based experimental variables to obtain a set of Py-PNPs with a wide range of properties, which are characterized using additional techniques, including dynamic light scattering (DLS), transmission electron microscopy (TEM), and powder x-ray diffraction (XRD). We then monitor changes in the fluorescence properties of pyrene to detect changes in the microenvironment of encapsulated pyrene in PNPs (Py-PNPs) that arise due to changes in experimental variables. Finally, using our complete dataset, we analyze the effects of three key physicochemical PNP characteristics (hydrodynamic size, dye or drug loading, and internal crystallinity) on the microenvironment of encapsulated molecules. This information should be useful in better understanding the location and environment of encapsulated molecules within PNP cores, properties directly related to the diffusion and release of molecules from the core. Therefore, this study could provide a road map for preparing PNPs with improved drug delivery properties.[31]

1.2. Block copolymers

1.2.1. Basic Concepts of Polymers

Polymers are macromolecules formed as a result of covalent bonding of many repeating small molecules.[32] These repeating units, also known as monomers, assemble to form long chains. In some cases, these chains possess branches or cross-links between chains, depending on the type and function of the polymer. The reaction that forms a polymer chain from its constituent monomers is known as polymerization. The degree of polymerization is defined as the number of repeat units in a polymer chain.[32] Polymerization reactions are statistical processes which generally lead to a distribution of chains with different numbers of repeat units. Therefore the degree of polymerization for a polymer sample is an average value obtained by averaging over all chains in the sample.[32] Different types of averages for polymer samples are described below.

Polymers can be classified into three categories depending on the connectivity of the polymer chains: linear, branched or cross-linked. Linear polymers are polymers which have linear polymer chains with no side chains attached and hence have high packing density, for instance, high-density polyethylene (Figure 1-1). Branched polymers have side chains attached to the polymer chain, for instance, low-density polyethylene (Figure 1-1).[32] A polymer having multiple side chains covalently attached to polymer chain is a cross-linked polymer, for example, vulcanised rubber (Figure 1-1).[32]

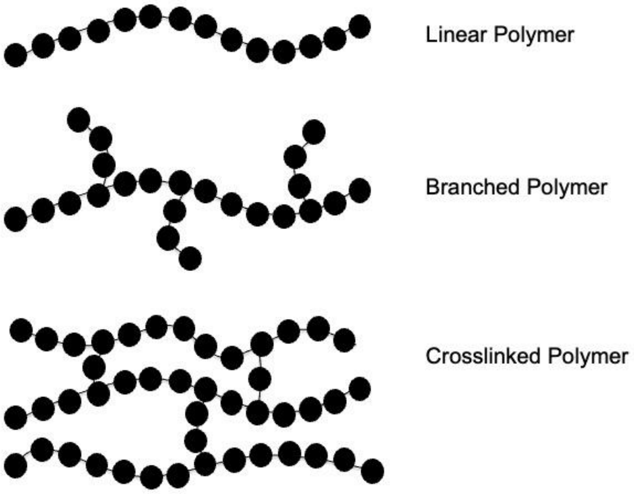

Figure 1-1. Different polymer structures based on connectivity of repeat units (black spheres)

Polymers, in general, are big molecules containing many repeat units and hence are also referred to as macromolecules. There is no generally accepted definition of the size of a polymer, but they are usually molecules made up of at least ~100 repeat units. Due to their large size, polymers do not crystallize completely below their melting temperature, and so often possess both crystalline and amorphous regions (i.e. they are semicrystalline). The crystalline regions in these polymers provide strength and hardness to the structure whereas the amorphous regions provide flexibility to the structure.[32] The thermodynamics and kinetics of crystalline and amorphous regions are described in detail in section 1.2.2.

When a polymer consists of a single type of repeat unit, it is called a homopolymer. If the polymer chains consist of two or more different types of repeat units, it is called a copolymer. Copolymers can be further classified into four main categories based on the arrangement of the different types of repeat units within the chain of the copolymer as displayed in Figure 1-2.[32]

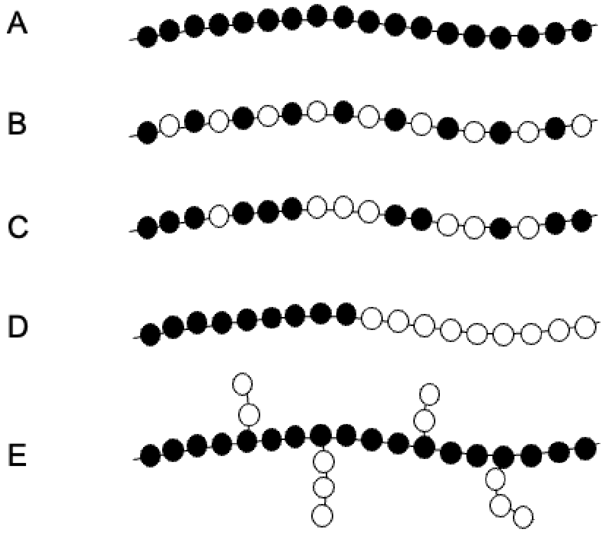

Figure 1-2. Schematic illustration of (A) homopolymers, (B) alternating copolymers, (C) random copolymers, (D) block copolymers, and (E) graft copolymers. Black and white spheres represent two different monomeric units.

These are random (or statistical) copolymers, alternating copolymers, graft copolymers and block copolymers. Random copolymers are characterized by a random distribution of repeat units in the polymer chain.[32] Alternating copolymers are identified with an alternating arrangement of the two different types of repeat units along the polymer chain, such that the mole fraction of both repeat units is ~50%.[32] Graft copolymers are branched polymers in which branches of the copolymer consist of a different type of repeat unit than the backbone chain.[33] Block copolymers are an interesting class of copolymers, with a sequence or block of one type of repeat unit covalently bonded to a block of another type of repeat unit. Block copolymers can have two or more blocks making up the copolymer chain; if only two blocks are present, the block copolymer is referred to as a diblock copolymer.[32] Diblock copolymers are of primary interest within this thesis.

As mentioned above, polymerization reactions lead to a distribution of chain lengths, or degrees of polymerization. Therefore polymer samples possess a distribution of molecular weights, rather than the single molecular weight used to describe most small molecule compounds. For this reason, the molar mass or molecular weight used to describe a polymer is an average of the distribution.[32] There are two types of averages used to describe the molecular weight of a polymer. The number-average molecular weight, M_n, is defined as:

$$M_n = \frac{\sum_i N_i M_i}{\sum_i N_i}$$

where N_i represents the number of chains in a polymer fraction i with molecular weight of M_i. The number average molecular weight is measured by methods that are sensitive to the number of chains in solution, including colligative methods such as osmotic pressure, boiling point elevation, lowering of vapour pressure, and depression of freezing point.[32]

The weight-average molecular weight, M_w, is defined as:

$$M_w = \frac{\sum_i w_i M_i}{\sum_i w_i}$$

where w_i represents the weight or mass of a polymer fraction i with molecular weight of M_i. Since the weight of a fraction can be described using: $w_i = N_i M_i$, M_w can also be written:

$$M_w = \frac{\sum_i N_i M_i^2}{\sum_i N_i M_i}$$

As an average value, M_w is more sensitive to longer chains in the distribution than M_n, and is always a higher number than M_n (Figure 1-3). M_w is determined using methods that are sensitive to the size of molecules in solution, including static light scattering.[32]

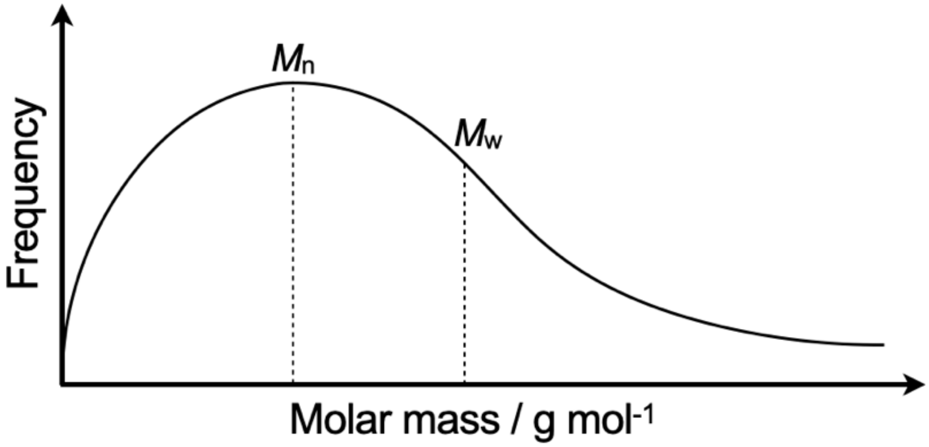

Figure 1-3. Theoretical molecular weight distribution of a polymer sample highlighting the positions of different molecular weight averages.

If all chains in a polymer sample are the same size, then (and only then) the sample is described a monodisperse. For a monodisperse sample, M_w is equal to $M_{n,}$. However, as discussed above, all real synthetic polymer samples possess a distribution of chain sizes.[32] The distribution width, or dispersity, of a sample can be defined:

$$Đ = \frac{M_w}{M_n}$$

1.2.2. Self-Assembly of Block Copolymers

Block copolymers are generally amphiphilic in nature i.e., contain both hydrophobic and hydrophilic segments. The spontaneous self-assembly of amphiphilic block copolymers in aqueous medium under certain conditions is driven by the system minimizing unfavorable interactions between the hydrophobic blocks and the surrounding water, while maximizing favorable interactions between hydrophobic blocks via intra/intermolecular association. The result of the self-assembly process is a block copolymer micelle, or PNP, made up of multiple block copolymer chains and possessing a core consisting of hydrophobic blocks and a surrounding corona of hydrophilic blocks extending into the aqueous medium (Figure 1-4).[32]

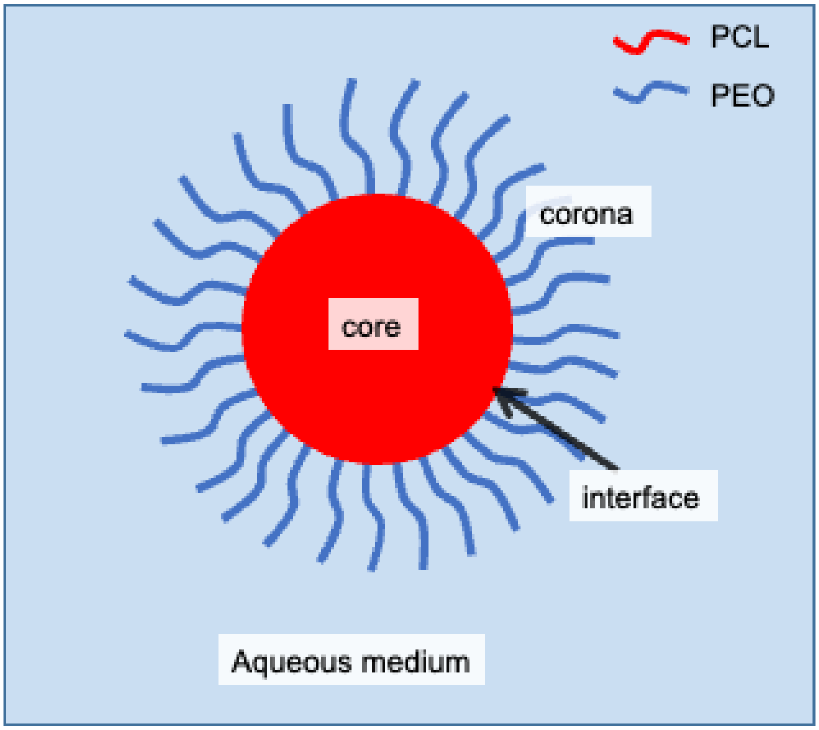

Figure 1-4. Schematics of a block copolymer micelle or PNP in an aqueous medium.

The spontaneous self-assembly of block copolymers in water has been a focus in producing more effective drug-delivery carriers.[12] The structure of a drug-delivery PNP in aqueous medium consists of three main regions: the core, the corona and interface between core and corona (Figure 1-4). The core consists of hydrophobic blocks which act as a microenvironment for encapsulated hydrophobic drugs; if the hydrophobic blocks are semicrystalline, the core may be further divided into amorphous and crystalline regions

(Figure 1-5). The thermodynamics and kinetics of amorphous and crystalline regions of polymer is described in section 1.2.4. The PNP corona consists of hydrophilic segments that extend into the aqueous medium forming the outer shell. The interfacial region is the area containing the linkages between the hydrophobic and hydrophilic blocks. Theories of micelle formation have been suggested by a number of researchers previously and these theories suggest that the interface region is very sharp in star-like micelles, i.e., the interface thickness is assumed to be negligible in comparison with the diameter of PNP core.[34] During micellization, the interfacial region formation is achieved in a way to minimize the surface energy and this has been shown by some micellar structure models to be possible by grafting arrangements of core and corona polymer blocks at the interface.[35] On the contrary, Monte Carlo simulations for modelling micellar structures have demonstrated that the interfacial region of micelle is more diffuse than sharp.[34]

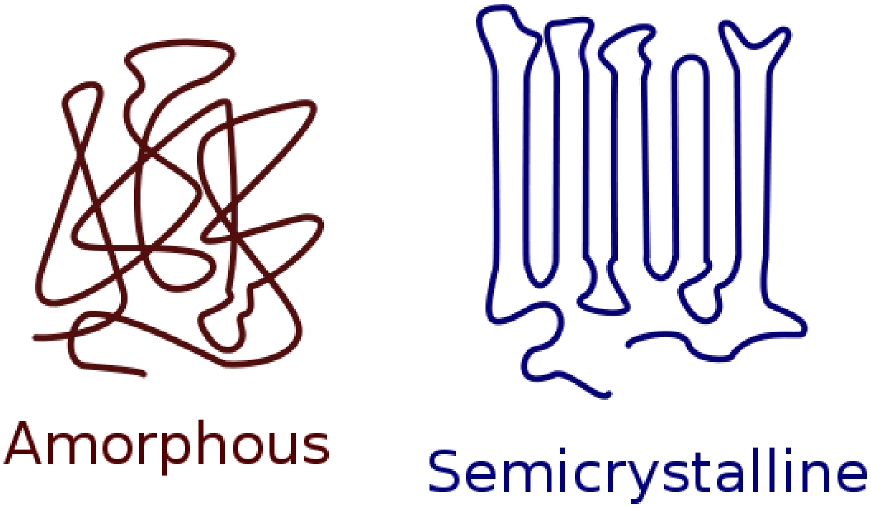

Figure 1-5. Schematic illustration of an amorphous and semicrystalline polymer.[36]

The most common morphology observed for PNPs are spheres, but other morphologies are possible, depending on multiple experimental conditions, including cylinders, lamellae, vesicles etc. A TEM figure showing multiple morphologies of a prepared Py-PNPs sample is shown in Figure 1-6.

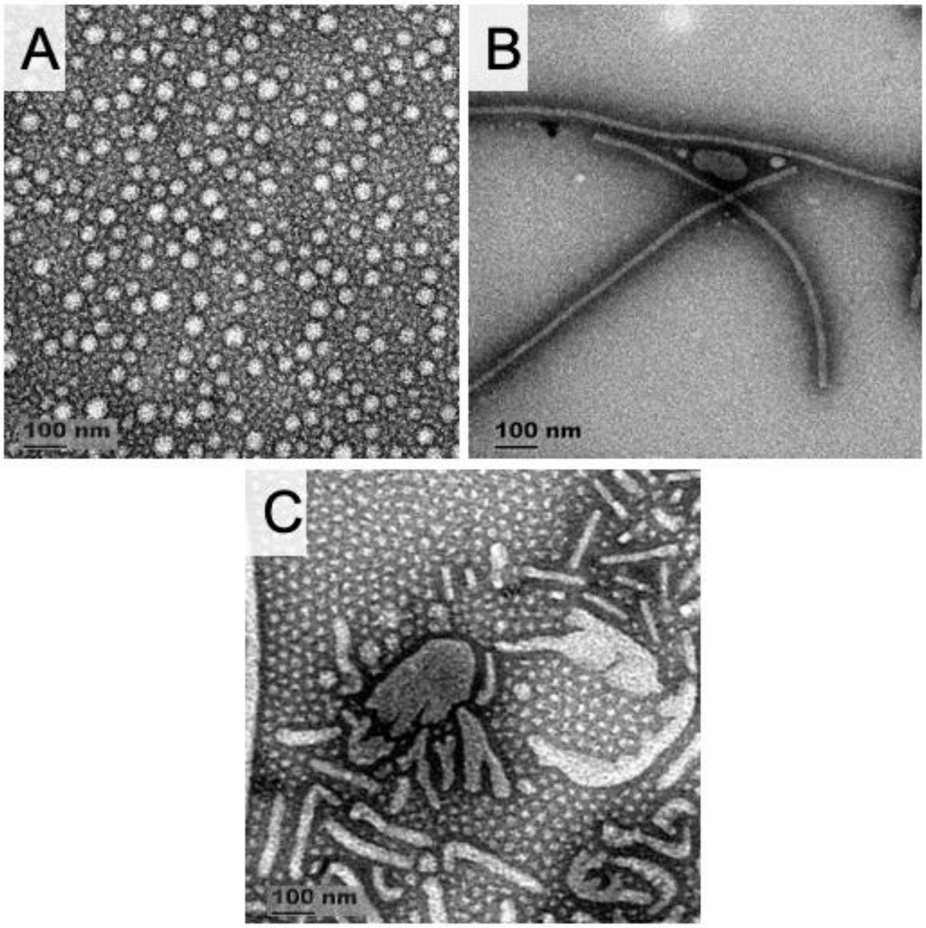

Figure 1-6. Representative TEM images from the current work showing different morphologies for PNPs: (a) spheres, (b) cylinders and (c) mixture of lamellae and cylindrical micellar structures. All these samples were prepared using $PCL_{2.1k}$-*b*-PEO_{5k} block copolymer under different microfluidic flow rates. All scale bars are 100 nm.

1.2.3. Thermodynamics of Self-Assembly

Block copolymers in solution can exists as single chains or self-assembled nanoparticles depending on the experimental conditions, including nature of the solvent, copolymer concentration, and temperature.[37] For any system, the free energy (G) depends on two terms, entropy (S) and enthalpy (H), according to the definition of G: [38]

$$G = H - TS$$

where T is the temperature of the system. At constant temperature, the change in free energy (ΔG) for a process is described: [38]

$$\Delta G = \Delta H - \mathrm{T}\Delta S$$

For a process to be spontaneous at constant pressure (p) and temperature, ΔG must be negative:

$$\Delta G < 0 \text{ condition for spontaneity, constant } p \text{ and } T$$

Under certain conditions, ΔG for the self-assembly process (single chains forming PNPs) will be negative, resulting from either negative ΔH, positive ΔS, or a combination of both. There are several factors that determine the overall sign of ΔH and ΔS and therefore the spontaneity of self-assembly.[37] The self-assembly of block copolymers gives rise to microphase separation between covalently attached hydrophilic and hydrophobic blocks.[33,34] ΔH of this microphase separation is generally negative because of the decrease in unfavorable interactions between hydrophobic blocks and water and increase in favorable interactions between self-assembled hydrophobic blocks.[37] However, this change will also have a smaller, positive ΔH contribution, arising from increased repulsive interactions between close-packed solubilized hydrophilic chains within the PNP corona.[37] ΔS of self-assembly can also have positive and negative contributions. The most important negative ΔS contribution is the loss of conformation entropy associated with the stretching of hydrophobic blocks due to steric interactions arising from close-packing at the core-corona interface.[37,38] However, self-assembly of block copolymers in water will also give rise to a positive ΔS contribution, due to a decrease in the structuring of water around the hydrophobic blocks as they segregate into the PNP core.

Overall, the formation of PNPs arising from the balance of enthalpic and entropic contributions will be spontaneous above a critical concentration of copolymer (critical micelle concentration, or cmc) and above a critical water content (cwc) in a solvent system containing a mixture of polar organic solvent and water.[37] Under these conditions, PNPs can be formed that can encapsulate hydrophobic drugs and have effective drug delivery properties owing to their size, morphologies and drug release.

1.2.4. Crystallization of Semicrystalline Polymers

The block copolymer used in this study possesses a hydrophobic block (PCL) that is semicrystalline in nature and due to this the hydrophobic PNP cores formed are comprised of both ordered crystalline and non-ordered amorphous regions.[39,40] Although PEO is also a semicrystalline polymer, crystalline and amorphous regions are identified only within the core of PNPs, since the corona block (PEO) is solubilized in aqueous medium which prevents its crystallization.[39,40] Crystalline regions consist of small, locally ordered and closed packed arrangements of core forming blocks.[39,40] On the other hand, amorphous regions are random arrangement of disordered chains that are kinetically frozen (Figure 1-5).[39,41]

Polymer crystallization is a process of phase transformation involving disordered polymer chains (or amorphous state) to ordering of polymer chains into close-packed arrangements. In this case, the change in free energy is denoted by $\Delta G_{\text{crystal}}$, which depends on two state functions: change in enthalpy ($\Delta H_{\text{crystal}}$) and entropy ($\Delta S_{\text{crystal}}$). During the process of ordering of chains, there is a decrease in internal energy due to phase changes resulting in release of energy to the surroundings.[38,39,41] Thus, $\Delta H_{\text{crystal}}$ is negative but has a small value due to weak intermolecular interactions (Van der waal) between packed chains.[38,39,41] $\Delta S_{\text{crystal}}$ also has a negative contribution due to large conformational entropy change during the ordering of polymer chains.[38,39,41] At a high temperature, $\Delta S_{\text{crystal}}$ contribution to free energy change makes the crystallization process unfavourable ($\Delta G_{\text{crys}} > 0$). However, below the melting point of polymer (T_m) polymer crystallization is favourable because the negative enthalpy contribution to the free energy of crystallization is sufficiently large.

Polymer crystallization is generally the slowest process of phase transformation, where the rate of transformation is the rate-determining step.[42] This is the reason that polymer chains do not have enough mobility to allow crystallite growth in the experimental time scale. [42] Polymer chains during crystallization process align at specific distances from each other to form nuclei (nucleation) and then these parallel arrays are further packed to form a three-dimensional ordered structure (growth).[39]

Amorphous state of polymers is the disordered polymer chain state which is further classified into two different kinetic states depending upon the temperature of system: the rubbery/viscous state and the glassy state.[41] Above the glass transition temperature (T_g), disordered polymer chains are highly dynamic and can dissipate the stress applied on it by conformational changes of chains.[41] On the other hand, below the T_g, disordered polymer chains are kinetically frozen and cannot change conformation under applied stress.[41] In case of nanoparticles formed from semicrystalline block copolymers, only viscous state amorphous regions are identified as T_g for semicrystalline block copolymers is quite low resulting in amorphous polymer chains being highly dynamic.

1.3. Pyrene

1.3.1. Introduction to Fluorescence

Photophysical processes such as absorption, fluorescence, and phosphorescence, occur when a molecule either gains energy by absorbing an incoming photon, or loses energy by releasing heat or emitting a photon.[43] There are molecular energy transitions involved in a photophysical process, which can be divided into two categories: 1. radiative transitions are processes that involve emission of photons after light absorption, and 2. non-radiative transitions are processes that do not involve emission of photons after light absorption, and include dissipation of energy in the form of heat during the deactivation of an excited state molecule. Specifically, absorption (A), fluorescence (F) and phosphorescence (P) are the possible radiative transitions. Internal conversion (IC), intersystem crossing (ISC) and vibrational relaxation (VR) are the possible non-radiative transitions.[43] All the different photophysical processes are illustrated using a Jablonski diagram as shown in the Figure 1-7.

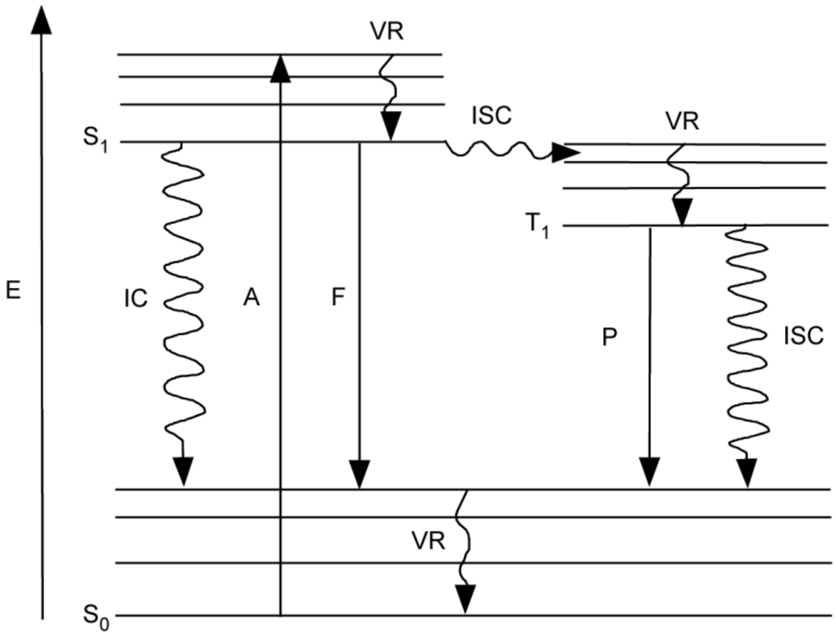

Figure 1-7. Illustrative Jablonski diagram depicting radiative (straight) and non-radiative (curled) transitions for an excited state molecule. E, S_0, S_1 and T_1 represent the energy, ground state, singlet excited state, triplet excited state respectively.

Absorption occurs when a molecule absorbs energy of an incoming photon, and the molecule is excited from the stable ground state to one of its electronic excited states. The excited state molecule is unstable due to its higher internal energy and therefore the molecule relaxes to return to its ground state using a deactivation mechanism involving either a radiative or non-radiative transition. Fluorescence is a radiative transition between electronic states with the same electronic spin, such either a transition from singlet (S) excited state to singlet ground state or triplet (T) excited state to triplet ground state.[43] Radiative deactivation pathways follow first-order reaction kinetics and there is competition between multiple deactivation pathways when an excited state molecule returns to the ground state.[43]

1.3.2. Pyrene as a Fluorescent Probe

Pyrene (Py) is a polyaromatic hydrocarbon (PAH) with excellent photophysical properties such as significant fluorescence lifetimes (190 ns in polar solvent and 650 ns in non-polar solvent)[44] and exceptional fluorescence quantum yield (0.65 in non-polar solvent and 0.72 in polar solvent).[44] These photophysical properties have been utilized extensively in fluorescent probe studies of many nanostructured systems.[9,23,25,45–48] For example, J. Zhao et al., studied the effect of chemical variables such as copolymer concentration and solvent composition (H_2O/DMF mixture) on the partition coefficient of pyrene in highly asymmetric block copolymers of polystyrene-*b*-polyacrylic acid using pyrene fluorescence intensity ratios.[48] Another instance, G. S. Kwon, et al., used pyrene as a model drug and fluorescent probe to study distribution of hydrophobic molecules into micelle cores and in their study pyrene incorporated in poly(β–benzyl-L-aspartate)-*b*-poly(ethylene oxide) (PBLA-*b*-PEO) had I_1/I_3 ratio of about 1.4 indicating a non-polar PBLA core.[47] These studies show that pyrene is an effective surrogate molecule for investigating prospective drug delivery systems. [9,23,25,45–48]

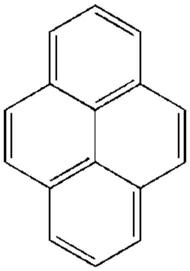

Chart 1-1. Chemical structure of pyrene.

1.3.3. Steady-State Fluorescence Emission of Pyrene

The steady-state emission spectrum of Py is very sensitive to the microenvironment surrounding the pyrene molecules and therefore fluorescence intensity ratios of different peaks in the spectrum can be quantitatively related to the properties of the local environment experienced by pyrene.[45,49,50] A typical fluorescence spectrum of pyrene exhibits several emission bands between 365 nm and 420 nm as indicated in Figure 1-8. The transition corresponding to the first fluorescence band (I_1, 373 nm), which is also the 0-0 transition of pyrene, is very weak in organic solvents, but is significantly stronger in more polar solvents, which explains the sensitivity of the I_1/I_3 ratio to solvent polarity, taking a value of 0.58 in hexane or 1.87 in water.[45,50,51] It is important to note that the third emission peak (I_3, 383 nm) is not sensitive to the microenvironment changes and thus serves as an internal standard for pyrene fluorescence. The fluorescence intensity ratio I_1/I_3 is an indicator of the sensitivity of pyrene molecules to the polarity of the microenvironment and this method has been used to understand the microenvironment of loaded pyrene in Py-PNPs.[45]

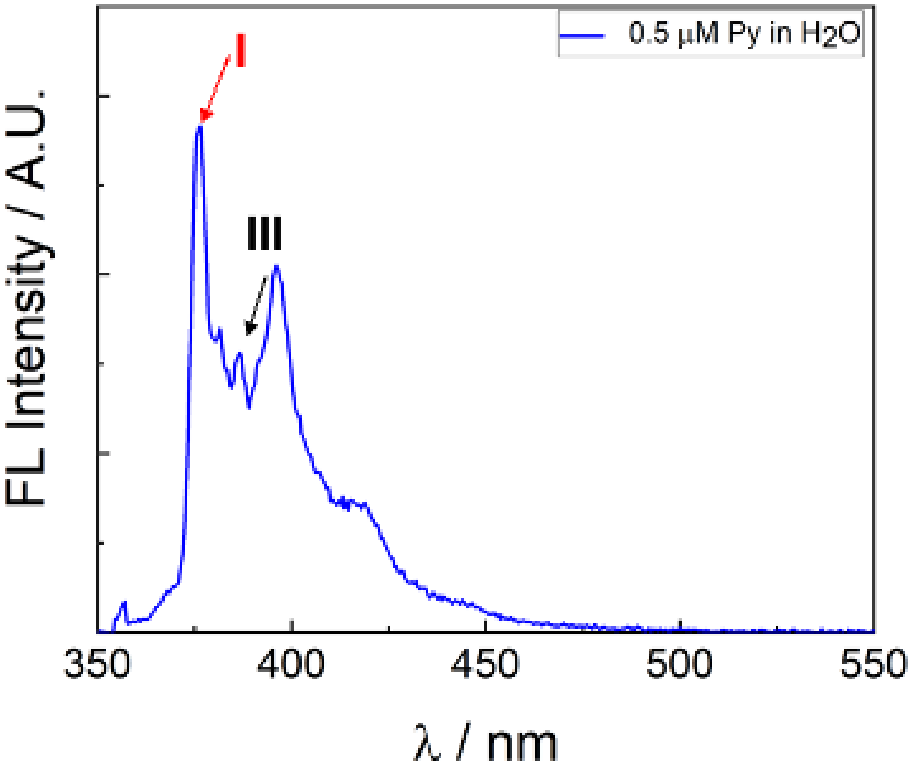

Figure 1-8. Fluorescence spectrum of 0.5 μM pyrene solution in water indicating the first (I_1, red) and third emission peak (I_3, black).

Another unique feature of steady-state spectrum of pyrene is monitoring the formation of excimer. An excimer (E^*) of pyrene is a complex formed from the association of a ground state pyrene (M) with singlet excited state pyrene (M^*) as illustrated in Figure 1-9.[52] The formation of pyrene excimers were first observed by Förster and Kasper when they studied the dependence of pyrene emission on the concentration of pyrene solutions.[52] Similar phenomena were observed for many other aromatic hydrocarbons including pyrene derivatives in solution.[53] The kinetics of excimer formation process is shown in the Figure 1-9, where τ_M and τ_E are the lifetimes associated with the pyrene monomer and excimer respectively.

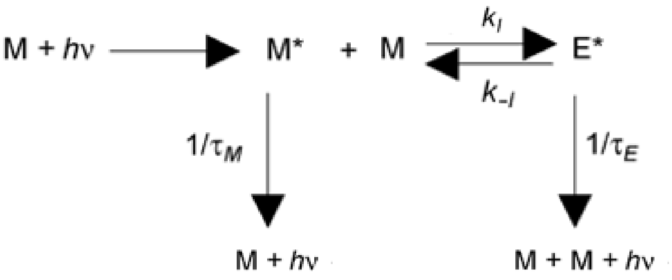

Figure 1-9. Mechanism of monomer and excimer formation for pyrene and their decay pathways.[53]

The excimer formation appears as a structureless band in fluorescence spectrum of pyrene in the green wavelength region (~480 nm) as shown in Figure 1-10. In this thesis, the pyrene excimer formation comes from the loaded pyrene molecules in the PNPs during the self-assembly process. This ability of pyrene allows one to probe the dynamics experienced by the pyrene dye inside the hydrophobic microdomains using time-resolved fluorescence and fluorescence quenching, although these techniques will not be applied in this thesis. The formation of excimer of loaded pyrene in Py-PNPs can be monitored using the fluorescent intensity ratios I_E/I_M, which represents the ratio of the fluorescence intensity of the excimer over that of the monomer (same as I_3) shown in Figure 1-10. Thus, steady-state emission of pyrene yields two fluorescence intensity ratios, namely the I_E/I_M and I_1/I_3 ratios that provide different information about the local environment of pyrene (Figure 1-8).

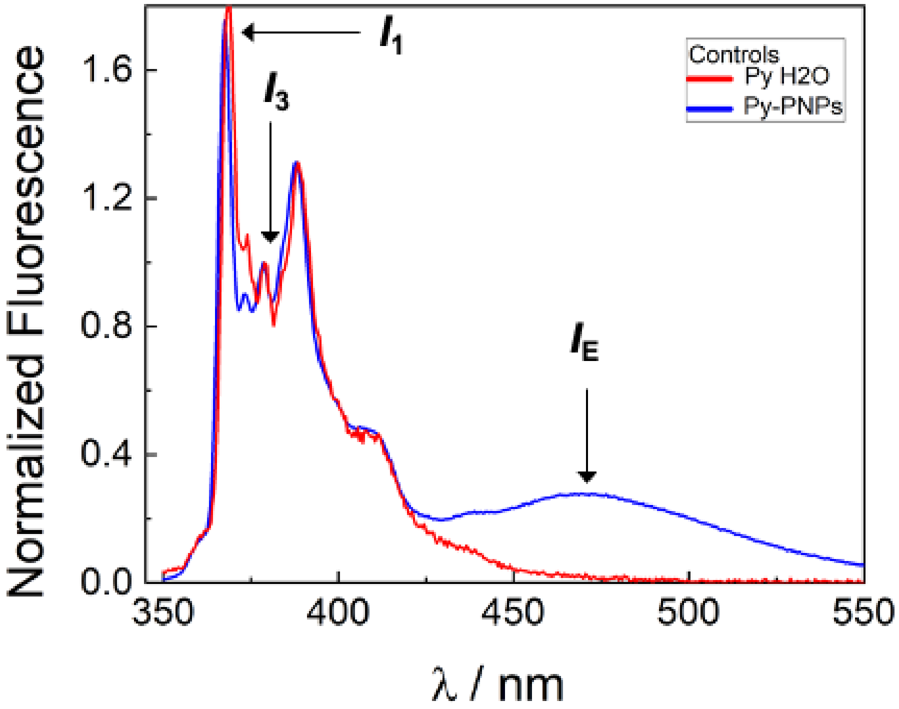

Figure 1-10. Fluorescence spectrum of 0.5 μM pyrene solution in water (red) and 0.5 μM loaded pyrene in Py-PNPs; showing the formation of excimer and indicating the important peaks for fluorescence intensity ratios.

1.4. Microfluidic Synthesis of Py-PNPs

1.4.1. Basics of Microfluidics

The earliest microfluidic devices demonstrated that fluidic components could be miniaturized and integrated together, leading to the idea that one could fit an entire "lab on a chip".[54] Microfluidics deals with flows within structures with at least one dimension < 1000 μm.[54] In this regime, fluid dynamics are vastly different from the macroscale, thus offering small reagent volumes, precise control over flow dynamics (laminar flow), continuous flow operation, increased control over mixing and local reagent volumes.[55] Flow dynamics on different length scales can be assessed by the dimensionless Reynolds number (*Re*). The Reynolds number is a measure of the ratio of inertial forces to viscous forces and can be defined as:

$$Re = \frac{\rho U d_h}{\mu}$$

where ρ is the fluid density, U is characteristic fluid velocity, d_h is the characteristic channel length, and μ is the dynamic viscosity of the fluid. Due to small channel dimensions, microfluidic flow is laminar in nature, characterized by Reynolds numbers that are typically ≤ 1, whereas macroscale laminar flow is characterized by Re > 1.[56]

1.4.2. Microfluidic Manufacturing of PNPs

While single phase reactors have been widely employed in material synthesis, multiphase microfluidic reactors have been attracting increased attention in material synthesis.[55–57] In single phase reactors, mixing is slow due to the absence of turbulence and generating turbulence in microchannels requires extremely high flow rates (~10 ms^{-1}) such that microfluidic flow is generally laminar in nature. Reaching such flow rates requires undesirably high reagent consumption and high pressure.[55] In addition, the cross-stream variation in flow velocity, characteristic of pressure-driven flow, results in a wide variance of residence time (broadened residence time distribution) and increased polydispersity in material synthesis in general. These two problems can be eliminated by introducing a second immiscible stream of fluid (gas 25 or liquid) into the system such that the immiscible interface results in the generation of a succession of immiscible fluid segments.[55,56] Multiphase microfluidic reactors in general can be divided into two types: droplet reactors (liquid-liquid flow) and gas-liquid segmented reactors.[55] In droplet reactors, discrete liquid droplets are encapsulated by a carrier fluid that wets the microchannel. The relative interfacial tension of the fluids with the channel surface determines which fluid which will be the major phase (continuous phase) and which fluid will be the minor phase (dispersed phase).[56] The phase that has higher interfacial tension with the channel wall, i.e., the less wetting phase, will form droplets or bubbles. The sizes of droplets or bubbles formed with respective to the continuous phase are primarily a function of flow rates. The reagents in the case of droplet reactors are compartmentalized within the nanoliter-sized droplets and do not come into contact with the channel surface and are transported through the channel without dispersion. In the gas-liquid segmented reactor, the liquid "plugs" are the continuous phase and are separated by discrete gas bubbles.[17,57] In this case, reactions occur in the continuous phase, and the liquid plugs are connected by a thin liquid film surrounding the gas (dispersed) phase.[18]

The two-phase microfluidic reactor used in this thesis is shown in Figure 1-10.[17–19,31] One of the four inlets is used to inject argon while the other three are used as the inlets for the polymer/drug solution, solvent DMF and solvent-water mixture solution. Then after the four streams join together, the regular gas stream mixes with the liquid stream and forms gas and liquid segments. Then the inlets are followed by a 100 mm long mixing channel. The mixing channel has a sinusoidal shape and is 100 µm wide, 100 mm long and 150 µm deep. After that, a mixture of gas and liquid flows through the processing channel which also has a sinusoidal shape. The processing channel is wider and longer than the mixing channel with a width of 200 µm and a length of 740 mm.

The advantage of using two-phase microfluidic reactor is the enhanced mixing generated by the recirculation of a pair of counter-rotating vortices in the top and bottom halves of the droplets or liquid "plugs".[17,18] Another advantage that is unique to two-phase gas-liquid microfluidic reactors is the high shear 'hot-spots' in the corners of the gas-liquid interface.[18] Using the same microfluidic platform our group has shown that microfluidic preparation of PAX-loaded PCL-*b*-PEO nanoparticles improved PAX loading efficiencies (up to 90%) and slowed in vitro release kinetics compared to a conventional bulk preparation.[18] Moreover, control of multiscale structure enabled tailoring of drug delivery nanoparticle function, as demonstrated by tuning of PAX release rates via on-chip flow rate.[18]

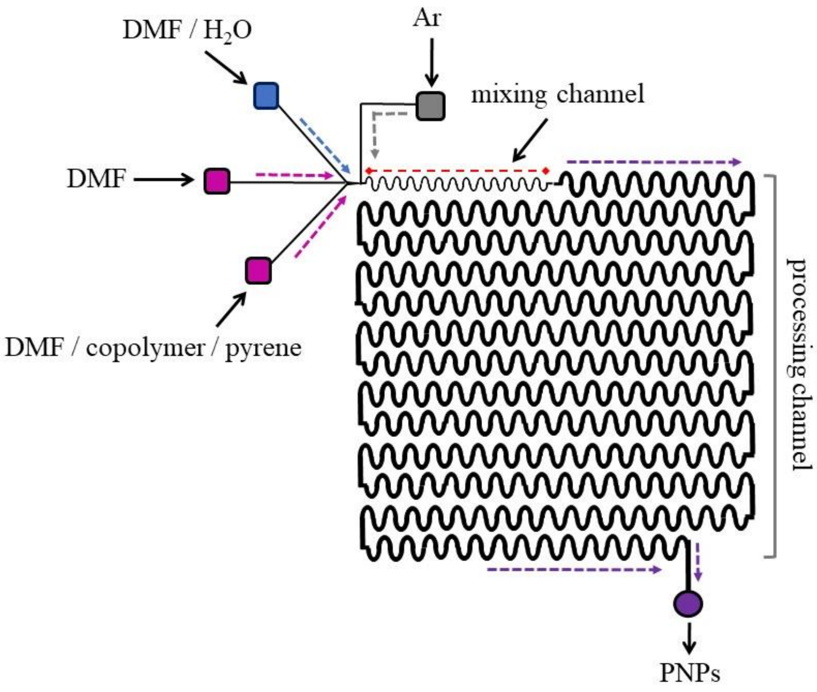

Figure 1-10. Schematic of the two-phase segmented flow microfluidic reactor showing inlet streams (solvent, water, solids) and outlet streams (PNPs) going through mixing and processing channels.

1.5. Characterization Techniques

1.5.1. Dynamic Light Scattering (DLS)

Dynamic light scattering, sometimes referred to as Photon Correlation Spectroscopy or Quasi-Elastic Light Scattering, is a technique used to characterize the hydrodynamic diameter of nanoparticles dispersed in solution.[58] DLS technique determines the size distribution profile of a nanoparticle dispersion in sub-micron ranges ($10^{-9} – 10^{-5}$ m).[58] The particle size measurement is achieved through understanding the Brownian motion of dispersed particle, which is related to the particle size.[59] Brownian motion is the random movement of particles due to bombardment with surrounding solvent molecules. As nanoparticles move randomly in the solution, the distance among them and the intensity of the scattered light will also change with time such that the big particles will move slowly whereas small particles move relatively faster. A system of nanoparticles in solution undergoing Brownian motion produces a speckle pattern where the position of each speckle is seen to be in constant motion, which is due to phase addition from the moving particles.[59] The speckle pattern constantly evolves to form new patterns and the rate of the intensity fluctuations determines particle speed and size, for example, smaller particles will give more rapid fluctuations than larger particles.[59] The changing intensity of scattered light is detected by an autocorrelator inside DLS instrument and it constructs the autocorrelation function G(τ) of the scattered light intensity.[59]

$$G_\tau = < I(t).I(t+\tau) >$$

The velocity of moving particles in Brownian motion is defined by using the translational diffusion coefficient (D_0) and the scattered light intensity is related to velocity of moving particles. The particle size measured through DLS is known as hydrodynamic diameter as it refers to the diameter of a sphere that has same diffusional coefficient as that of the nanoparticle. The hydrodynamic diameter for particles can be obtained from the autocorrelation function using various algorithms and there are two fundamentally different algorithms that are often used and reported: Cumulant Analysis and CONTIN analysis.[59] Cumulant Analysis uses a single exponential fitting for the correlation function to obtain the mean size (z-average diameter) and an estimate of the width of the distribution (polydispersity index), on the other hand, CONTIN analysis uses multiple exponential fits for the correlation function to obtain the distribution of particle sizes.[59]

The hydrodynamic radius (r_h) of nanoparticles is determined from the diffusion coefficient (D_0) from the scattered light intensity using the Stokes-Einstein equation and calculated as follows:

$$r_h = \frac{\kappa_B T}{6\pi\eta D_0}$$

In case of non-spherical particles, DLS measurements show the effect of shape/morphology of particle in a way that affects its diffusion coefficient.[59] For example, small changes in the length of a rod-shaped particle will directly impact the hydrodynamic size, whereas changes in the rod's diameter will hardly affect the diffusion speed and thus difficult to detect.[59]

1.5.2. X-Ray Diffraction

A particularly effective method to analyze semicrystalline polymers is by X-ray diffraction (XRD).[32] In a polymer sample, the crystallites regions will diffract X-ray beams from parallel planes for incident angles, θ, which are determined from the Bragg equation:

$$n\lambda = 2d \sin\theta$$

where n is an integer, λ is the wavelength of the incident beam and, d is the distance between parallel crystallite planes. When the incident beam interacts with crystallite regions within the polymer sample diffraction rings are produced.[32] These diffraction rings will be sharply defined for highly crystalline materials and become increasingly diffuse when the amorphous content is high.[32] Each semicrystalline polymer sample will have a characteristic diffraction pattern. To obtain an X-ray diffraction spectrum, a Fourier transform is applied to the X-ray diffraction pattern. An example of an XRD spectrum is presented in Figure 1-11. Weight percentage of polymer crystallinity can be calculated by accounting for the relative areas under crystallite peaks and amorphous halos. This procedure is described in detail in the experimental chapter section along with schematics and image of XRD instrument.

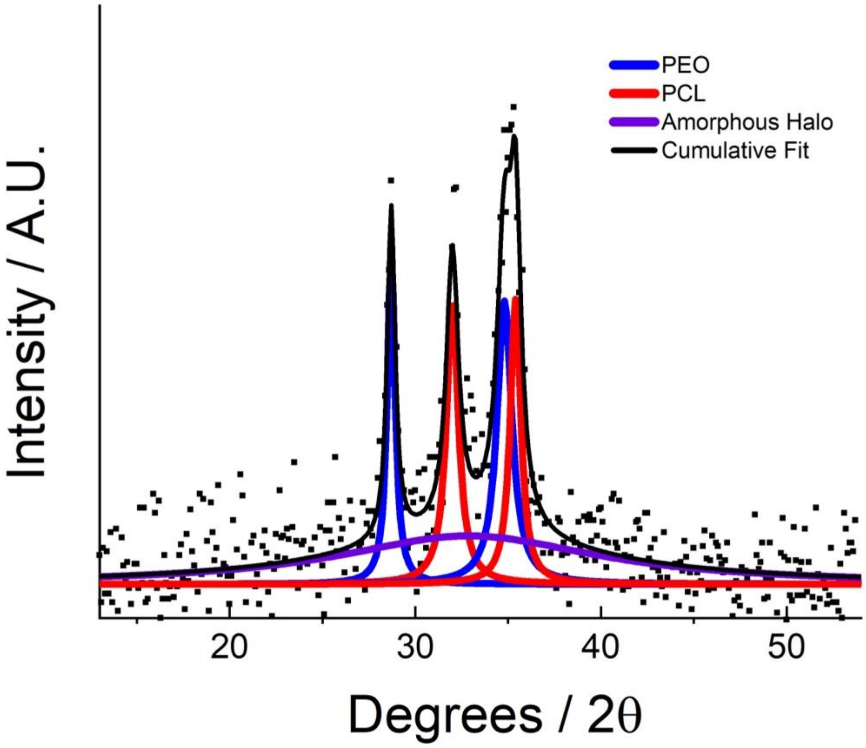

Figure 1-11. Representative x-ray diffraction profile of a PCL-*b*-PEO block copolymer nanoparticles, showing raw data and best fit function. The PNP sample was prepared using PCL_{2100}-*b*-PEO_{5000} at 200 μL min^{-1}, loading ratio (r = 0.1) and a water content of cwc + 5.0 wt%.

1.5.3. Transmission Electron Microscopy

For this thesis, PNP sizes and morphologies were routinely characterized using transmission electron microscopy (TEM). TEM is possible because of the work of de Broglie. We are able to use electrons for imaging of nanoparticles, due to the fact that an accelerated electron beam has an effective wavelength that is ~10^5 times shorter than visible light. Nanoparticle images are generated when an accelerated electron beam hits the specimen, scattering electrons at different angles.[32] Depending on the electron density of the specimen, the electrons from the electron beam can either be: 1. undeflected; 2. deflected from beam path without loss of energy (elastic scattering); or, 3. deflected from beam path with significant loss of energy (inelastic scattering).[32] The relative brightness of the image depends on the number of unscattered electrons that pass through the objective aperture. Furthermore, regions of the specimen composed of light atoms (carbon) will scatter relatively fewer electrons appearing bright; whereas, heavy atoms (iron) will scatter greater amounts of electrons, and appear dark.[32]

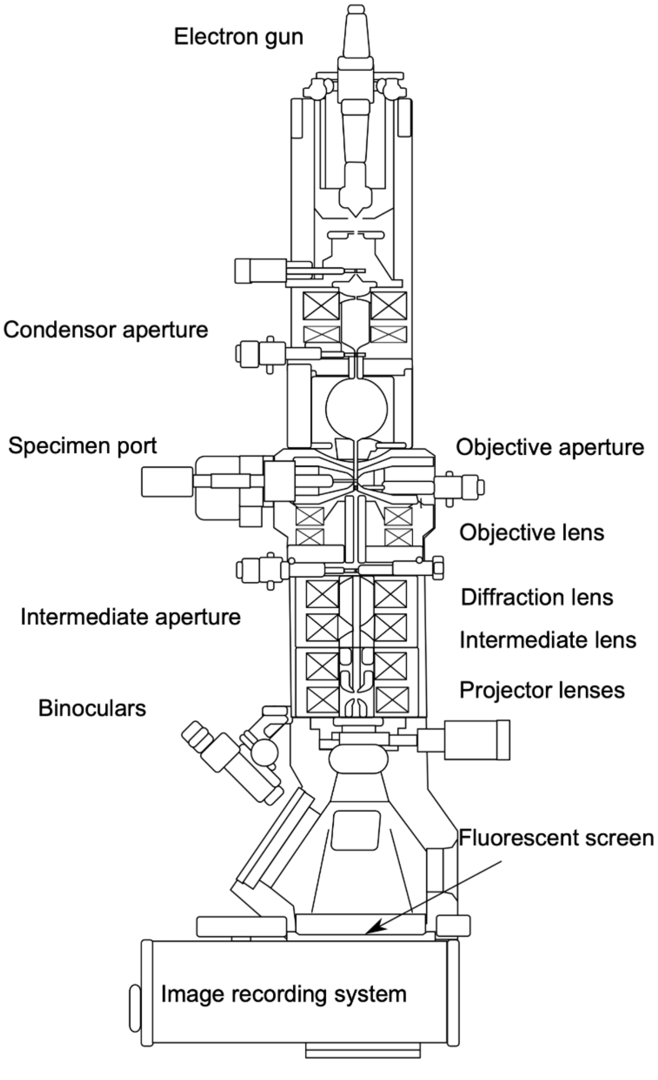

Figure 1-12. Schematics of a Transmission Electron Microscope. [60]

Our group regularly use uranyl acetate to negatively stain the TEM images, providing better contrast for the PCL-*b*-PEO PNPs, since the PNPs used in this thesis are composed mostly of carbon atoms, they do not provide enough contrast to allow for effective imaging. Uranyl acetate selectively binds to the PEO block of our PNPs, providing negative contrast by deflecting greater amounts of electrons than the PCL core.[32] Due to this negative staining, our TEM images appear dark, with light regions representing the PCL cores of the PNPs.

1.6. Outline of Thesis

This thesis focuses on the preparation of Py-PNPs using microfluidics under the action of a combination of chemical and processing variables to further understand the changes in internal structure of PNPs by the preparation conditions. This is achieved by applying characterization techniques that characterize multiscale structural features of Py-PNPs and using fluorescence to probe the internal structure and microenvironment changes in the PNP core. The remaining chapters consists of a description of experiments chapter, a results and discussion chapter, and a conclusion and future directions chapter. Specific contents of each chapter are summarized as follows:

Chapter 2 provides information to the methodology and characterization techniques used in all the experiments performed in the thesis. This chapter contains detailed information on the experimental methods and characterization setup such as critical water content determination, step-by-step approach to microfluidic reactor fabrication, achieving microfluidic flow control and detailed description of microfluidic preparation of Py-PNPs. In later part, this chapter delves into spectroscopic method details for steady-state fluorescence, x-ray diffraction, dynamic light scattering, etc. Lastly, we describe the statistical analysis used to compare any two experiment derived data points or sets.

Chapter 3 reports the results for on-chip loading of the fluorescent probe pyrene (Py) into PCL-b-PEO polymer nanoparticles (Py-PNPs) under different chemical and flow conditions within a two-phase segmented microfluidic reactor. In this chapter we study the influence of four different experimental variables for Py-PNP preparation on both the physicochemical properties and fluorescence properties of Py-PNPs. Specifically, we investigated the effects of PCL block length, initial Py:copolymer loading ratio, r_{Py}, on-chip water content, and microfluidic flow rate, Q on the structural properties of PNPs and Py fluorescence intensity ratios. These gave an insight on the changing microenvironment of Py-PNPs influenced by each chemical and processing variable. In later part of this chapter, we combine the different datasets from the four different preparation conditions to establish general relationships between physicochemical properties of Py-PNPs, including mean effective hydrodynamic diameters and drug loading of the PCL core with the Py fluorescence ratios. This yields a general understanding of the impact of physicochemical properties on the internal structure and core microenvironment of Py-PNPs.

Chapter 4 contains main findings and conclusions from this thesis work and suggests some directions for future work.

1.7. References

(1) Hickey, J. W.; Santos, J. L.; Williford, J.-M.; Mao, H.-Q. Control of Polymeric Nanoparticle Size to Improve Therapeutic Delivery. *J Control Release* **2015**, *219*, 536–547.

(2) Nicolas, J.; Mura, S.; Brambilla, D.; Mackiewicz, N.; Couvreur, P. Design, Functionalization Strategies and Biomedical Applications of Targeted Biodegradable/Biocompatible Polymer-Based Nanocarriers for Drug Delivery. *Chem Soc Rev* **2013**, *42* (3), 1147–1235.

(3) Eetezadi, S.; Ekdawi, S. N.; Allen, C. The Challenges Facing Block Copolymer Micelles for Cancer Therapy: In Vivo Barriers and Clinical Translation. *Adv Drug Deliv Rev* **2015**, *91*, 7–22.

(4) Ahmed, F.; Pakunlu, R. I.; Brannan, A.; Bates, F.; Minko, T.; Discher, D. E. Biodegradable Polymersomes Loaded with Both Paclitaxel and Doxorubicin Permeate and Shrink Tumors, Inducing Apoptosis in Proportion to Accumulated Drug. *J Control Release* **2006**, *116* (2), 150–158.

(5) Elsabahy, M.; Wooley, K. L. Design of Polymeric Nanoparticles for Biomedical Delivery Applications. *Chem. Soc. Rev.* **2012**, *41* (7), 2545–2561.

(6) Zhang, Y.; Chan, H. F.; Leong, K. W. Advanced Materials and Processing for Drug Delivery: The Past and the Future. *Adv Drug Deliv Rev* **2013**, *65* (1), 104–120.

(7) Knop, K.; Hoogenboom, R.; Fischer, D.; Schubert, U. S. Poly(Ethylene Glycol) in Drug Delivery: Pros and Cons as Well as Potential Alternatives. *Angew Chem Int Ed Engl* **2010**, *49* (36), 6288–6308.

(8) Tan, J. S.; Butterfield, D. E.; Voycheck, C. L.; Caldwell, K. D.; Li, J. T. Surface Modification of Nanoparticles by PEO/PPO Block Copolymers to Minimize Interactions with Blood Components and Prolong Blood Circulation in Rats. *Biomaterials* **1993**, *14* (11), 823–833.

(9) Allen, C.; Yu, Y.; Maysinger, D.; Eisenberg, A. Polycaprolactone-b-Poly(Ethylene Oxide) Block Copolymer Micelles as a Novel Drug Delivery Vehicle for Neurotrophic Agents FK506 and L-685,818. *Bioconjugate Chem.* **1998**, *9* (5), 564–572.

(10) Lavasanifar, A.; Samuel, J.; Kwon, G. S. Poly(Ethylene Oxide)-Block-Poly(L-Amino Acid) Micelles for Drug Delivery. *Adv Drug Deliv Rev* **2002**, *54* (2), 169–190.

(11) Khan, I. U.; Serra, C. A.; Anton, N.; Vandamme, T. Microfluidics: A Focus on Improved Cancer Targeted Drug Delivery Systems. *J Control Release* **2013**, *172* (3), 1065–1074.

(12) Sun, T.; Zhang, Y. S.; Pang, B.; Hyun, D. C.; Yang, M.; Xia, Y. Engineered Nanoparticles for Drug Delivery in Cancer Therapy. *Angew Chem Int Ed Engl* **2014**, *53* (46), 12320–12364.

(13) Björnmalm, M.; Thurecht, K. J.; Michael, M.; Scott, A. M.; Caruso, F. Bridging Bio–Nano Science and Cancer Nanomedicine. *ACS Nano* **2017**, *11* (10), 9594–9613.

(14) Tyrrell, Z. L.; Shen, Y.; Radosz, M. Fabrication of Micellar Nanoparticles for Drug Delivery through the Self-Assembly of Block Copolymers. *Progress in Polymer Science* **2010**, *35* (9), 1128–1143.

(15) Letchford, K.; Burt, H. A Review of the Formation and Classification of Amphiphilic Block Copolymer Nanoparticulate Structures: Micelles, Nanospheres, Nanocapsules and Polymersomes. *Eur J Pharm Biopharm* **2007**, *65* (3), 259–269.

(16) Bains, A.; Cao, Y.; Moffitt, M. G. Multiscale Control of Hierarchical Structure in Crystalline Block Copolymer Nanoparticles Using Microfluidics. *Macromolecular Rapid Communications* **2015**, *36* (22), 2000–2005.

(17) Wang, C.-W.; Oskooei, A.; Sinton, D.; Moffitt, M. G. Controlled Self-Assembly of Quantum Dot−Block Copolymer Colloids in Multiphase Microfluidic Reactors. *Langmuir* **2010**, *26* (2), 716–723.

(18) Wang, C.-W.; Sinton, D.; Moffitt, M. G. Flow-Directed Block Copolymer Micelle Morphologies via Microfluidic Self-Assembly. *J. Am. Chem. Soc.* **2011**, *133* (46), 18853–18864.

(19) Wang, C.-W.; Sinton, D.; Moffitt, M. G. Morphological Control via Chemical and Shear Forces in Block Copolymer Self-Assembly in the Lab-on-Chip. *ACS Nano* **2013**, *7* (2), 1424–1436.

(20) Bains, A.; Cao, Y.; Kly, S.; Wulff, J. E.; Moffitt, M. G. Controlling Structure and Function of Polymeric Drug Delivery Nanoparticles Using Microfluidics. *Mol. Pharmaceutics* **2017**, *14* (8), 2595–2606.

(21) Xu, Z.; Lu, C.; Riordon, J.; Sinton, D.; Moffitt, M. G. Microfluidic Manufacturing of Polymeric Nanoparticles: Comparing Flow Control of Multiscale Structure in Single-Phase Staggered Herringbone and Two-Phase Reactors. *Langmuir* **2016**, *32* (48), 12781–12789.

(22) Zhao, C. L.; Winnik, M. A.; Riess, G.; Croucher, M. D. Fluorescence Probe Techniques Used to Study Micelle Formation in Water-Soluble Block Copolymers. *Langmuir* **1990**, *6* (2), 514–516.

(23) M. Taylor, J.; Scale, K.; Arrowsmith, S.; Sharp, A.; Flynn, S.; Rannard, S.; O. McDonald, T. Using Pyrene to Probe the Effects of Poloxamer Stabilisers on Internal Lipid Microenvironments in Solid Lipid Nanoparticles. *Nanoscale Advances* **2020**, *2* (12), 5572–5577.

(24) Kumar, V.; Adamson, D. H.; Prud'homme, R. K. Fluorescent Polymeric Nanoparticles: Aggregation and Phase Behavior of Pyrene and Amphotericin B Molecules in Nanoparticle Cores. *Small* **2010**, *6* (24), 2907–2914.

(25) Wu, T.; Oake, J.; Liu, Z.; Bohne, C.; Branda, N. R. Probing the Microenvironments in a Polymer-Wrapped Core–Shell Nanoassembly Using Pyrene Chromophores. *ACS Omega* **2018**, *3* (7), 7673–7680.

(26) Cai, S.; Vijayan, K.; Cheng, D.; Lima, E. M.; Discher, D. E. Micelles of Different Morphologies—Advantages of Worm-like Filomicelles of PEO-PCL in Paclitaxel Delivery. *Pharm Res* **2007**, *24* (11), 2099–2109.

(27) Geng, Y.; Dalhaimer, P.; Cai, S.; Tsai, R.; Tewari, M.; Minko, T.; Discher, D. E. Shape Effects of Filaments versus Spherical Particles in Flow and Drug Delivery. *Nat Nanotechnol* **2007**, *2* (4), 249–255.

(28) Glover, A. L.; Bennett, J. B.; Pritchett, J. S.; Nikles, S. M.; Nikles, D. E.; Nikles, J. A.; Brazel, C. S. Magnetic Heating of Iron Oxide Nanoparticles and Magnetic Micelles for Cancer Therapy. *IEEE Trans Magn* **2013**, *49* (1), 231–235.

(29) Williams, D. E.; Dolgopolova, E. A.; Pellechia, P. J.; Palukoshka, A.; Wilson, T. J.; Tan, R.; Maier, J. M.; Greytak, A. B.; Smith, M. D.; Krause, J. A.; Shustova, N. B. Mimic of the Green Fluorescent Protein β-Barrel: Photophysics and Dynamics of Confined Chromophores Defined by a Rigid Porous Scaffold. *J. Am. Chem. Soc.* **2015**, *137* (6), 2223–2226.

(30) Abraham, S.; Weiss, R. G. Photochemical and Photophysical Studies of and in Bulk Polymers. In *Supramolecular Photochemistry*; John Wiley & Sons, Ltd, 2011; pp 443–516.

(31) Bains, A.; Wulff, J. E.; Moffitt, M. G. Microfluidic Synthesis of Dye-Loaded Polycaprolactone-Block-Poly(Ethylene Oxide) Nanoparticles: Insights into Flow-Directed Loading and in Vitro Release for Drug Delivery. *Journal of Colloid and Interface Science* **2016**, *475*, 136–148.

(32) Cowie, J. M. G.; Arrighi, V. *Polymers: Chemistry and Physics of Modern Materials, Third Edition*, 3rd ed.; CRC Press: Boca Raton, 2007.

(33) Hamley, I. W. *The Physics of Block Copolymers*; Oxford University Press: Oxford, New York, 1999.

(34) Alexandridis, P.; Alan Hatton, T. Poly(Ethylene Oxide)-*b*-poly(Propylene Oxide)-*b*-poly(Ethylene Oxide) Block Copolymer Surfactants in Aqueous Solutions and at

Interfaces: Thermodynamics, Structure, Dynamics, and Modeling. *Colloids and Surfaces A: Physicochemical and Engineering Aspects* **1995**, *96* (1), 1–46.

(35) Halperin, A. Polymeric Micelles: A Star Model. *Macromolecules* **1987**, *20* (11), 2943–2946.

(36) Introduction to Polymer Science. In *Introduction to Physical Polymer Science*; John Wiley & Sons, Ltd, 2005; pp 1–28.

(37) Mai, Y.; Eisenberg, A. Self-Assembly of Block Copolymers. *Chem. Soc. Rev.* **2012**, *41* (18), 5969–5985.

(38) Peter Atkins; Julio de Paula; James Keeler, Atkins' Physical Chemistry 11 edition, *Oxford University Press*.

(39) The Crystalline State. In *Introduction to Physical Polymer Science*; John Wiley & Sons, Ltd, 2005; pp 239–323.

(40) Hu, W.; Zha, L. Thermodynamics and Kinetics of Polymer Crystallization. In *Polymer Morphology*; John Wiley & Sons, Ltd, 2016; pp 242–258.

(41) The Amorphous State. In *Introduction to Physical Polymer Science*; John Wiley & Sons, Ltd, 2005; pp 197–238.

(42) Shalu; Singh, R. K. Chapter 16 - Effect of Ionic Liquids on the Crystallization Kinetics of Various Polymers and Polymer Electrolytes. In *Crystallization in Multiphase Polymer Systems*; Thomas, S., Arif P., M., Gowd, E. B., Kalarikkal, N., Eds.; Elsevier, 2018; pp 509–533.

(43) *Principles of Fluorescence Spectroscopy*; Lakowicz, J. R., Ed.; Springer US: Boston, MA, 2006.

(44) Murov, S. L.; Carmichael, I.; Hug, G. L. *Handbook of Photochemistry, Second Edition*; CRC Press, 1993.

(45) Kalyanasundaram, K.; Thomas, J. K. Environmental effects on Vibronic Band Intensities in Pyrene Monomer Fluorescence and their application in studies of Micellar Systems, *Journal of the American Chemical Society*, **1977**, *99(7)*, 2039-2043.

(46) Pensack, R. D.; Ashmore, R. J.; Paoletta, A. L.; Scholes, G. D. The Nature of Excimer Formation in Crystalline Pyrene Nanoparticles. *J. Phys. Chem. C* **2018**, *122* (36), 21004–21017.

(47) Kwon, G. S.; Naito, M.; Kataoka, K.; Yokoyama, M.; Sakurai, Y.; Okano, T. Block Copolymer Micelles as Vehicles for Hydrophobic Drugs. *Colloids and Surfaces B: Biointerfaces* **1994**, *2* (4), 429–434.

(48) Zhao, J.; Allen, C.; Eisenberg, A. Partitioning of Pyrene between "Crew Cut" Block Copolymer Micelles and H2O/DMF Solvent Mixtures. *Macromolecules* **1997**, *30* (23), 7143–7150.

(49) Kobayashi, N.; Saito, R.; Hino, H.; Hino, Y.; Ueno, A.; Osa, T. Fluorescence and Induced Circular Dichroism Studies on Host–Guest Complexation between γ-Cyclodextrin and Pyrene. *J. Chem. Soc., Perkin Trans. 2* **1983**, No. 7, 1031–1035.

(50) Dong, D. C.; Winnik, M. A. The Py Scale of Solvent Polarities. *Can. J. Chem.* **1984**, *62* (11), 2560–2565.

(51) Glushko, V.; Thaler, M. S. R.; Karp, C. D. Pyrene Fluorescence Fine Structure as a Polarity Probe of Hydrophobic Regions: Behavior in Model Solvents. *Archives of Biochemistry and Biophysics* **1981**, *210* (1), 33–42.

(52) Stevens, B.; Hutton, E. Radiative Life-Time of the Pyrene Dimer and the Possible Role of Excited Dimers in Energy Transfer Processes. *Nature* **1960**, *186* (4730), 1045–1046.

(53) Birks, J. B.; Christophorou, L. G. Excimer Formation in Polycyclic Hydrocarbons and Their Derivatives. *Nature* **1963**, *197* (4872), 1064–1065.

(54) Song, H.; Tice, J. D.; Ismagilov, R. F. A Microfluidic System for Controlling Reaction Networks in Time. *Angewandte Chemie International Edition* **2003**, *42* (7), 768–772.

(55) Stone, H. A.; Stroock, A. D.; Ajdari, A. Engineering Flows in Small Devices: Microfluidics Toward a Lab-on-a-Chip. *Annual Review of Fluid Mechanics* **2004**, *36* (1), 381–411.

(56) Squires, T. M.; Quake, S. R. Microfluidics: Fluid Physics at the Nanoliter Scale. *Rev. Mod. Phys.* **2005**, *77* (3), 977–1026. https://doi.org/10.1103/RevModPhys.77.977.

(57) Teh, S.-Y.; Lin, R.; Hung, L.-H.; Lee, A. P. Droplet Microfluidics. *Lab Chip* **2008**, *8* (2), 198–220.

(58) Light Scattering. In *Particle Characterization: Light Scattering Methods*; Xu, R., Scarlett, B., Eds.; Particle Technology Series; Springer Netherlands: Dordrecht, 2002; pp 56–110.

(59) Pecora, R. *Dynamic Light Scattering: Applications of Photon Correlation Spectroscopy*; Springer Science & Business Media, **2013**.

(60) Transmission Electron Microscopy. *Wikipedia*; **2023**, date accessed: 25 April 2023.

Chapter 2 Description of Experiments

2.1. Materials

The block copolymers used in this study were obtained from Advanced Polymer Materials comprising of poly(caprolactone)-*b*-poly(ethylene glycol) (PCL-*b*-PEG). Three different compositions of copolymers were used, varying in the number-average molecular weights (M_n) of the PCL blocks. For the three copolymers, the lengths of the PCL blocks were M_n = 2100 g mol^{-1}, 5000 g mol^{-1} and 12000 g mol^{-1}, respectively, while the length of the PEG block was fixed at M_n = 5000 g mol^{-1}. The dispersity of the three block copolymers were *Đ* = 1.08, 1.13 and 1.20, respectively, for PCL(2100)-*b*-PEG(5000), PCL(6000)-*b*-PEG(5000) and PCL(12000)-b-PEG(5000), where numbers in brackets indicate M_n of the respective blocks. Within the thesis, the three different block copolymers will be referred to according to their PCL block lengths, using the names PCL2.1k, PCL6k and PCL12k, respectively. Pyrene was purchased from Sigma Aldrich (>99.0%), *N*,*N*-dimethylformamide (DMF, >99.9%) and acetonitrile (HPLC grade) were purchased from Fisher Scientific and used without further purification. Pyrene purchased from Sigma Aldrich was >99% pure (fluorescent grade); the purity of pyrene was checked experimentally before it was used, as described in a later section.

2.2. Critical Water Content (cwc) Determination

The cwc is the minimum water content that is required for block copolymer self-assembly into micellar aggregates in a given solvent and at a given copolymer concentration. Static light scattering (SLS) measurements were carried out to determine the cwc of 0.33 wt % copolymer in DMF solution, which was the initial condition for all self-assembly experiments in this study. SLS experiments were performed on a Brookhaven Instruments photo-correlation spectrometer equipped with a BI-200SM goniometer, a BI-

9000AT digital autocorrelator, and a BI-Mini-L30 30 mW red (636 nm) compact diode laser, at a scattering angle of 90° and a temperature of 23.0 ± 0.1 °C (Figure 2-1).

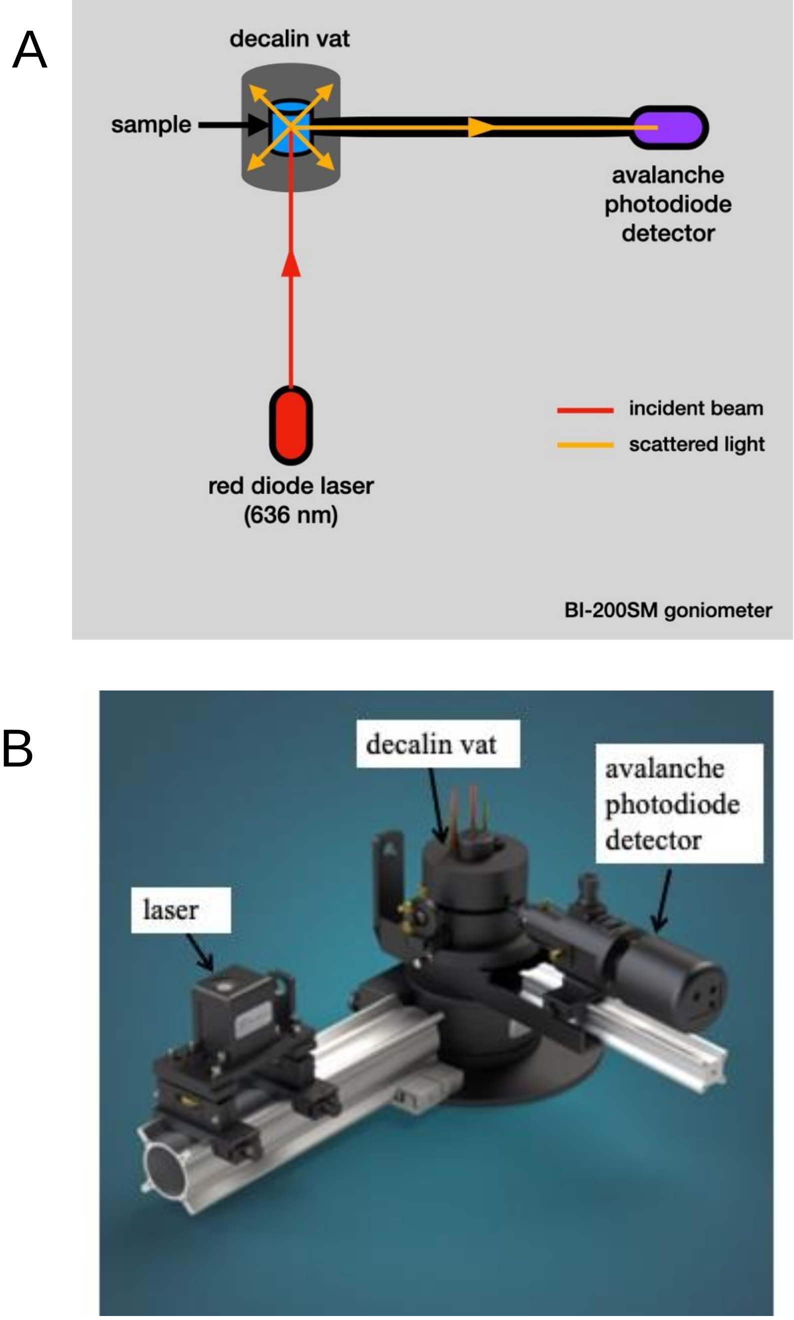

Figure 2-1. (a) Schematic of static light scattering instrument (b) Actual image (source: brookshaveninstrument.com) of static light scattering instrument equipped with BI-200SM goniometer system having red diode laser (636 nm) and avalanche photodiode (APD) detector (set at 90 degrees to laser beam).

For each cwc determination, 1.0 wt % copolymer stock solution in DMF was prepared and stirred overnight. This solution was filtered through 2 × 0.45 μm nominal pore size Teflon syringe filters (VWR) into pre-cleaned scintillation vials, and then was diluted to a final concentration of 0.33 wt % by gravimetric addition of DMF. To the resulting ~5 g of solution, deionized water was added in successive 0.03−0.06 g quantities using a microsyringe equipped with 2 × 0.20 μm nominal pore size nylon syringe filters (National Scientific). After each addition of water, the sample was allowed to equilibrate for 15 min before the scattered light intensity was measured. The resulting scattered light intensity was plotted vs. water concentration. Then the cwc value was determined from the intercept of linear fits to the baseline and the sharply increasing intensity region. Representative titration plots and cwc determination for each copolymer are shown in Figure 2-2.

Determinations of cwc were carried out in triplicate from the same stock solution and the mean value and standard error of the three measurements were used to calculate the reported cwc and experimental error. The cwc values for the three different block copolymers under the stated conditions used in this study were as follows: 12.7 ± 0.5 wt % for PCL2.1k, 6.3 ± 0.2 wt % for PCL6k, and 5.7 ± 0.3 wt % for PCL12k.

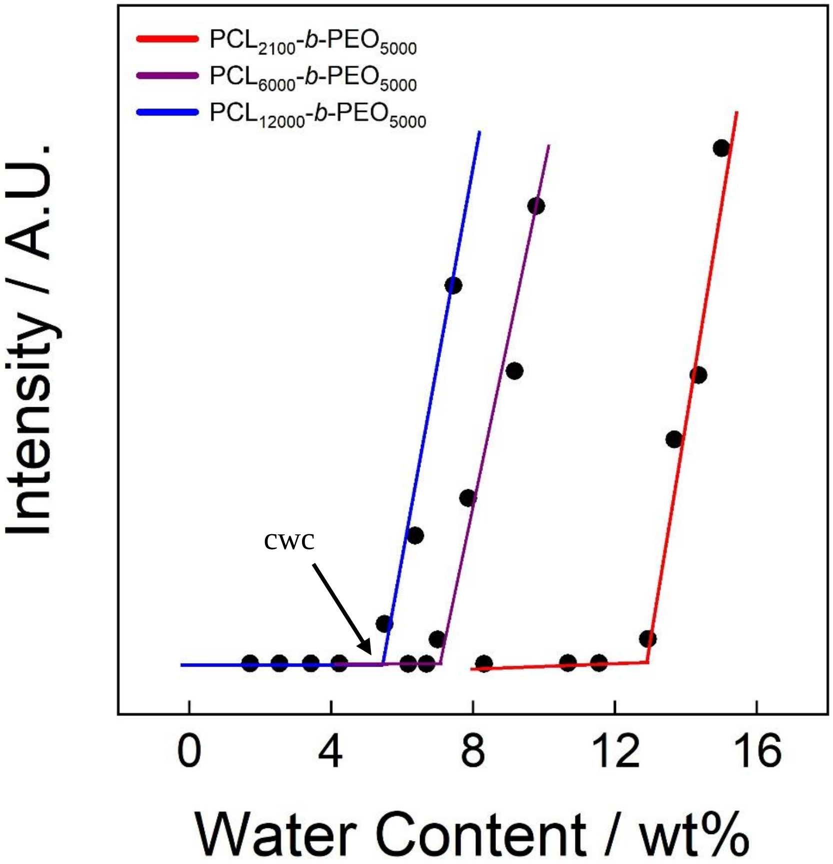

Figure 2-2. Determination of critical water content (cwc) for 0.33 wt% PCL-*b*-PEO copolymers in DMF solvent using static light scattering method on goniometer BIC-200SM instrument for three different PCL block lengths.

2.3. Microfluidic Reactor Fabrication

Negative masters were fabricated on silicon wafers (Silicon Materials) using the negative photoresist SU-8 100 (Kayaku). The whole process is outlined in the Figure 2-3. A 150 µm thick SU-8 film was spin-coated at 2000 rpm onto the silicon wafer and heated at 65 °C for 12 min and then at 95 °C for 50 min. After the wafer was cooled, a photomask (Figure 2-3) was placed directly above, and the wafer was exposed to UV light for 100 s. Then, the UV-treated film was heated at 65 °C for 1 min and then 95 °C for 20 min. Finally, the silicon wafer was submerged in SU-8 developer (Kayaku) and rinsed with isopropanol until all unexposed photoresist was removed.

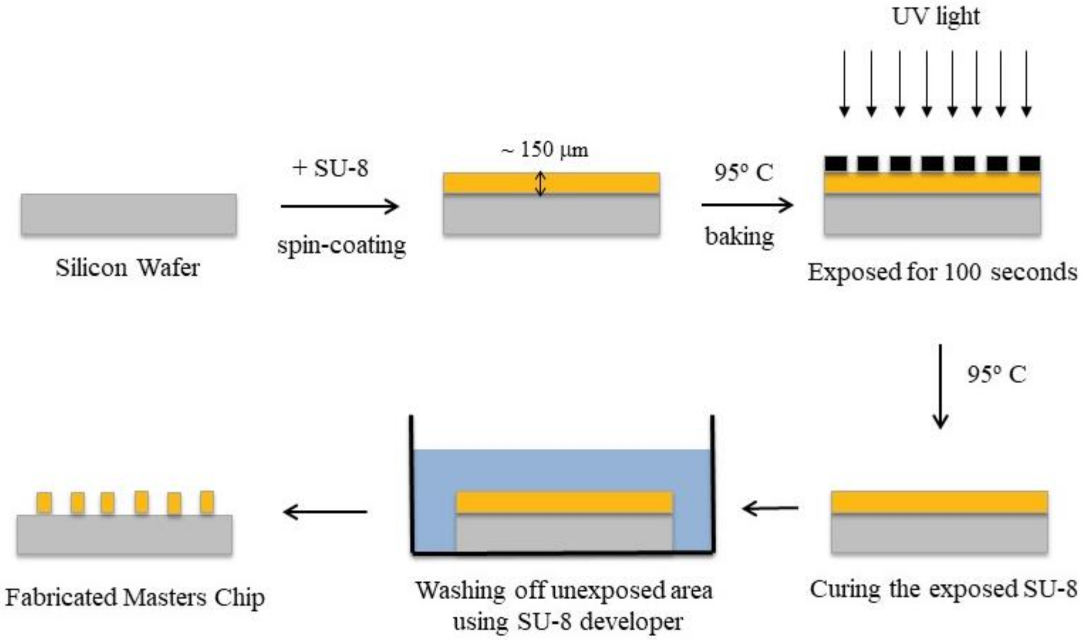

Figure 2-3. Outline of the Silicon Masters Chip fabrication process using SU-8 polymer as a negative photoresist and ultraviolet light.

Microfluidic chips were fabricated from poly-(dimethylsiloxane) (PDMS) using a SYLGARD 184 silicon elastomer kit (Dow Corning). For fabrication of all PDMS chips, the elastomer and curing agent were mixed at a 7:1 ratio and degassed under vacuum. The resulting mixture was poured over a clean negative master chip in a Petri dish and further degassed until all remaining air bubbles were removed. The PDMS was heated at 85 °C until cured (~20 min) and then peeled from the negative master; holes were punched through the reservoirs of the resulting PDMS chip to allow for the insertion of tubing. A thin PDMS film (substrate layer) was also made on a glass slide by spin-coating a 20:1 elastomer/ curing agent mixture followed by curing. The substrate layer was then permanently bonded to the base of the microfluidic reactor (channel layer) after both components were exposed to oxygen plasma for 90 s. The resulting reactor has a set channel depth of 150 μm and consists of a sinusoidal mixing channel 100 μm wide and a sinusoidal processing channel 200 μm wide as showing Figure 2-4, identical to the reactor described in previous publications from our group. [1-6]

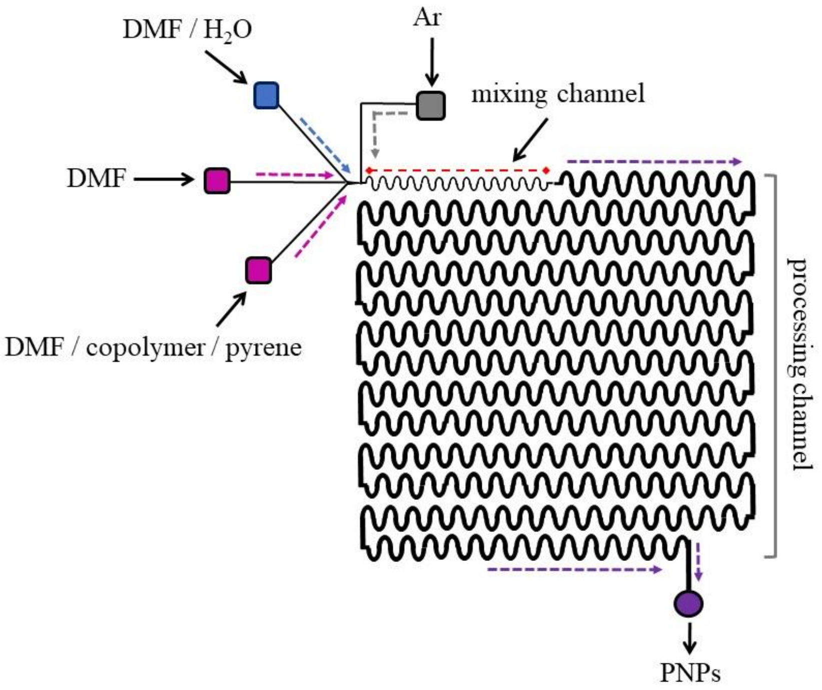

Figure 2-4. Schematic of the two-phase segmented flow microfluidic reactor showing inlet streams (solvent, water, solids) and outlet streams (PNPs) going through mixing and processing channels.

2.4. Flow Delivery and Control

Pressure-driven flow of liquids to the reactor inlet was provided using 1 mL gastight syringes (Hamilton, Reno, NV) mounted on syringe pumps (Harvard Apparatus, Holliston, MA). The microfluidic chip was connected to the liquid syringes via 1/16th-inch (OD) Teflon tubing (Scientific Products and Equipment, ON). Argon (Ar) gas flow was introduced to the chip via an Argon gas tank regulator and a downstream regulator (Johnston Controls) for fine adjustments. The chip was connected to the downstream regulator through a 1/16 i.n. (OD)/100 μm (ID) Teflon tube (Upchurch Scientific, Oak Harbor, WA). The microfluidic chip setup as shown in Figure 2-5.

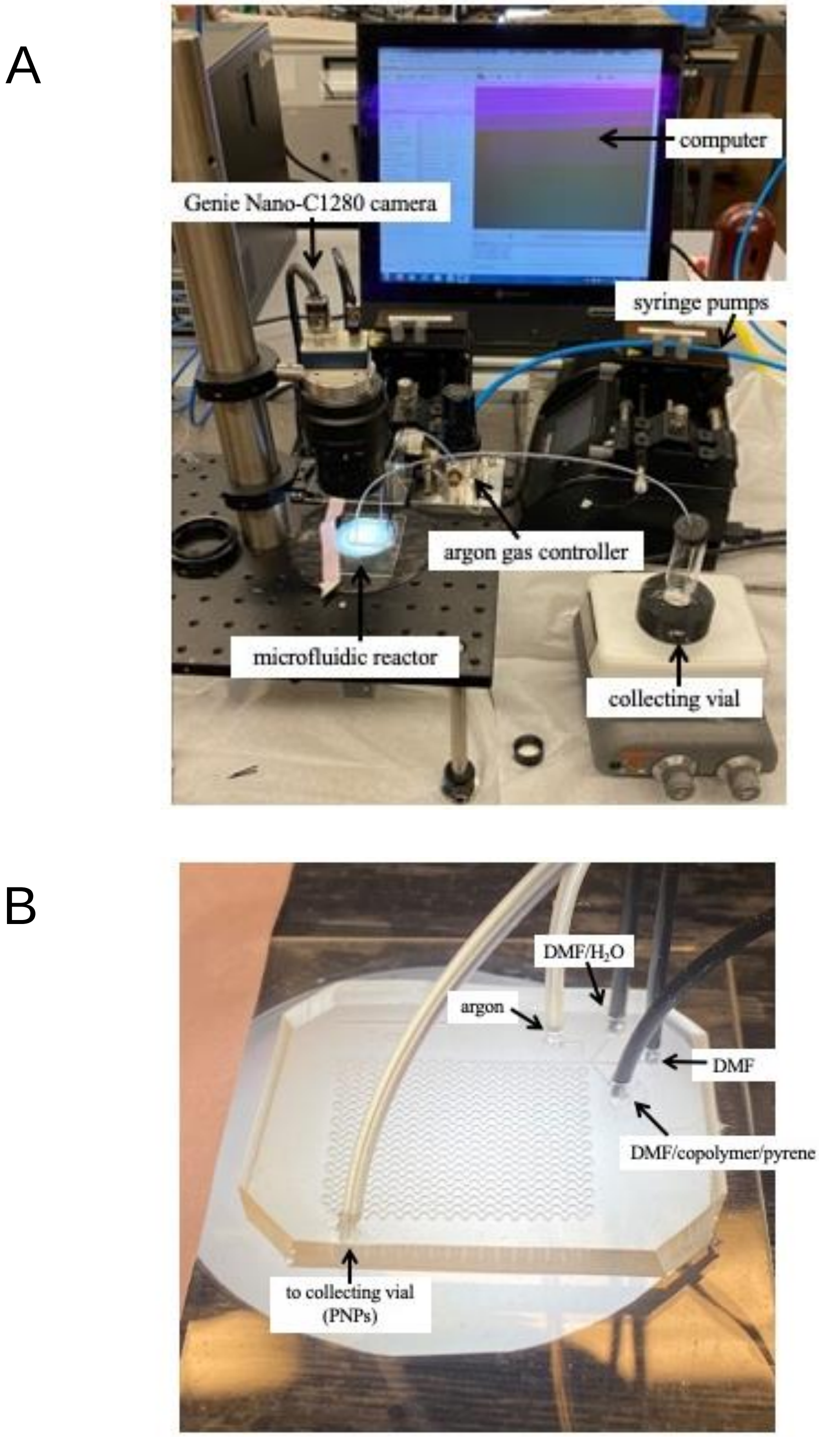

Figure 2-5. (a) An image showing the setup of microfluidic reactor that is used to prepare PNPs (b) close-up view of a two-phase segmented flow microfluidic reactor.

The liquid flow rate (Q_{liq}) was programmed via the syringe pumps, and the gas flow rate (Q_{gas}) was fine-tuned via the downstream pressure regulator in order to set the nominal total flow rates (Q) of 50, 100, 200, and 400 μL min^{-1} described in the main text. Images of the microchannels were captured using a Genie Nano-C1280 camera (1stVision) equipped with an On-Semi Python1300 sensor and a C-Mount Manual Iris Varifocal lens (1/1.8″, 4–13 mm, f/1.5) (Tamron) as displayed in Figure 2-5.

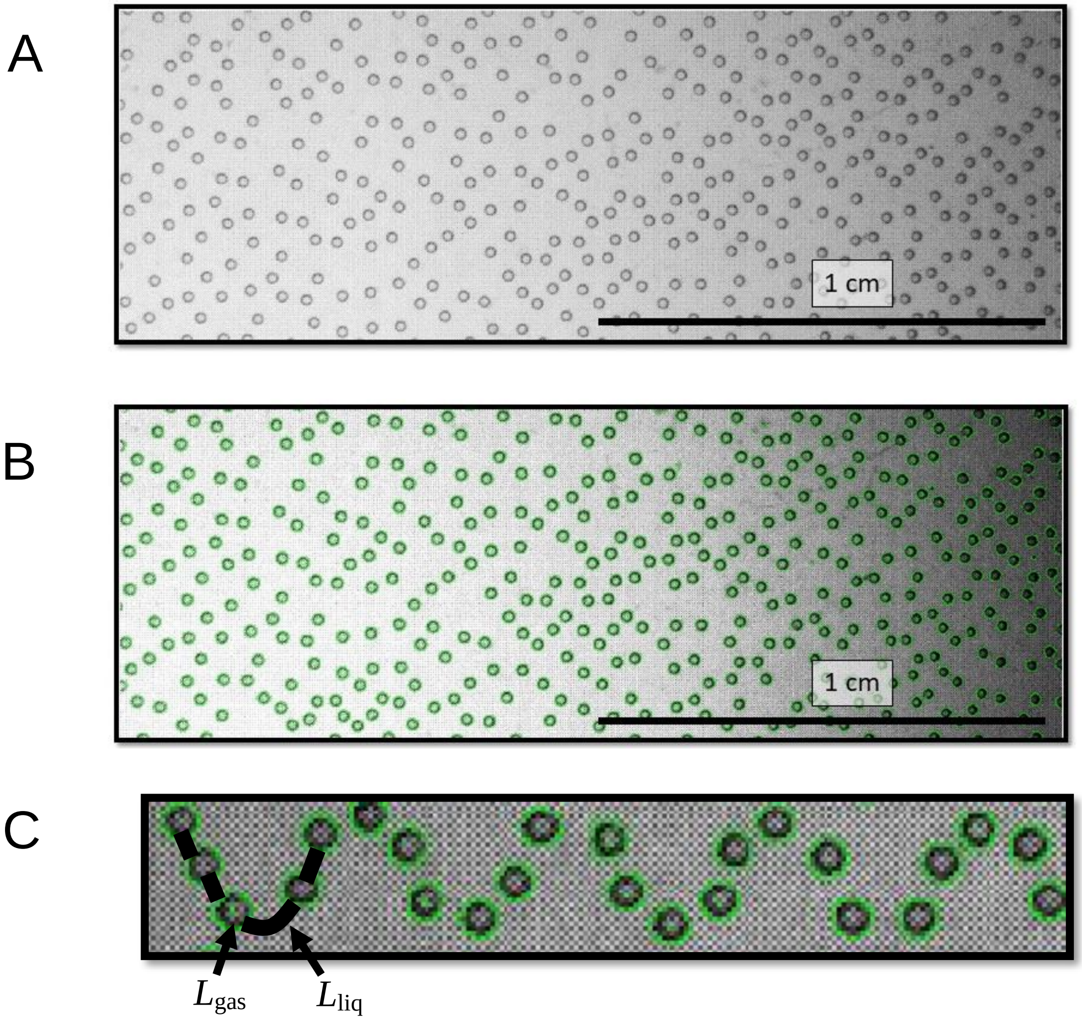

Figure 2-6. (a) Microscopic image snapshot of a microfluidic sample preparation on the two-phase microfluidic reactor captured using a Genie Nano-C1280 camera; the bubbles displayed consists of argon gas (b) MATLAB Flow Rate analysis software detecting argon gas bubbles (fluorescent green) from a microscopic image (c) displaying L_{gas} is the length of bubble (fluorescent green) and L_{liq} is the length of the liquid plug. A portion of the channel path (which is not visible due to lack of contrast) is traced in solid black for clarity.

Due to the compressible nature of the gas and the high gas/liquid interfacial tension, discrepancies arise between the nominal (programmed) and actual values of Q_{gas}, Q_{gas}/Q_{liq}, and the total flow rate (Q_{total}). Therefore, actual values of Q_{gas}, Q_{gas}/Q_{liq}, and $Q_{total} = Q_{gas} + Q_{liq}$ for each microfluidic experiment were calculated from the frequency of bubble formation and the average volume of gas bubbles, determined from image analysis of the mean lengths of liquid and gas plugs, L_{liq} and L_{gas}, respectively, under a given set of flow conditions (Figure 2-6).

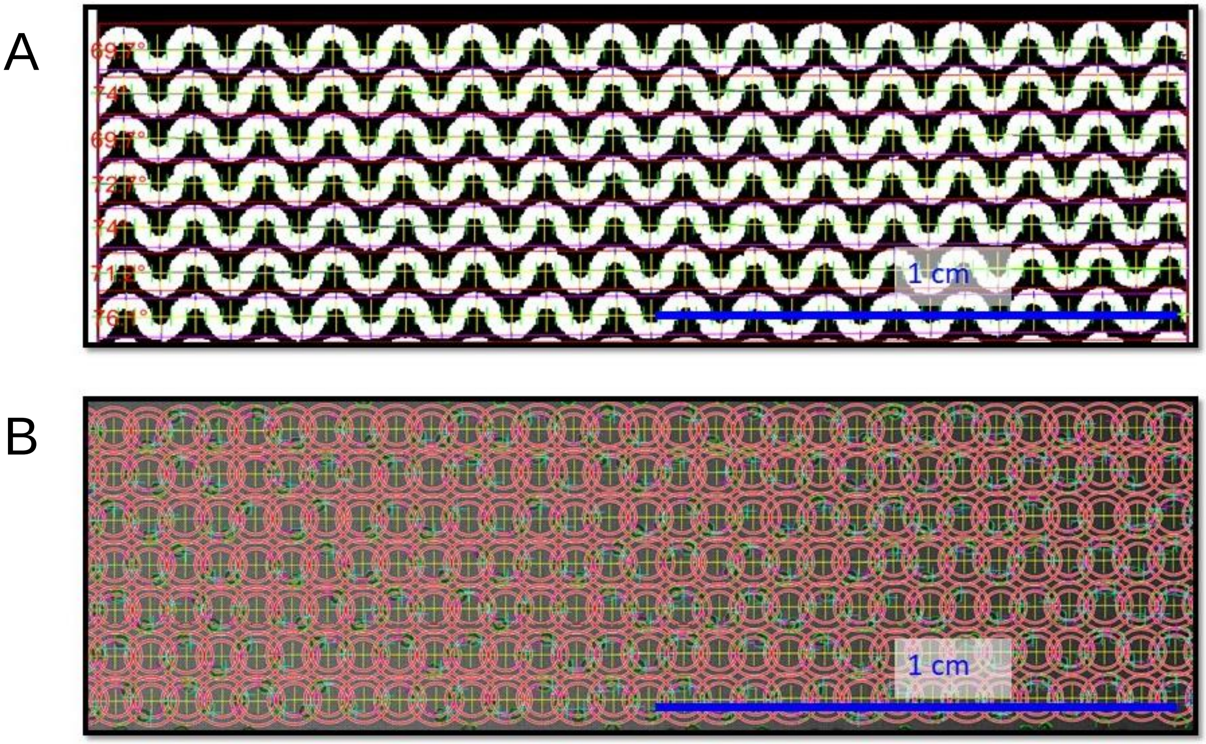

Figure 2-7. MATLAB Flow Rate analysis software (a) detecting microfluidic channels on a microfluidic reactor from an image; purple lines indicate boundaries between two channels (b) performing a combined detection of bubbles and channels to determine the L_{gas}/ L_{liq}.

The visualization and actual flow rate calculations were done using a modified version of MATLAB software originally developed by Eugenia Kumacheva's lab at the

University of Toronto and generously shared with our lab as shown in Figure 2-7.[7] For all experiments, $Q_{gas}/Q_{liq} \sim 1$; actual Q_{total} values are within 10 % of nominal Q values. The Q values were determined for each Py-PNP sample prepared in this thesis and shown in Table 2-1, 2-2, 2-3 and 2-4.

Table 2-1. Actual gas and liquid flow rates for various preparations of Py-PNPs; for all preparations described in this table, Q = 200 μL min^{-1}, r = 0.1 and water content = cwc + 5.0 wt %.

Block copolymer	L_{gas}/L_{liq}	Q_{gas} μL min^{-1}	Q_{liq} μL min^{-1}	Q_{total} μL min^{-1}
PCL$_{2100}$-*b*-PEG$_{5000}$				
Prep 1	1.1	107.8	100.0	207.8
Prep 2	1.1	116.4	100.0	216.4
Prep 3	1.1	109.4	100.0	209.4
Empty PNPs 1	0.9	94.9	100.0	194.9
PCL$_{6000}$-*b*-PEG$_{5000}$				
Prep 1	1.0	101.3	100.0	201.3
Prep 2	1.1	106.9	100.0	206.9
Prep 3	1.0	105.2	100.0	205.2
Empty PNPs 2	1.1	117.9	100.0	217.9
PCL$_{12000}$-*b*-PEG$_{5000}$				
Prep 1	1.1	113.7	100.0	213.7
Prep 2	1.1	108.6	100.0	208.6
Prep 3	1.0	104.8	100.0	204.8
Empty PNPs 3	1.1	109.0	100.0	209.0

Table 2-2. Actual gas and liquid flow rates for various preparations of Py-PNPs; for all preparations in this table, PCL_{2100}-*b*-PEG_{5000} block copolymer used, Q = 200 μL min^{-1} and water content = cwc + 5.0 wt%.

Loading ratio, *r*	L_{gas}/L_{liq}	Q_{gas} μL min^{-1}	Q_{liq} μL min^{-1}	Q_{total} μL min^{-1}
0				
Empty PNPs 1	0.9	94.9	100.0	194.9
0.01				
Prep 1	0.9	97.2	100.0	197.2
Prep 2	0.9	92.1	100.0	192.1
Prep 3	1.1	106.9	100.0	206.9
0.1				
Prep 1	1.0	107.8	100.0	207.8
Prep 2	1.1	116.4	100.0	216.4
Prep 3	1.1	109.3	100.0	209.3
0.5				
Prep 1	1.1	107.8	100.0	207.8
Prep 2	1.1	116.4	100.0	216.4
Prep 3	1.1	109.3	100.0	209.3
0.75				
Prep 1	0.9	96.9	100.0	196.9
Prep 2	1.0	104.3	100.0	204.3
Prep 3	0.9	96.5	100.0	196.5

Table 2-3. Actual gas and liquid flow rates for various preparations of Py-PNPs; for all preparations in this table, PCL_{2100}-*b*-PEG_{5000} block copolymer used, *r* = 0.5 and water content = cwc + 5.0 wt%.

Nominal Flow Rate, *Q*	$\boldsymbol{L_{gas}/L_{liq}}$	$\boldsymbol{Q_{gas}}$ **µL min^{-1}**	$\boldsymbol{Q_{liq}}$ **µL min^{-1}**	$\boldsymbol{Q_{total}}$ **µL min^{-1}**
50 µL min^{-1}				
Prep 1	0.8	21.2	25.0	46.2
Prep 2	0.8	20.6	25.0	45.6
Prep 3	0.8	21.5	25.0	46.5
Empty PNPs 4	1.1	27.7	25.0	52.7
100 µL min^{-1}				
Prep 1	0.8	44.4	50.0	94.4
Prep 2	0.8	43.4	50.0	93.4
Prep 3	0.8	42.5	50.0	92.5
Empty PNPs 5	1.1	58.5	50.0	108.5
200 µL min^{-1}				
Prep 1	1.1	107.8	100.0	207.8
Prep 2	1.1	116.4	100.0	216.4
Prep 3	1.1	109.3	100.0	209.3
Empty PNPs 1	0.9	94.9	100.0	194.9
400 µL min^{-1}				
Prep 1	0.9	186.6	200.0	386.6
Prep 2	0.9	183.9	200.0	383.9
Prep 3	0.9	181.3	200.0	381.2
Empty PNPs 6	1.1	237.2	200.0	437.2

Table 2-4. Actual gas and liquid flow rates for various preparations of Py-PNPs; for all preparations in this table, PCL_{2100}-*b*-PEG_{5000} block copolymer used, Q = 200 μL min^{-1} and r = 0.5.

Water content	L_{gas}/L_{liq}	Q_{gas} / μL min^{-1}	Q_{liq} / μL min^{-1}	Q_{total} / μL min^{-1}
cwc + 2.0 wt%				
Prep 1	0.9	89.5	100.0	189.5
Prep 2	0.9	93.4	100.0	193.4
Prep 3	0.9	96.3	100.0	196.3
Empty PNPs 7	0.8	86.5	100.0	186.5
cwc + 5.0 wt%				
Prep 1	0.9	88.9	100.0	188.9
Prep 2	0.9	87.2	100.0	187.2
Prep 3	0.8	85.8	100.0	185.8
Empty PNPs 1	0.9	94.9	100.0	194.9
cwc + 10.0 wt%				
Prep 1	1.1	107.8	100.0	207.8
Prep 2	1.2	116.4	100.0	216.4
Prep 3	1.1	109.4	100.0	209.4
Empty PNPs 8	1.0	101.3	100.0	201.3
cwc + 20.0 wt%				
Prep 1	0.9	93.5	100.0	193.5
Prep 2	0.9	92.7	100.0	192.7
Prep 3	0.9	91.1	100.0	191.1
Empty PNPs 9	1.0	98.3	100.0	198.3

2.5. Microfluidic Preparation of Pyrene-Loaded Polymer Nanoparticles (Py-PNPs)

PNPs containing various quantities of pyrene were prepared using a microfluidic nanoprecipitation method. For microfluidic preparation of Py-PNPs, the following three fluid streams were combined to form gas-segmented liquid plugs within the reactor (1) 1.0 wt % PCL2.1k, PCL6.0k, or PCL12k in DMF containing variable amounts of co-dissolved pyrene, described by the initial dye-to-polymer ratios r_{Py} (w/w), where r_{Py} = 0.01, 0.1, 0.5 or 0.75; (2) pure DMF; and (3) DMF/deionized (DI) water (water compositions selected to give on-chip water contents of cwc + 2.0 wt %, cwc + 5.0 wt %, cwc + 10.0 wt % or cwc + 20.0 wt %).

The flow rates of the three liquid streams were equal for all runs such that the steady state on-chip copolymer concentration was 0.33 wt %. Different water contents were selected relative to the cwc values for each copolymer. For instance, using a PCL2.1k copolymer, the determined cwc was 12.7 wt % and using the condition requiring cwc + 2.0 wt % on-chip, corresponds to 14.7 wt % water on-chip and 44.1 wt% water in the DMF-water stream inlet (i.e. 3× water-content required on-chip). For each Py-PNP preparation, the sample was collected from the chip into vials containing 10× excess by volume of deionized water. In order to remove residual DMF, the resulting samples were then dialyzed (6−8 kDa MWCO dialysis membrane, Spectrum Laboratories) against deionized water for 18 h, with changing of water every hour for the first 4 h. Precipitated drug in the aqueous samples was removed by centrifugation at 16000 × g for 10 min; the resulting dispersions were designated Py-PNPs.

Empty PNPs dispersions in water were also prepared using the identical set of conditions as described above except without using any pyrene ($r_{Py} = 0$) as listed in Table 2-1 to 2-4. These preparations were essential to correct steady-state emission measurements for Py-PNPs by subtracting emission of empty PNPs as further described in section 2.7.5.

2.6. Dynamic Light Scattering (DLS)

DLS measurements were carried out for determination of hydrodynamic sizes and polydispersities of Py-PNPs. DLS experiments were performed on Zeta PALS Analyzer (Brookhaven Instruments Corporation, Holtsville, NY), a benchtop light scattering equipment measuring at a fixed scattering angle of 15° and a temperature of 23 ± 0.1 °C (Figure 2-8). PNP concentrations for all DLS measurements were ~0.03 mg/mL. To prepare samples for DLS measurements, ~0.5 mL aliquots of Py-PNPs were transferred to a clean glass cuvette and then ~2 mL of deionized water was added that had been pre-filtered through 2 × 0.20 μm Nylon syringe filters (National Scientific) in series. The resulting dispersions were allowed to equilibrate for 15 min before a DLS measurement. For each PNP dispersion, mean effective hydrodynamic sizes and polydispersities were determined from three independent measurements of the autocorrelation function using cumulant analysis.

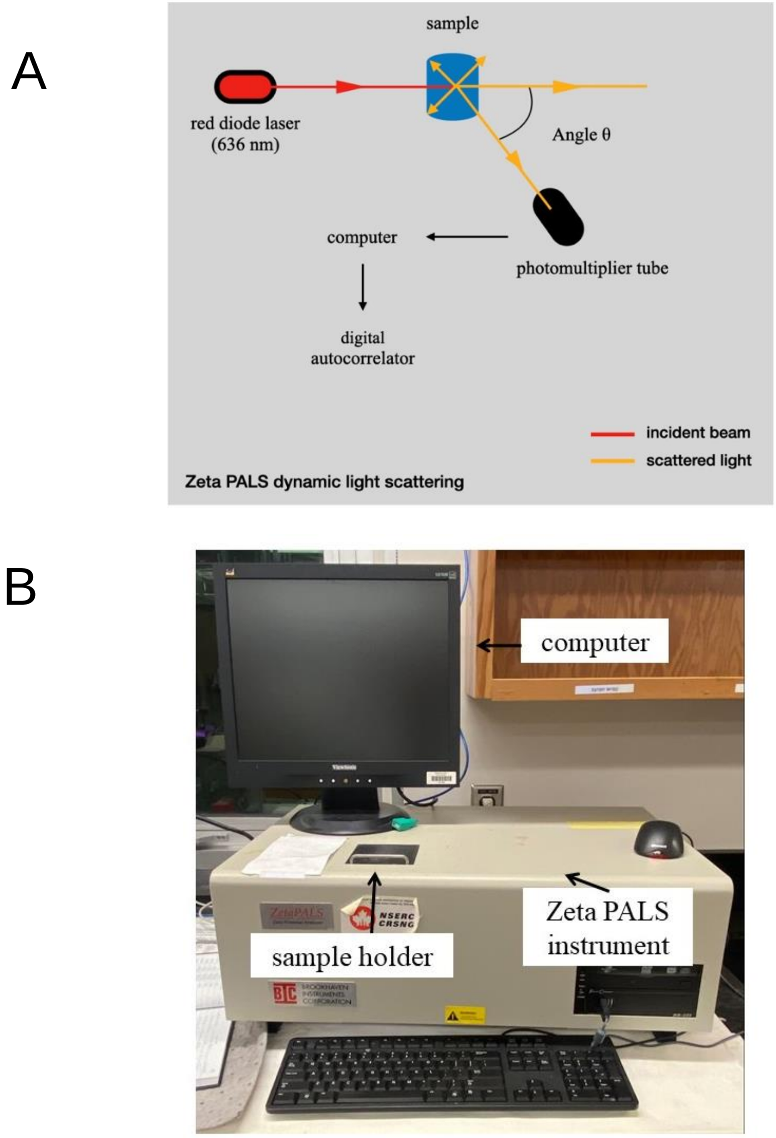

Figure 2-8. (a) Schematics of dynamic light scattering measurements on Zeta PALS (b) an image of the Zeta PALS instrument.

Reported mean effective hydrodynamic sizes and polydispersities for each condition were determined by averaging values from triplicate preparations. Standard errors (σ) on hydrodynamic sizes and polydispersities were calculated from the standard deviation (s) of triplicate values: $\sigma = \frac{s}{\sqrt{3}}$.

2.7. Fluorescence Spectroscopy

2.7.1. Sample Preparation

All the fluorescence emission measurements were carried out in a 10 x 10 mm quartz cuvette. Before using the cuvette for any measurement, it was washed six times with methanol, subsequently six times with deionized water and then air dried. After this, a cell check was performed on the PTI-QM40 fluorimeter using only solvent (water) to make sure there were no trace of contaminants. After each addition of a sample, the cuvette was rinsed three times with methanol and then three times with deionized water.

2.7.2. Pyrene Purity

Pyrene purchased from Sigma Aldrich was >99% pure (fluorescent grade). The purity of pyrene was checked by the method described by Bohne group.[8,13] Time-resolved fluorescence experiments (λ_{ex} = 335 nm, λ_{em} = 383 nm) were carried out for a 0.5 μM pyrene solution in water, where a monoexponential decay (133 ns, Figure 2-9) indicated that the pyrene used was pure. Many of these time-resolved measurements were done with the help of Ankur Awasthi from Bohne lab.

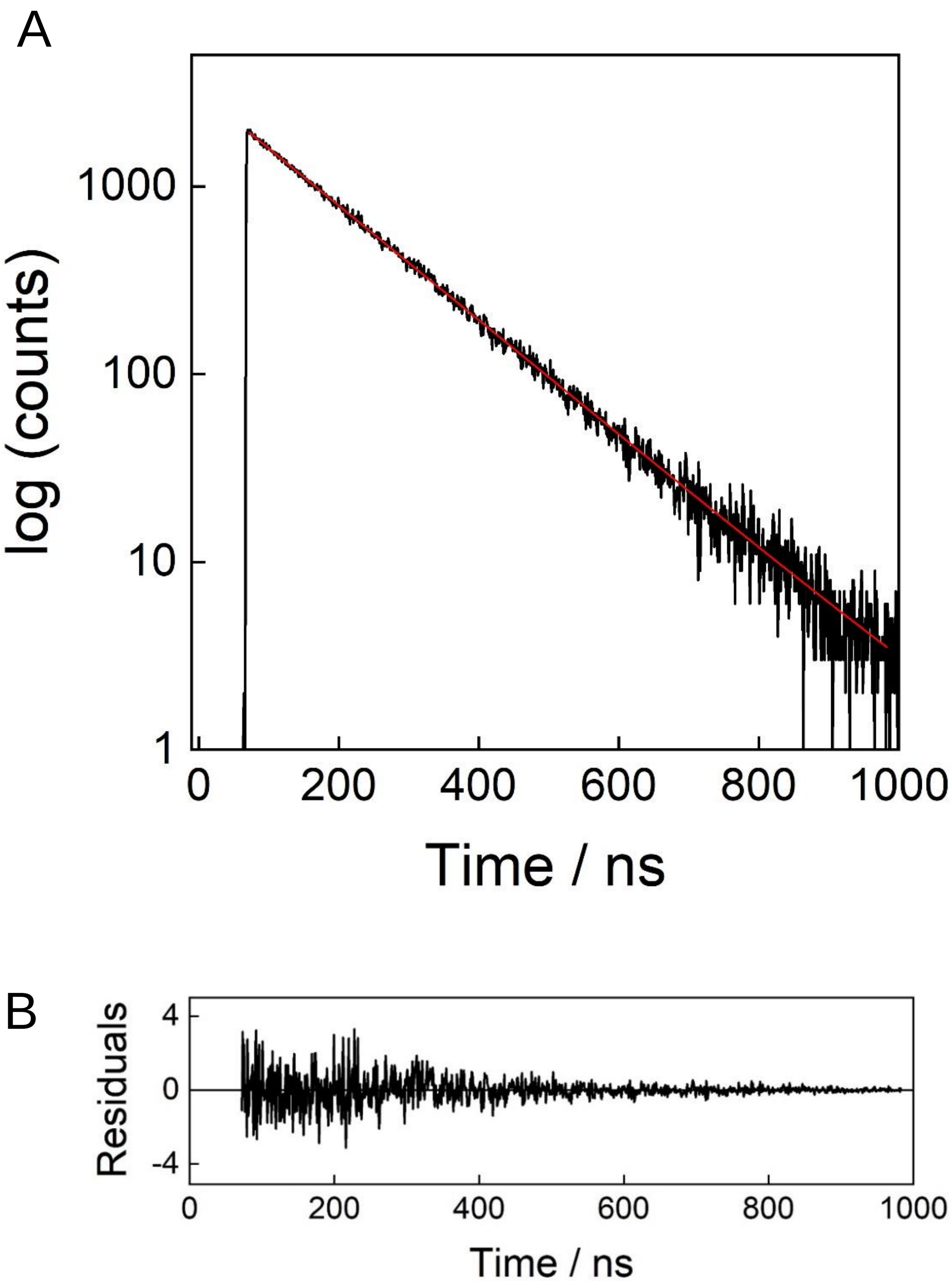

Figure 2-9. (a) Time-resolved fluorescence of a pure pyrene solution exhibiting a mono exponential decay and fitted curve (red) to obtain a single lifetime of pyrene around 133-134 ns (b) Residuals from the fitted exponential time-resolved curve.

2.7.3. Steady-state emission measurements

All steady-state fluorescence emission spectra were collected using a PTI QM-40 fluorimeter (Figure 2-10).

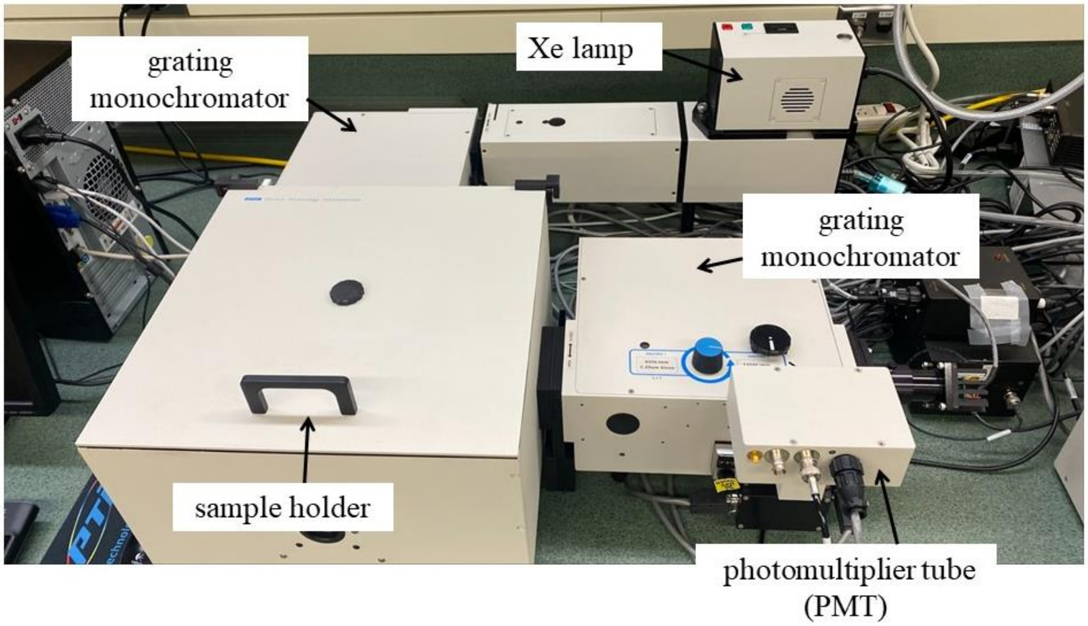

Figure 2-10. An image showing the PTI QM-40 Fluorimeter that is used for all steady-state fluorescence measurements in this thesis.

For all measurements, emission spectra were recorded between λ_{em} = 350 nm and λ_{em} = 650 nm in order to observe the full excimer emission region, using a single excitation wavelength of λ_{ex} = 331 nm. The temperature was held constant at 20.0 ± 0.1 °C for all measurements. For all fluorescence measurements, the step size was 0.25 nm, the integration time was 0.5 s, and the slits for both monochromators were set to 1 nm bandwidths.

All raw fluorescence spectra were treated with an instrument correction applied by the FelixGx software installed on PTI QM-40 instrument that accounted for differences in the efficiencies of the lamp, optics, grating, mirrors and detector at different wavelengths. An example of the instrument correction applied to a spectrum of Py in acetonitrile is shown in Figure 2-11. Moreover, a correction for the emission monochromator was applied to all solutions of Py in solvent (water or acetonitrile) and Py-PNPs in water due to a calibration problem with emission monochromator. This was done by collecting Raman peak emission for water and finding the difference between Raman peak positions before and after the instrument was calibrated (Figure 2-12). An offset of 5.0 nm in the emission wavelength range was found for all recorded spectra of Py in solvent and Py-PNPs in water. This offset was corrected by applying a red shift of 5.0 nm to all recorded Py emission spectra in sections 2.7.4. and 2.7.5. In addition to these corrections, fluorescence measurements of Py-PNPs in water required further corrections which are described in section 2.7.5.

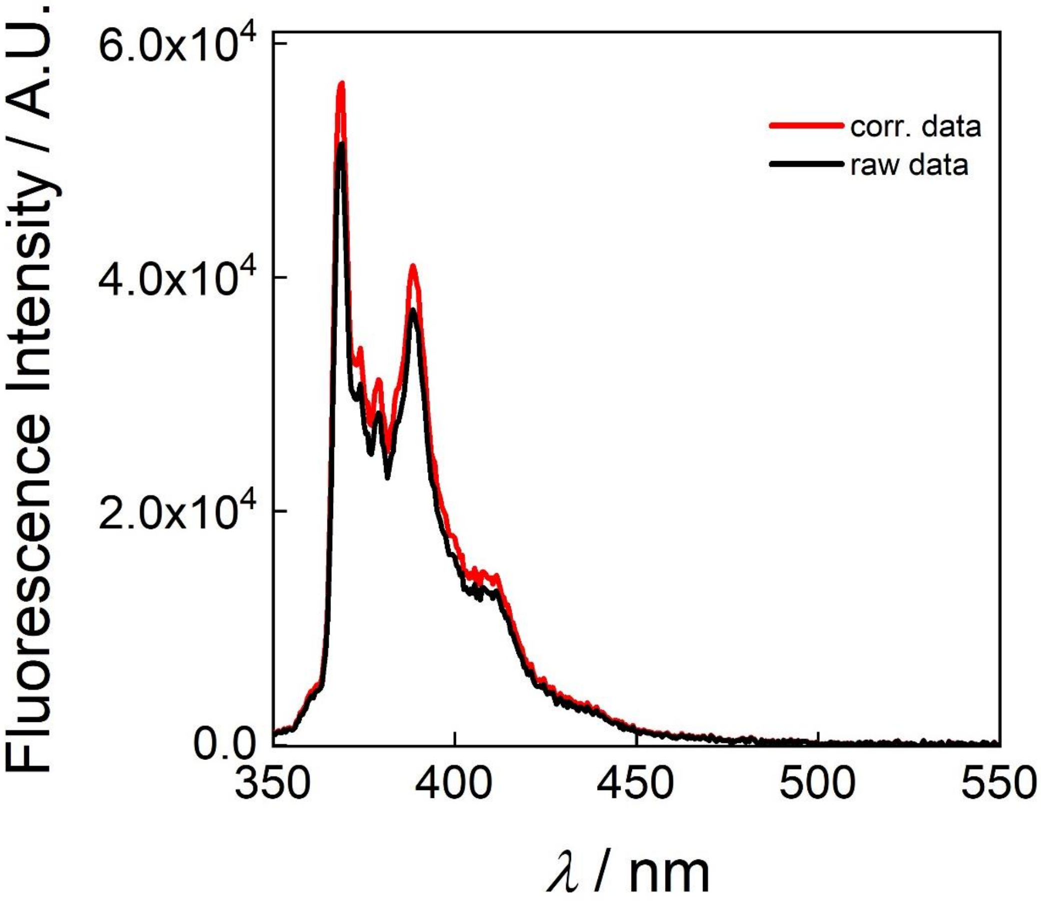

Figure 2-11. Steady state emission spectra of 0.5 μM pyrene in acetonitrile showing both raw data (black curve) the corrected (corr.) spectrum after applying the instrument correction.

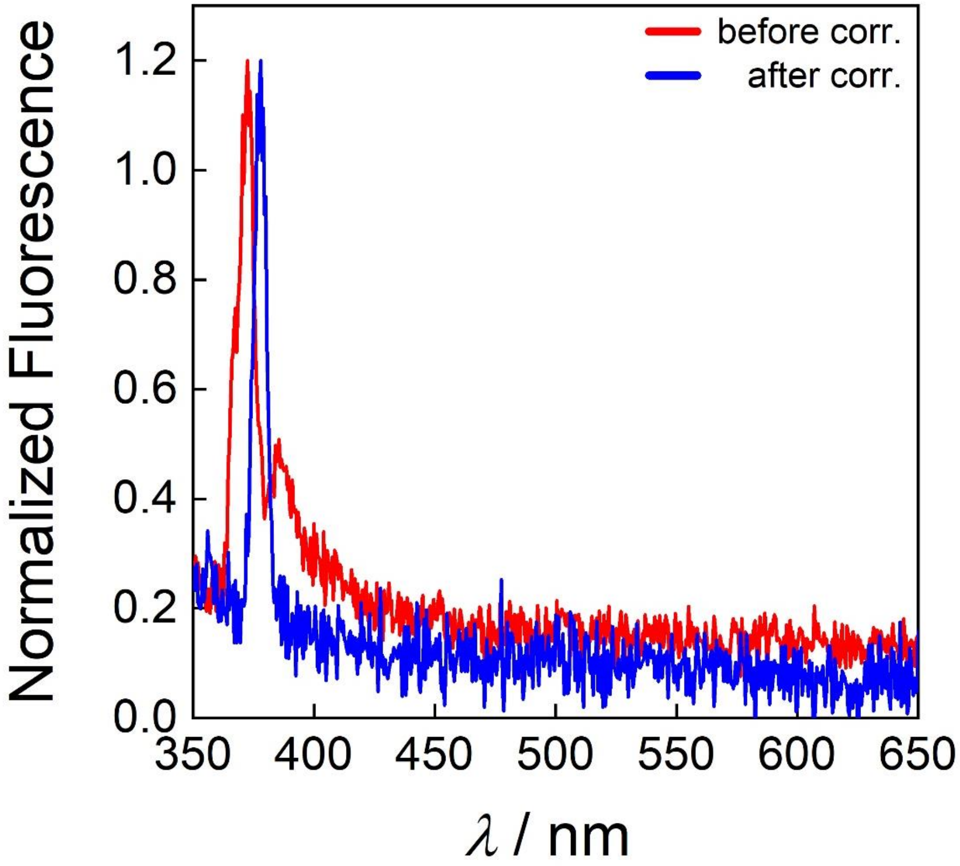

Figure 2-12. Normalized steady state emission spectra of water solvent showing the offset of emission monochromator on raman peak emission of water before and after monochromator calibration.

2.7.4. Determination of Pyrene Encapsulation Efficiency and Loading

To determine the dye encapsulation efficiency, water was removed from ~0.3 g of a gravimetrically determined quantity of Py-PNPs by rotary evaporation for 15 min at 25 °C, followed by addition of a known gravimetrically determined quantity of acetonitrile (~0.5 g) and overnight stirring to ensure complete dissolution of all solids. This ensured that Py was released from the Py-PNPs and was dispersed in the same acetonitrile environment as the calibration standards for these measurements.

Fluorescence intensity–concentration calibration curves for pyrene at the I_3 emission maxima (λ_{em} = 383 nm, λ_{ex} = 331 nm) in acetonitrile were determined in a range of concentrations from 0.5 – 6 μM (Figure 2-13, 2-14), after following the instrument and monochromatic correction of the raw data. No further correction for solvent or copolymer emission was carried out on spectra of pyrene standards and pyrene samples derived from dissolved Py-PNPs in acetonitrile. This is because I_3 emission peak is used for standards calibration as it is independent of microenvironment (solvent) interactions.[10]

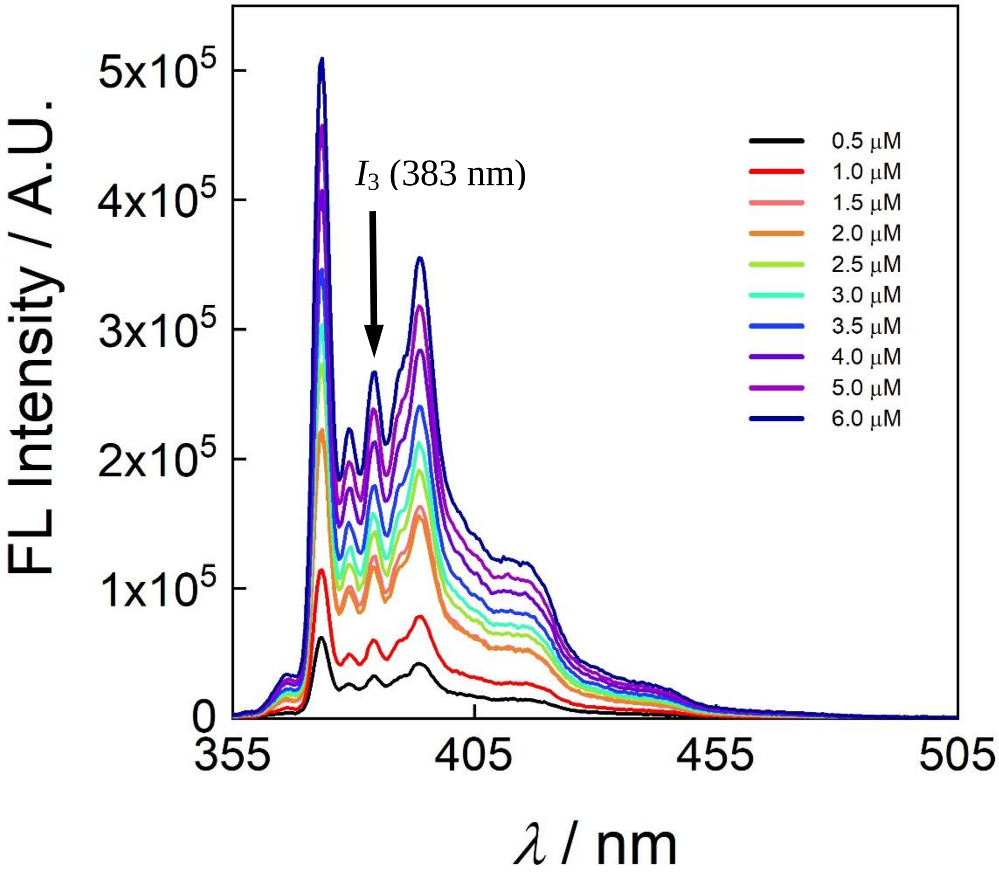

Figure 2-13. Steady-state emission spectra for pyrene in acetonitrile with concentrations ranging 0.5 – 6 μM. The I_3 peak (λ_{em} 383 nm) is used for preparing standard calibration curves.

These standard calibration plots were used to determine the unknown pyrene concentration in the Py-PNPs samples. Thus, the fluorescence intensities of dissolved nanoparticle solutions were measured at the same wavelengths and under identical conditions to those of the calibration standards, just after obtaining the calibration curves. Since fluorescence is a relative measurement and the emission intensity is sensitive to instrument factors, all the calibration curve and loading measurements were done on the same day.

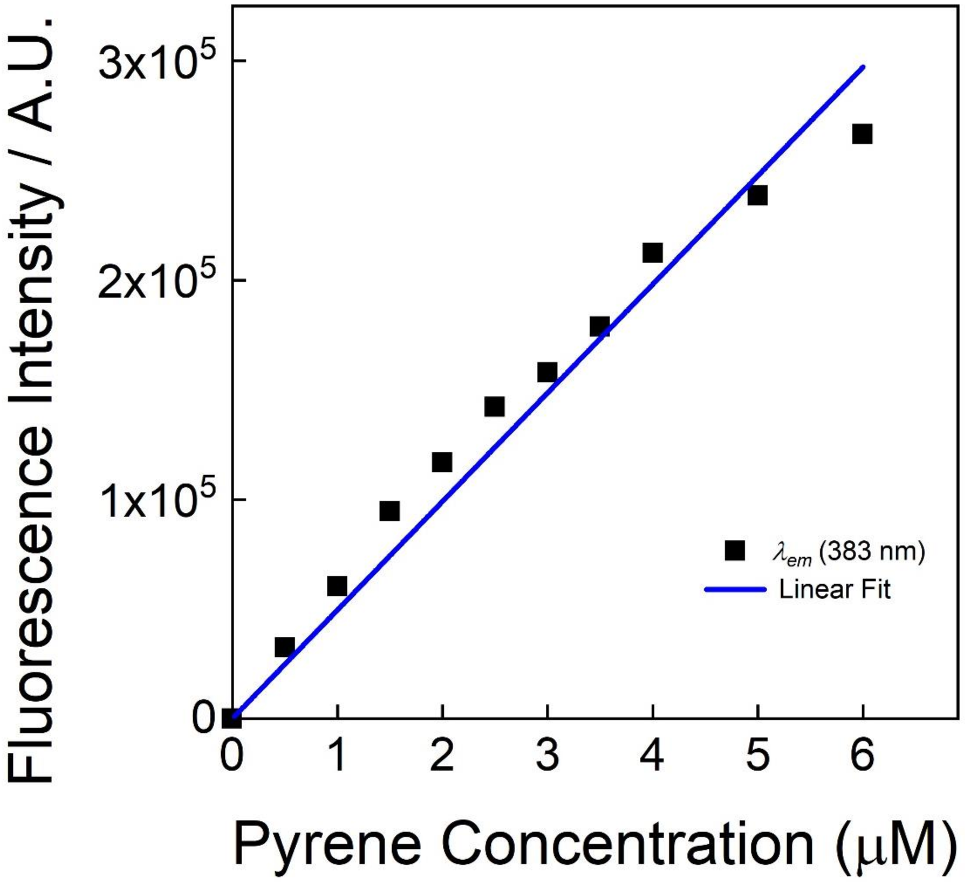

Figure 2-14. A linear pyrene calibration plot (at λ_{em} = 383 nm) used to determine the encapsulation and loading efficiency of Py-PNPs; concentrations range from 0.5 – 6.0 μM.

The dye concentrations were then determined from the calibration curves. After correcting for dilution factors, the mass of the encapsulated pyrene was determined and thus, we obtained the encapsulation efficiency (EE) and dye loading (DL) using the following expressions:

$$EE = \frac{mass\ encapsulated\ pyrene}{total\ mass\ of\ pyrene} \times 100\ \%$$

$$DL = \frac{mass\ encapsulated\ pyrene}{mass\ encapsulated\ pyrene + total\ mass\ PCL} \times 100\ \%$$

r_{Py} is the initial loading ratio, described as the initial mass ratio of pyrene to copolymer:

$$r_{Py} = \frac{total\ mass\ pyrene}{total\ mass\ copolymer}$$

f_{PCL} is the mass fraction of PCL in the copolymer:

$$f_{PCL} = \frac{total\ mass\ PCL}{total\ mass\ copolymer}$$

DL is related to the initial loading ratio and mass fraction of PCL such that:

$$DL = \frac{(r_{Py}/f_{PCL})\ \times (\frac{EE}{100})}{(r_{Py}/f_{PCL})\ \times (\frac{EE}{100}) + 1} \times 100\ \%$$

Reported mean encapsulation efficiency (EE) and dye loading (DL) for each condition were determined by averaging values from triplicate preparations. Standard errors (σ) on EE and DL were calculated from the standard deviation (s) of triplicate values: $\sigma = \frac{s}{\sqrt{3}}$.

2.7.5. Steady-state Emission Analysis of Py-PNPs in Water

Steady-state emission of Py-PNPs in water were obtained using PTI QM 40 fluorimeter. For these measurements, the Py was measured within the intact Py-PNPs instead of being released from the PNPs as in the measurements described in the previous section. The emission spectra were obtained using the same instrument settings as described in section 2.7.2. The sample containing Py-PNPs in water was prepared for emission analysis after determining the concentration of pyrene in the sample as described in the previous section (section 2.7.4). Samples were prepared by adding DI water to the Py-PNP stock in order to adjust the concentration of pyrene to between 0.5 – 0.6 μM for each emission measurement.

After each measurement, an instrument and monochormatic correction was applied as described in section 2.7.2. Then, from the instrument-corrected emission spectra, an emission spectrum of empty PNPs in water were subtracted (Figure 2-15). The final corrected emission spectra were used for all further analysis of Py-PNPs.

The final corrected emission spectra were then deconvoluted using Origin Pro as shown in Figure 2-15. Five individual monomer peak maxima (λ = 373.0, 378.5, 383.0 , 393.0 and 413.0nm) in the monomer region and one peak maxima in the excimer region (λ = 483.0 nm) were identified and used to fix the positions of six Lorentzian peak contributions to the fit (Figure 2-16A).[9] Thus, the fluorescence emission data were fit to a sum of 6 Lorentzian functions; the resulting monomer peaks were then combined in order to obtain deconvoluted monomer and excimer emission contributions of pyrene in Py-PNPs (Figure 2-16B).[9] Then, the monomeric emission maxima at I_1 (λ_{em} = 373.0 nm) and I_3 (λ_{em} = 383.0 nm) were taken from the combined monomer curve to obtain the I_1/I_3 ratios (Figure 2-16B). The excimer emission maxima at I_e (λ_{em} = 478.0 nm) from the deconvoluted excimer curve and the I_3 emission maxima from the combined monomer curve were used to obtain the I_e/I_m ratios (Figure 2-16B).

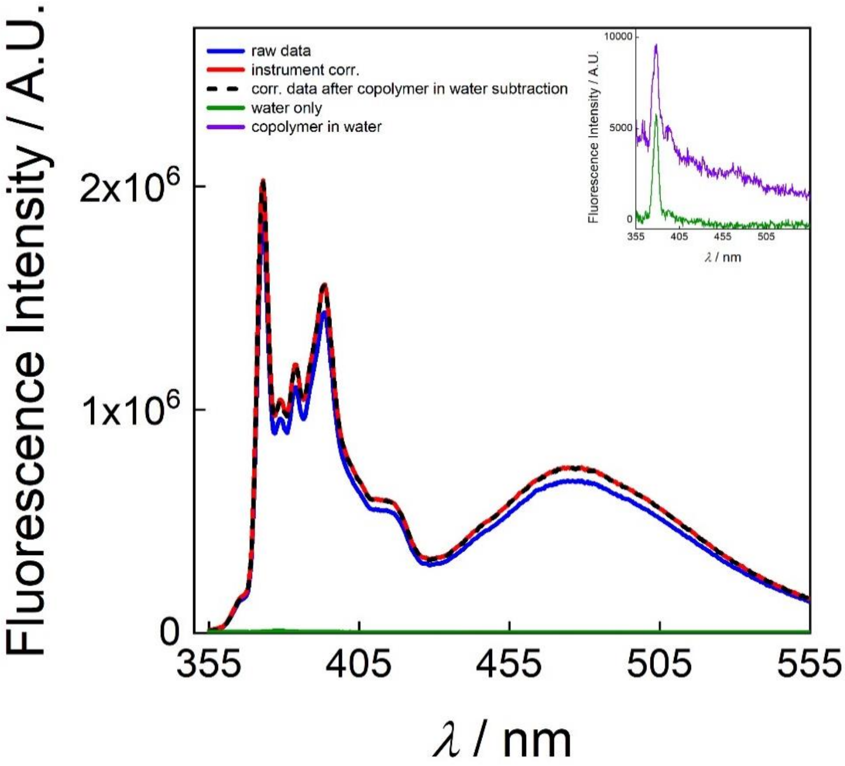

Figure 2-15. Step-by-step corrections of steady state emission spectra of a sample containing Py-PNPs. The emission spectrum of solvent and copolymer in solvent are shown in the inset.

Reported I_1/I_3 ratios and I_e/I_m ratios for each condition were determined by averaging values from triplicate preparations. Standard errors (σ) on I_1/I_3 ratios and I_e/I_m ratios were calculated from the standard deviation (s) of triplicate values: $\sigma = \frac{s}{\sqrt{3}}$.

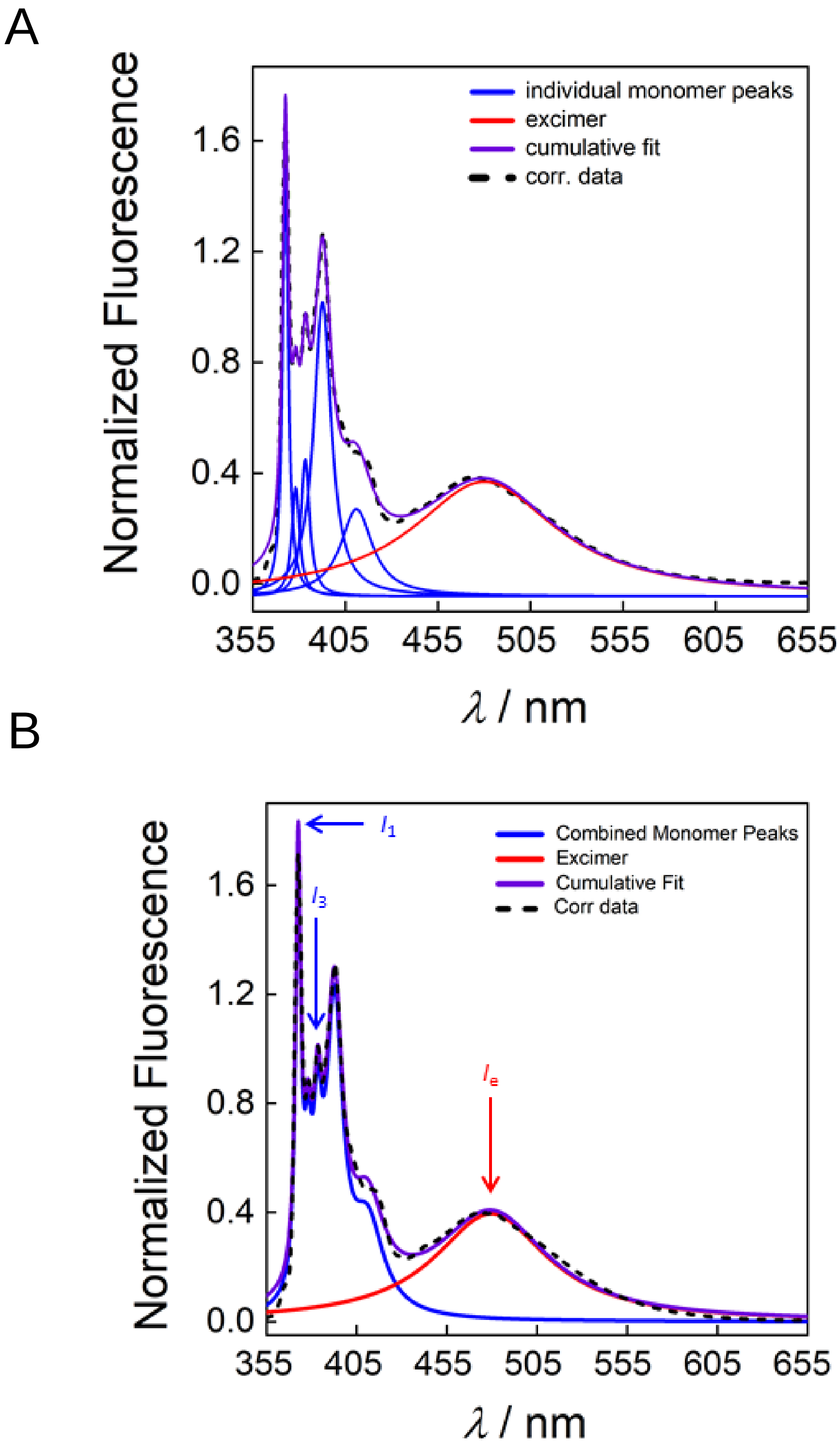

Figure 2-16. Deconvolution of a normalized (λ = 383 nm) emission spectra of Py-PNPs (a) all individual monomer peaks (blue) and excimer (red) deconvoluted (b) combined monomeric peaks (blue) and excimer (red).

To assess the validity of the excimer subtraction procedure described in Figure 2-16, for specific conditions (described in section 3.2.3.) we compared I_1/I_3 obtained using this method with ratios obtained using an alternative method described in Figure 2-17. In the alternative method, I_1/I_3 was not determined from the combined deconvoluted monomer peaks. Instead, the deconvoluted excimer peak (red data, Figure 2-17) was subtracted from the corrected emission spectrum (black dashed data) to obtain the monomer emission spectrum (light brown data). The I_1/I_3 value was then determined from the monomer emission spectrum.

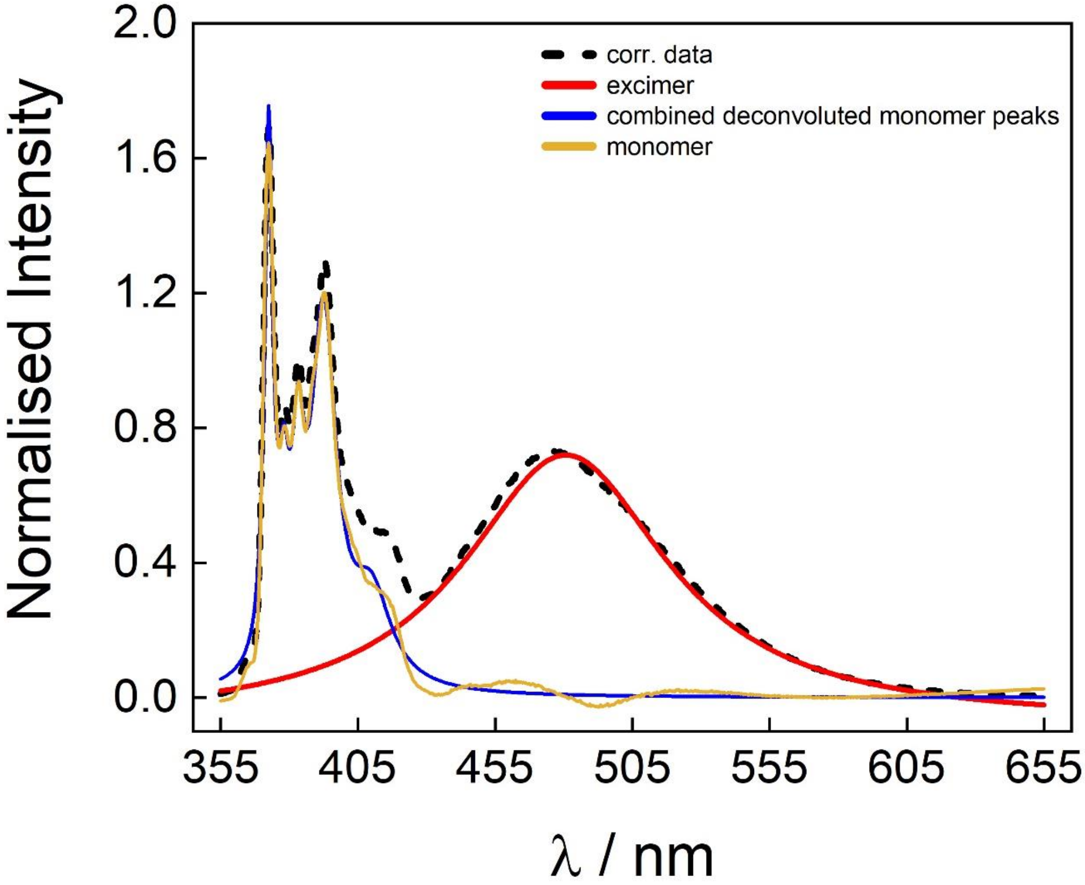

Figure 2-17. Deconvolution of a normalized (λ = 383 nm) emission spectra of Py-PNPs showing the monomer emission (light brown) using alternative method.

2.8. X-ray Diffraction

X-ray diffraction measurements were performed on a Rigaku Miniflex diffractometer with a Cr source (kR radiation, k = 2.2890 Å) operating at 30 kV and 15 mA with a resolution of 0.05° (2θ) and a scan speed of 1°/min (Figure 2-18). X-ray diffraction profiles were collected for 2θ ranging from 10° to 80°.

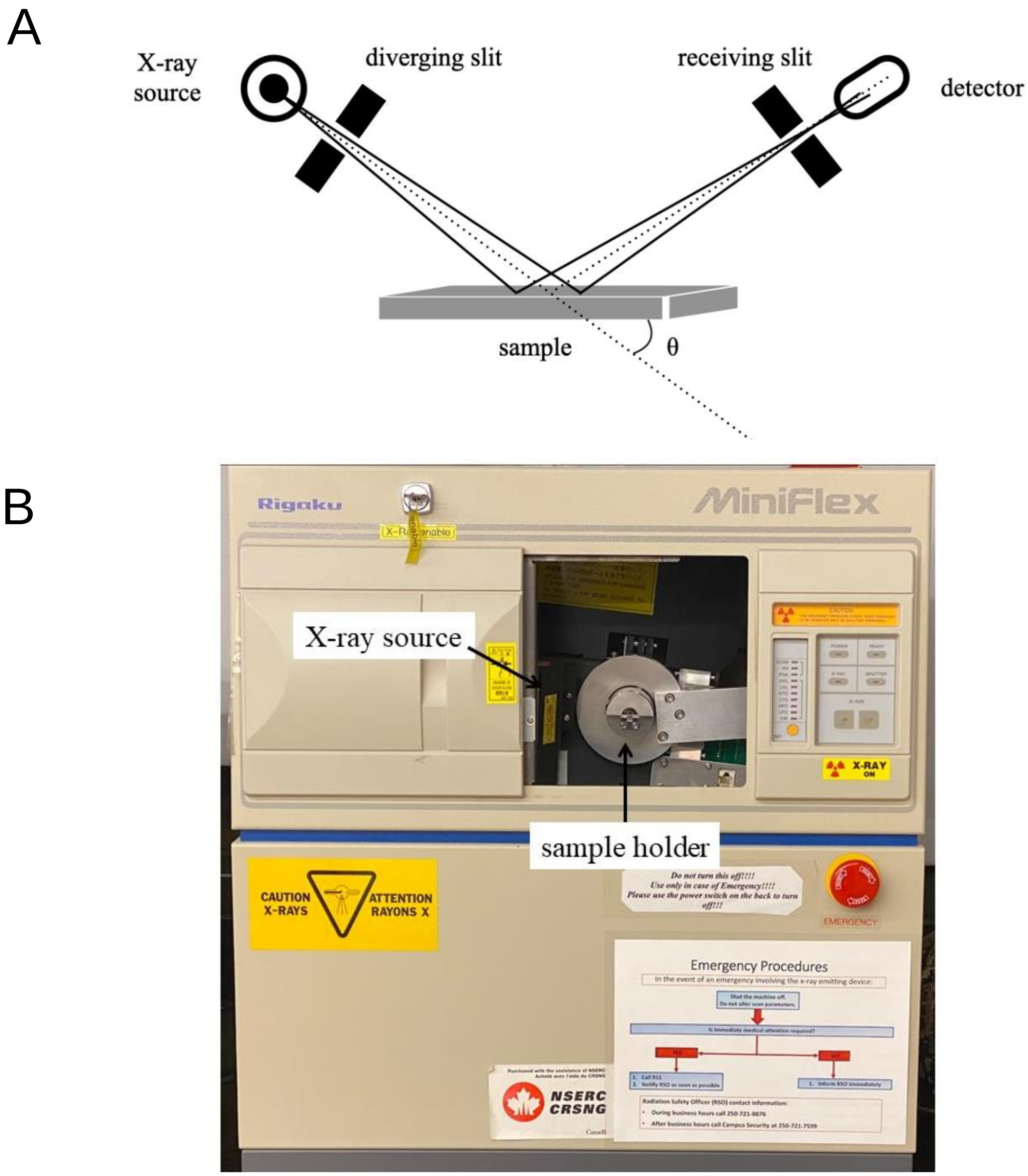

Figure 2-18. (a) Schematics of x-ray diffraction measurements on Rigaku Miniflex diffractometer (b) an image of the instrument.

For XRD sample preparation, water was removed from suspensions of Py-PNPs by rotary evaporation at 25 °C until solid films were obtained. The resulting films were then scraped as a powder into the zero background XRD specimen holder with no subsequent drying step to remove residual solvent. We note that this preparation method will significantly increase the crystallinity of coronal PEO blocks relative to their colloidal state, as removal of water from the nanoparticle coronae will allow initially solubilized PEO chains to pack together. However, since the hydrophobic cores will contain no water in the purely aqueous suspensions, we do not expect the crystallinity of the core-forming PCL blocks to be strongly affected when water is removed by rotary evaporation. Therefore, our XRD experiments should provide a reasonable probe of nanoparticle core crystallinity in the colloidal state.

Peak deconvolution of XRD data was done using Origin Pro as shown in Figure 2-19. Two characteristic reflections for each of crystalline PCL and crystalline PEO were identified from the literature and these were used to fix the positions of four Lorentzian peak contributions to the fit.[11,12] Thus, XRD data were fit to a sum of 5 Lorentzian functions: 2 peaks assigned to crystalline PCL (2θ = 32.5° and 35.7°), 2 peaks assigned to crystalline PEO (2θ = 28.2°, 35.4°), and 1 peak (no fixed position) assigned to incoherent scattering from amorphous copolymer (amorphous halo).

Areal peak contributions from the three components (crystalline PCL, A_{PCL}; crystalline PEO, A_{PEO}; and amorphous copolymer, $A_{\mathrm{amorphous}}$) were then determined by integration. The percentage of mass of crystalline PCL relative to the mass of the entire PNP (PCL core + PEO corona), $\chi_{\mathrm{PCL,PNP}}$ was defined as follows:

$$\chi_{\mathrm{PCL,PNP}} = \frac{m_{PCL,crys}}{m_{total}} \times 100\ \%$$

where $m_{\mathrm{PCL,crys}}$ is the mass of crystalline PCL and m_{total} is the mass of copolymer in the sample. $\chi_{\mathrm{PCL,PNP}}$ was calculated from areal peak contributions as follows:

$$\chi_{\mathrm{PCL,PNP}} = \frac{A_{PCL}}{A_{total}} \times 100\ \%$$

$$\text{where } A_{total} = A_{PCL} + A_{PEO} + A_{amorphous}$$

The mass percentage of PCL to each of the three copolymers, P_{PCL} is defined as:

$$P_{\mathrm{PCL}} = \frac{m_{PCL}}{m_{total}} \times 100\ \%$$

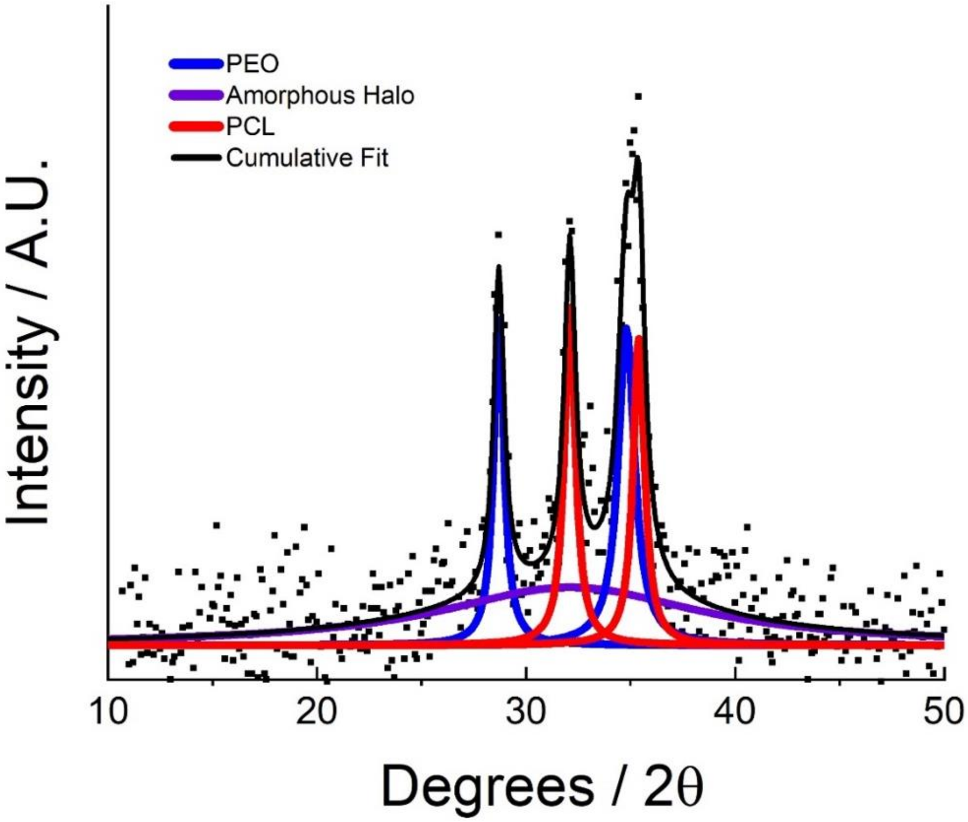

Figure 2-19. Representative XRD profile of a sample of Py-loaded PCL-*b*-PEO nanoparticles, showing raw data, best fit function (black), and crystalline PCL (red), crystalline PEO (blue) and amorphous (purple) Lorentzian contributions to the fit. This sample was prepared using the PCL6k copolymer under the following formulation conditions: $Q = 200$ µL/min, $r = 0.1$, and a water content of cwc + 5 wt %.

Finally, the percentage of crystalline PCL relative to the mass of the PNP core (amorphous PCL + crystalline PCL), $\chi_{\mathrm{PCL,core}}$ was defined as follows:

$$\chi_{\text{PCL,core}} = \frac{m_{PCL,crys}}{m_{PCL}} \times\ 100\ \%$$

and was calculated as follows using $\chi_{\text{PCL,PNP}}$ determined from x-ray peak areas and P_{PCL} determined from the copolymer composition:

$$\chi_{\text{PCL,core}} = \frac{\chi_{\text{PCL,PNP}}}{P_{PCL}} \times\ 100\ \%$$

Reported mean $\chi_{\text{PCL,PNP}}$ and $\chi_{\text{PCL,core}}$ values for each condition were determined by averaging values from triplicate preparations. Standard errors (σ) on $\chi_{\text{PCL,PNP}}$ and $\chi_{\text{PCL,core}}$ were calculated from the standard deviation (s) of triplicate values: $= \frac{s}{\sqrt{3}}$.

2.9. Statistics and Data Handling

For comparison of any two results in a data set, Excel built-in functions were used. The combined standard error SE_c was calculated from the square of the sum if the squares of the SEs from the individual data points:

$$SE_c = \sqrt{{SE_1}^2 + {SE_2}^2}$$

Next, the combined degrees of freedom (DOF) were calculated on the basis of the number of values (N) in each data set:

$$DOF = [(N_1 - 1) + (N_2 - 1)]$$

The difference between measured results (t) was expressed in terms of the difference between mean values, $\bar{x}$, over the combined standard error, SE_c:

$$t = \frac{|\overline{x_1} - \overline{x_2}|}{SE_c}$$

Finally, a p-value was calculated for pairwise comparisons using the TDIST function:

$$p = \ TDIST(t, DOF, 2)$$

where differences were assumed to be statistically significant when $p < 0.05$.

2.10 References

(1) Bains, A.; Wulff, J. E.; Moffitt, M. G. Microfluidic synthesis of dye-loaded polycaprolactone-block-poly (ethylene oxide) nanoparticles: Insights into flow-directed loading and in vitro release for drug delivery, *J. Coll. Interf. Sci.* **2016**, *475*, 136-148.

(2) Bains, A.; Cao, Y. M.; Kly, S.; Wulff, J. E.; Moffitt, M. G. Controlling structure and function of Polymeric Drug Delivery Nanoparticles using Microfluidics, *Mol. Pharm.* **2017**, *14*, 2595–2606.

(3) Chen, R.; Wulff, J. E.; Moffitt, M. G. Microfluidic Processing approach to controlling Drug Delivery properties of Curcumin-loaded Block Copolymer Nanoparticles, *Mol. Pharm.* **2018**, *15*, 4517-4528.

(4) Cao, Y.; Silverman, L.; Lu, C.; Hof, R.; Wulff, J. E.; Moffitt, M. G. Microfluidic Manufacturing of SN-38-loaded polymer nanoparticles with shear processing control of drug delivery properties, *Mol. Pharm.* **2018**, 16, 96-107.

(5) Huang, Y.; Moini Jazani, A.; Howell, E. P.; Oh, J. K.; Moffitt, M. G. Controlled Microfluidic Synthesis of Biological Stimuli-Responsive Polymer Nanoparticles, *ACS Appl. Mater. Interfaces* **2019**, *12*, 177-190.

(6) Huang, Y.; Jazani, A. M.; Howell, E. P.; Reynolds, L. A.; Oh, J. K.; Moffitt, M. G. Microfluidic Shear Processing Control of Biological Reduction Stimuli-Responsive Polymer Nanoparticles for Drug Delivery, *ACS Biomater. Sci. Eng.* **2020**, *6*, 5069-5083.

(7) Abolhasani, M. S.; Kumacheva M. E.; and Günther, A. Automated microfluidic platform for studies of carbon dioxide dissolution and solubility in physical solvents, *Lab on a Chip* **2012**, *12*(9), 1611-1618.

(8) Yihwa, C., Kellermann, M., Becherer, M., Hirsch, A., & Bohne, C. Pyrene binding to persistent micelles formed from a dendro-calixarene, *Photochemical & Photobiological Sciences,* **2007**, *6*, 525-531.

(9) Infelta, P.P. and Grätzel, M., Statistics of Solubilizate Distribution and its application to Pyrene Fluorescence in Micellar Systems: A concise Kinetic model, *The Journal of Chemical Physics*, **1979**, *70(1)*, 179-186.

(10) Kalyanasundaram, K.; Thomas, J. K. Environmental effects on Vibronic Band Intensities in Pyrene Monomer Fluorescence and their application in studies of Micellar Systems, *Journal of the American Chemical Society*, **1977**, *99(7)*, 2039-2043.

(11) N.-V. Cuong, Y.-L. Li and M.-F. Hsieh, Targeted Delivery of Doxorubicin to Human Breast Cancers by Folate-Decorated Star-shaped PEG-PCL Micelle, *J. Mater. Chem*, **2012**, *22*, 1006-1020

(12) A. Bains, Y. Cao and M.G. Moffitt, Multiscale control of Hierarchical structure in Crystalline Block Copolymer Nanoparticles using Microfluidics, *Macromol. Rapid Commun.* **2015,** *36*, 2000-2005.

(13) Xu, W., Demas, J. N., DeGraff, B. A., & Whaley, M. Interactions of pyrene with cyclodextrins and polymeric cyclodextrins. *The Journal of Physical Chemistry*, **1993**, *97*(24), 6546-6554.

Chapter 3 Results & Discussion

3.1. Introduction

In this chapter, we report the results for on-chip loading of the fluorescent probe pyrene (Py) into PCL-*b*-PEO polymer nanoparticles (Py-PNPs) under different chemical and flow conditions within a two-phase segmented microfluidic reactor. The experimental details for this study are described in Chapter 2. As described in Chapter 1, the objective of these experiments is to provide further understanding about how the microenvironment of encapsulated hydrophobic drugs within the PNP core,[1] as reported by Py probe molecules, is impacted by various chemical and structural features of the PNPs, including mean size, internal crystallinity, and drug loading.

The remainder of this chapter is divided into two sections. In section 3.2, we describe the effects of four different experimental variables for Py-PNP preparation on both the physicochemical properties and fluorescence properties of Py-PNPs. Specifically, we describe the effects of PCL block length (3.2.1), initial Py:copolymer loading ratio, r_{Py} (3.2.2), on-chip water content (3.2.3), and microfluidic flow rate, Q (3.2.4), before summarizing and discussing the effects of different experimental variables and the implications of the results for drug delivery formulations (3.2.5). In section 3.3, we combine the different datasets to establish general relationships between physicochemical properties of Py-PNPs, including mean effective hydrodynamic diameters, $d_{\mathrm{h,eff}}$ and drug loading of the PCL core, $\mathrm{DL}_{\mathrm{core}}$, and the Py fluorescence ratios (I_1/I_3 and $I_{\mathrm{e}}/I_{\mathrm{m}}$), which report on the microenvironment of the dye. We do this by determining the dependence of I_1/I_3 and $I_{\mathrm{e}}/I_{\mathrm{m}}$ on linear combinations of

$d_{\mathrm{h,eff}}$ and $\mathrm{DL}_{\mathrm{core}}$. The method and resulting plots are first presented (3.3.1) and then discussed (3.3.2).

3.2. Effects of Nanoparticle Preparation Variables on Physicochemical and Fluorescence Properties of Py-PNPs

3.2.1. Effect of PCL Block Length

We first investigated the effect of the hydrophobic and semicrystalline PCL block length on Py-PNP physicochemical properties ($d_{\mathrm{h,eff}}$, $\mathrm{DL}_{\mathrm{core}}$, and $\chi_{\mathrm{PCL,core}}$) and fluorescence properties (I_1/I_3 and I_e/I_m). For these experiments, we used three different copolymers with mean PCL block molecular weights of 2100, 6000, and 12000 g/mol, and equal mean PEO block molecular weight of 5000 g/mol; the three copolymers are designated PCL2.1k, PCL6.0k, and PCL12k, respectively. All other preparation conditions for self-assembly were kept constant, including microfluidic flow rate (Q = 200 µL/min), initial dye-to-polymer ratio (w/w) ($r_{\mathrm{Py}} = 0.1$) and on-chip water content relative to the cwc (cwc + 5.0 wt %). As reported in Chapter 2, measured cwc values for the three different copolymers in DMF and at a copolymer concentration of 0.33 wt % (equivalent to the on-chip copolymer concentration) were 12.7 wt % (PCL2.1k), 6.3 wt % (PCL6.0k), and 5.7 wt % (PCL12k), such that on-chip water contents of 17.7 wt % (PCL2.1k), 11.3 wt % (PCL6.0k), and 10.7 wt % (PCL12k) were employed. Triplicate preparations were completed for each PCL block length to characterize the resulting Py-PNP properties.

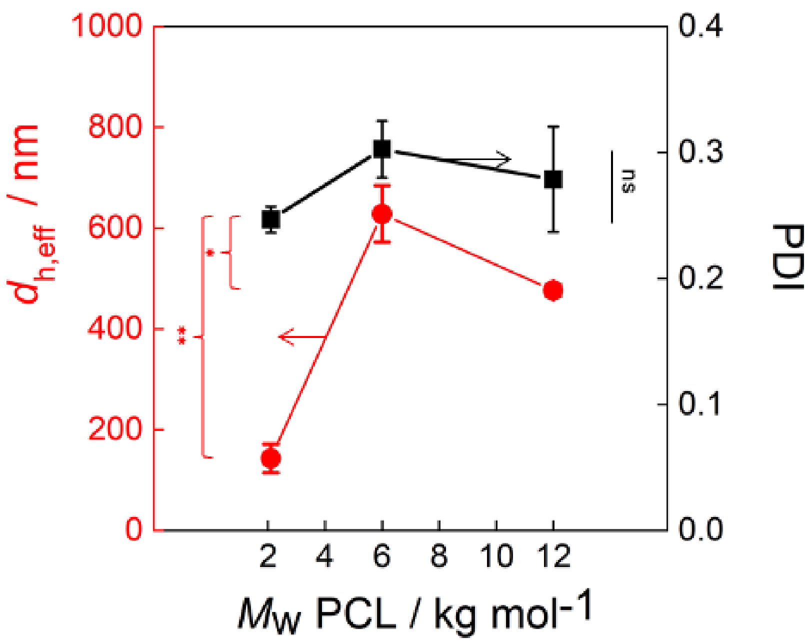

Figure 3-1. Effect of PCL block length on mean effective hydrodynamic diameter, $d_{h,eff}$ (red circles), and polydispersity index, PDI (black squares), of Py-PNPs determined from cumulant analysis of dynamic light scattering (DLS) measurements. All Py-PNPs were prepared with an initial loading ratio of $r_{Py} = 0.1$, and on-chip water content of cwc + 5 wt % and a microfluidic flow rate of $Q = 200$ µL/min. Error bars represent standard errors from triplicate preparations. Brackets indicate statistical comparisons between $d_{h,eff}$ and PDIs of Py-PNPs with different PCL block lengths: ns indicates $p > 0.05$, * indicates $p < 0.05$ and ** indicates $p < 0.005$.

The effect of PCL block length on the hydrodynamic size and polydispersity of Py-PNPs is shown in the Figure 3-1. There is an increase in the colloidal Py-PNP size (including solvated PEO layer) from PCL2.1k to PCL6.0k and then a decrease from PCL6.0k to PCL12k. The average polydispersity of PNPs also increases from PCL2.1k to PCL6.0k and then decreases from PCL6.0k to PCL12k, however the differences are not statistically significant. Corresponding CONTIN analysis shows scattering intensity-weight size distributions for each of the three Py-PNP populations (Figure 3-

2). In general, shorter hydrophobic block lengths tend to favour smaller, spherical PNPs, whereas an increase in the hydrophobic block length favours an increased tendency to form larger morphologies with lower interfacial curvature, including cylinders and vesicles.[2–5] This may explain the observed jump in Py-PNP size between PCL2.1k and PCL6.0k, although the drop in size between PCL6.0k and PCL12k is not well understood. We observe a small drop in the crystallinity of the PCL core between PCL6.0k and PCL12k (*vide infra*), possibly due to slower diffusion kinetics of the higher molecular weight copolymer; since PCL crystallization will also increase the tendency to form larger, lower-curvature morphologies,[6,7] the observed drop in $d_{\mathrm{h,eff}}$ between PCL6.0k and PCL12k could therefore be related to the corresponding drop in the core crystallinity. We note that this explanation is tentative, since the observed small drop in the core crystallinity is statistically insignificant due to experimental error on the measurement (*vide infra*).

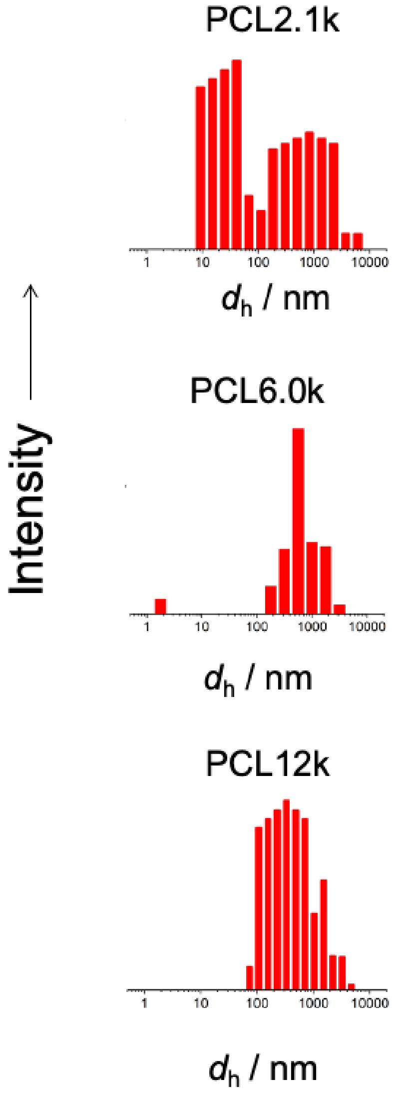

Figure 3-2. Representative CONTIN size distributions from single DLS measurements showing the effect of PCL block length on hydrodynamic diameter distributions of Py-PNPs.

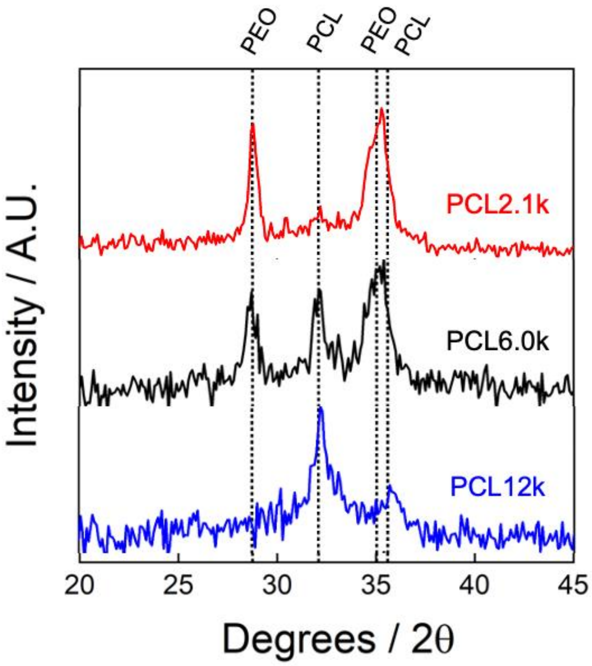

Figure 3-3. Representative powder x-ray diffraction spectra of Py-PNPs showing the effect of PCL block length on copolymer crystallinity. All Py-PNPs were prepared with an initial loading ratio of $r_{\mathrm{Py}} = 0.1$, and on-chip water content of cwc + 5 wt % and a microfluidic flow rate of $Q = 200$ µL/min.

Next, we carried out powder x-ray diffraction (XRD) of dried Py-PNPs from copolymers of the three different PCL block lengths in order to characterize and compare the crystallinities of the PCL core. Although drying the Py-PNPs will induce crystallization of the solubilized PEO corona, it does not have a major impact of the crystallinity of the PCL core, which is determined by on-chip micelle formation and is locked in by removal of DMF during dialysis.[2] Since PEO block lengths are identical for all three copolymers and since PEO crystallization occurred under identical conditions for all three samples, the crystalline PEO peaks in the various XRD spectra in Figure 3.3 serve as internal standards for the comparison of PCL peak intensities between the different samples. Figure 3.3 shows strong differences the relative intensity of crystalline PCL peaks for different PCL block lengths, with an increase in the relative intensity of the major crystalline PCL peak ($2\theta = 32.0°$) compared to the crystalline PEO peaks ($2\theta = 28.7°, 35.0°$) with increasing PCL block length from PCL2.1k (Figure 3-3, top) to PCL12k (Figure 3-3, bottom).

As described in Chapter 2, peak deconvolution was applied to each XRD spectrum and areal contributions from crystalline PCL peaks, crystalline PEO peaks, and the amorphous halo were determined. Then, the various peak areas were used to determine the mass percentage of crystalline PCL relative to the mass of the entire PNP (PCL core + PEO corona), $\chi_{\text{PCL,PNP}}$. Mean $\chi_{\text{PCL,PNP}}$ values for triplicate preparations and associated standard errors are plotted vs. the molecular weight of the PCL block in Figure 3-4A (blue diamonds). Not surprisingly, we find a monotonic increase in $\chi_{\text{PCL,PNP}}$ with increasing length of the PCL block, which is found to track closely with the associated increase in the overall mass percentage of PCL in the copolymers, P_{PCL} (Figure 3-4B, red circles). To separate out the effect of increasing overall PCL mass between the three copolymers, we also calculated the percentage of crystalline PCL relative to the mass of the PNP core (amorphous PCL + crystalline PCL), $\chi_{\text{PCL,core}}$, using the relationship:

$$\chi_{\text{PCL,core}} = \frac{\chi_{\text{PCL,PNP}}}{P_{PCL}} \times 100\ \%$$

Mean $\chi_{\text{PCL,core}}$ values for triplicate preparations and associated standard errors are plotted vs. the molecular weight of the PCL block in Figure 3-4B. The results indicate that between 41-45% of the PCL mass in the Py-PNP cores is crystalline. Although there is a slight apparent decrease in $\chi_{\text{PCL,core}}$ with increasing PCL block length, most notably between the PCL6.0k and PCL12k copolymers, these differences are found to be statistically insignificant within the associated experimental error. We found it quite surprising that the percentage of crystalline material within the cores was so similar for such different PCL block lengths, considering that the thermodynamic driving force for crystallization should be stronger for longer PCL blocks.[8] One explanation is that the slower crystallization kinetics for longer PCL blocks, caused by slower diffusion of the longer copolymer chains,[9] off-sets the stronger thermodynamic driving force, leading to similar $\chi_{\mathrm{PCL,core}}$ values across all three PCL block lengths.

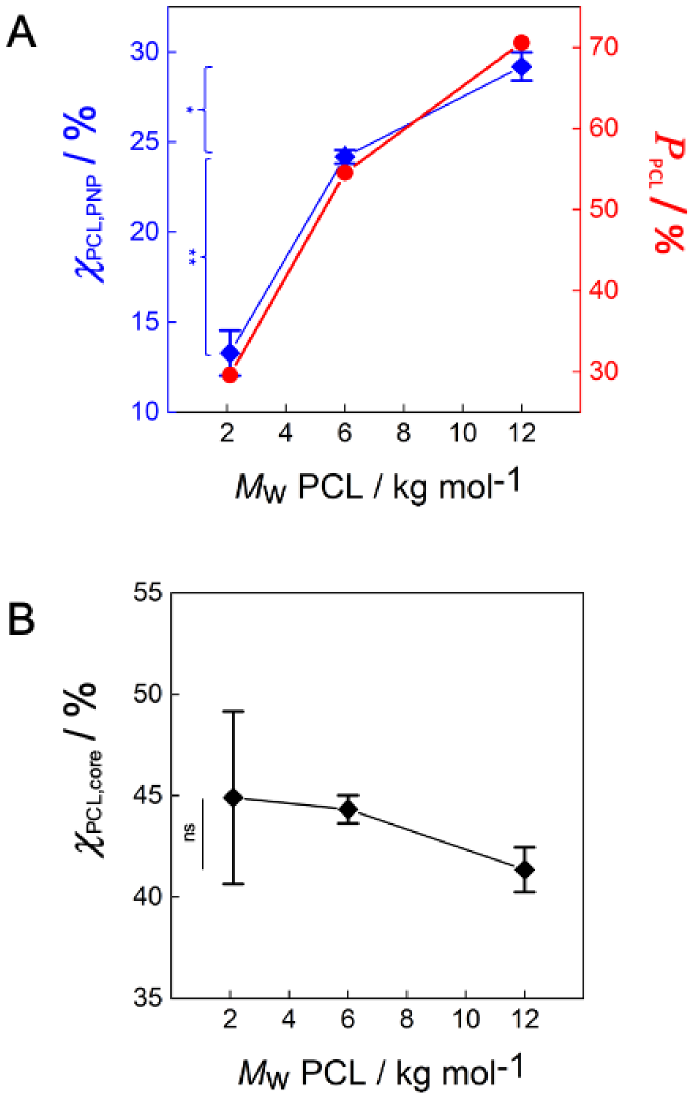

Figure 3-4. Effect of PCL block length on the mass percentage of crystalline PCL relative to the mass of the entire PNP, $\chi_{PCL,PNP}$ (A, blue diamonds) and on the mass percentage of crystalline PCL relative to the mass of the core, $\chi_{PCL,core}$ (B). All Py-PNPs were prepared with an initial loading ratio of $r_{Py} = 0.1$, and on-chip water content of cwc + 5 wt % and a microfluidic flow rate of $Q = 200$ µL/min. Error bars represent standard errors from triplicate preparations. Also shown for comparison is the overall mass of PCL in the copolymers, P_{PCL} (A, red circles). Brackets indicate statistical comparisons between $\chi_{PCL,PNP}$ and $\chi_{PCL,core}$ of Py-PNPs with different PCL block lengths: ns indicates $p > 0.05$, * indicates $p < 0.05$ and ** indicates $p < 0.005$.

Next, in Figure 3-5, we plot the effect of PCL block length on the encapsulation efficiency (EE) and dye loading (DL_{core}). As described in Chapter 2, EE (Figure 3-5, red circles) is the percentage of encapsulated Py relative to the total mass of Py added to the formulation, while DL_{core} (Figure 3-5, blue diamonds) is the mass percentage of encapsulated Py relative to the total mass of Py-PNPs. The mean EE and DL_{core} values decrease slightly from PCL2.1k to PCL6.0k and then increase sharply from PCL6.0k to PCL12k. Among the three core block lengths, EE and DL_{core} are highest for Py-PNPs prepared using PCL12k block copolymer, a result that can be understood in terms of the PCL12k copolymer containing the largest fraction of the encapsulating hydrophobic PCL component. The small decrease in EE and DL_{core} between the PCL2.1k to PCL6.0k is not well understood, but may be related to a decrease in the prevalence of spherical micelles suggested by the increase in $d_{h,eff}$ between PCL2.1k and PCL6.0k (Figure 3-1). Spherical Py-PNPs possess a larger interfacial area than non-spherical morphologies, which may provide more efficient packing of Py molecules within the PCL cores.

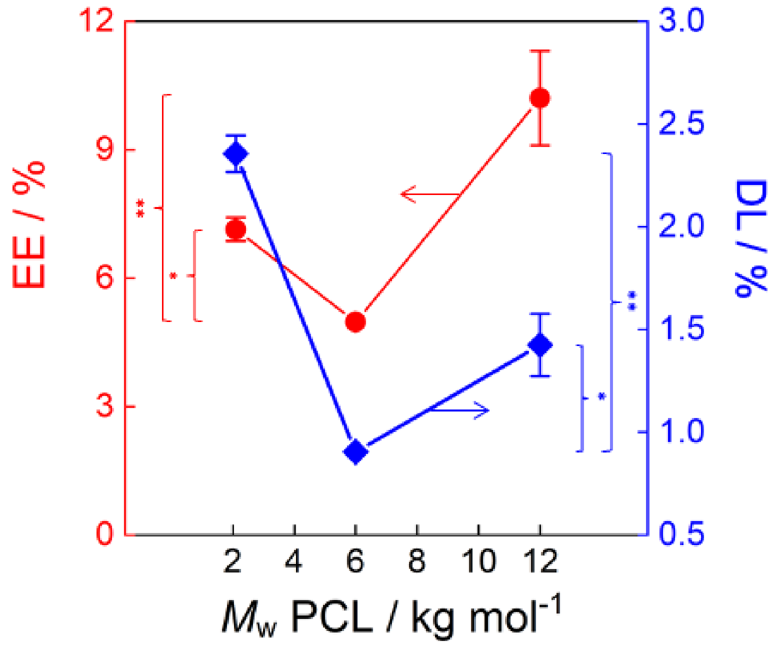

Figure 3-5. Effect of PCL block length on the encapsulation efficiency, EE (red circles) and dye loading, DL_{core} (blue diamonds). All Py-PNPs were prepared with an initial loading ratio of $r_{Py} = 0.1$, and on-chip water content of cwc + 5 wt % and a microfluidic flow rate of Q = 200 μL/min. Error bars represent standard errors from triplicate preparations. Brackets indicate statistical comparisons between EE and DL_{core} of Py-PNPs with different PCL block lengths: * indicates $p < 0.05$ and ** indicates $p < 0.005$.

Next, we compared the steady-state fluorescence properties of encapsulated Py for the three PCL block lengths, specifically the I_1/I_3 peak ratio and the excimer to monomer ratio (I_e/I_m) that have have been used extensively to study microheterogeneous systems.[10,11] Figure 3-6 shows representative normalized emission spectra of Py-PNPs formed from the three copolymers obtained with an excitation wavelength of λ_{ex} = 331 nm. All three spectra show emission from Py monomers (λ_{em} = 373 – 425 nm), and varying intensities of emission from Py excimers (λ_{em} = 480 nm). Interestingly, excimer emission appears to be more prominent for the shortest and longest PCL blocks (PCL2.1k, red spectrum; PCL12k, blue spectrum) and less prominent for the intermediate PCL block (PCL6.0k, black spectrum).

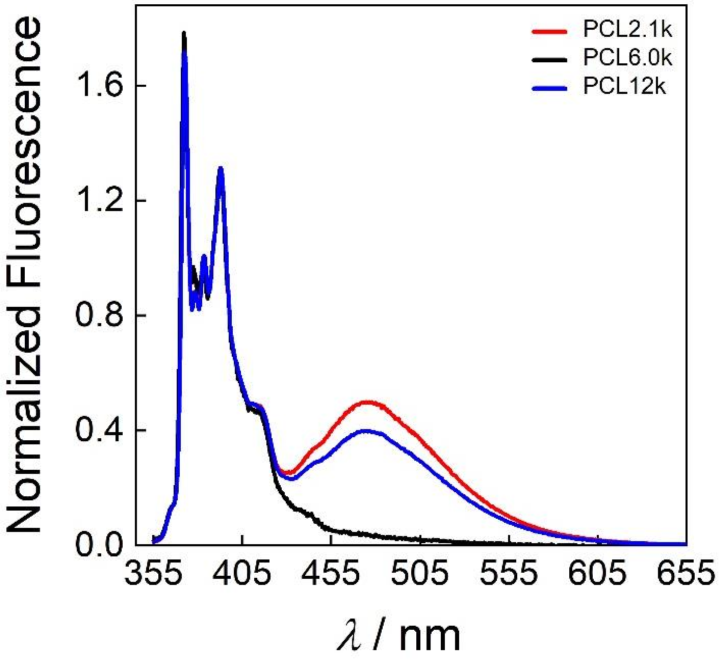

Figure 3-6. Representative normalized (to 383.5 nm) steady-state fluorescence emission spectra (λ_{ex} = 331 nm) of Py-PNPs for three different PCL block lengths. All Py-PNPs were prepared with an initial loading ratio of r_{Py} = 0.1, and on-chip water content of cwc + 5 wt % and a microfluidic flow rate of Q = 200 µL/min.

Using the method described in Chapter 2 (2.7.5), mean ratios I_1/I_3 and I_e/I_m were determined from fluorescence spectra obtained from triplicate preparations of each PCL block length, then plotted as a function of PCL block molecular weight (Figure 3-7). We find a non-monotonic trend in I_e/I_m (Figure 3-7, red squares) that tracks with the trend observed for DL_{core} (Figure 3-5), with both quantities decreasing then increasing as the PCL block length increases. The tracking of I_e/I_m with DL_{core} is reasonable, since higher concentrations of dye within the core (as described by DL_{core}) should lead to shorter mean distances between Py molecules and thus a higher probability of excimer formation. On the other hand, I_1/I_3 (Figure 3-7, blue circles) showed a monotonic increase with increasing PCL block length, possibly suggesting a mean increase in the microenvironment polarity experienced by Py molecules; however, the overall increase is small compared to experimental error and is not found to be statistically significant. For all PCL block lengths investigated, the average I_1/I_3 value was 1.87, compared to 1.87 for Py in water and 0.58 for Py in hexane.[10,12,13]

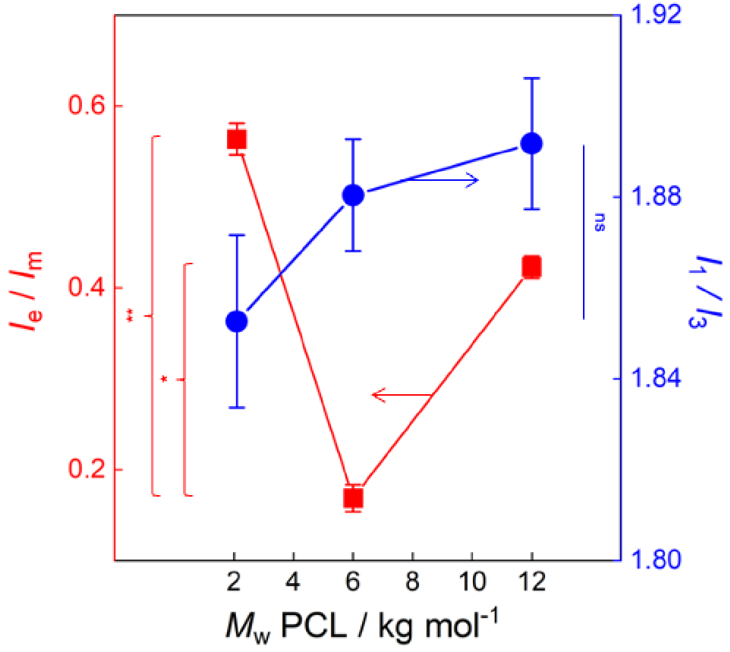

Figure 3-7. Effect of the PCL block length on the Py fluorescence intensity ratios: I_1/I_3 (blue circles) and I_e/I_m (red squares). All Py-PNPs were prepared with an initial loading ratio of $r_{Py} = 0.1$, and on-chip water content of cwc + 5 wt % and a microfluidic flow rate of $Q = 200$ μL/min. Error bars represent standard errors from triplicate preparations. Brackets indicate statistical comparisons between I_1/I_3 and I_e/I_m of Py-PNPs with different PCL block lengths: ns indicates $p > 0.05$, * indicates $p < 0.05$ and ** indicates $p < 0.005$.

3.2.2. Effect of Initial Py:Copolymer Loading Ratio

We next investigated the effect of the initial Py:copolymer loading ratio (w/w), r_{Py} on Py-PNP physicochemical properties ($d_{h,eff}$, DL) and fluorescence properties (I_1/I_3 and I_e/I_m). For these experiments, we used four different dye loading ratios covering almost two orders of magnitude (r_{Py} = 0.01, 0.1, 0.5, and 0.75). For all preparations, a single block copolymer (PCL2.1k) was selected based on the relatively small size of micelles formed from the shorter block length and the relevance to drug delivery applications of PNPs in the size regime of d_h < 200 nm. Other preparation conditions for self-assembly were also kept constant, including microfluidic flow rate (Q = 200 µL/min) and on-chip water content relative to the cwc (cwc + 5.0 wt %). Triplicate preparations were completed for each r_{Py} condition to characterize the resulting Py-PNP properties. In this section, data for the r_{Py} = 0.1 condition is identical to the data for the PCL2.1k condition in the previous section and is included for completeness and to provide comparison with other loading ratios.

The effect of initial Py:copolymer loading ratio on the hydrodynamic size and polydispersity of Py-PNPs is shown in the Figure 3-8. We find a statistically significant decrease in $d_{h,eff}$ as r_{Py} increases (Figure 3-8, red circles). Specifically, hydrodynamic sizes of Py-PNPs decrease from ~150 nm at lower loading ratios (r_{Py} = 0.01 and 0.1) to ~60 nm at higher loading ratios (r_{Py} = 0.5 and 0.75). There is also a corresponding increase in polydispersity (PDI) of prepared Py-PNPs from ~0.2 at the lower loading ratios to ~0.4 at the higher loading ratios (Figure 3-8, black squares). This clearly shows the impact of the initial Py loading ratio on the size and size distributions of Py-PNPs, which can be explained by increased amounts of Py during PNP formation causing more disruption to PCL crystallization, thus lowering the sizes of the resulting aggregates.[14,15] Our group has previously reported a similar decrease in size for PCL-*b*-PEO PNPs with increased paclitaxel loading ratios, which was attributed similarly to the plasticizing role of the added hydrophobic molecules.[14]

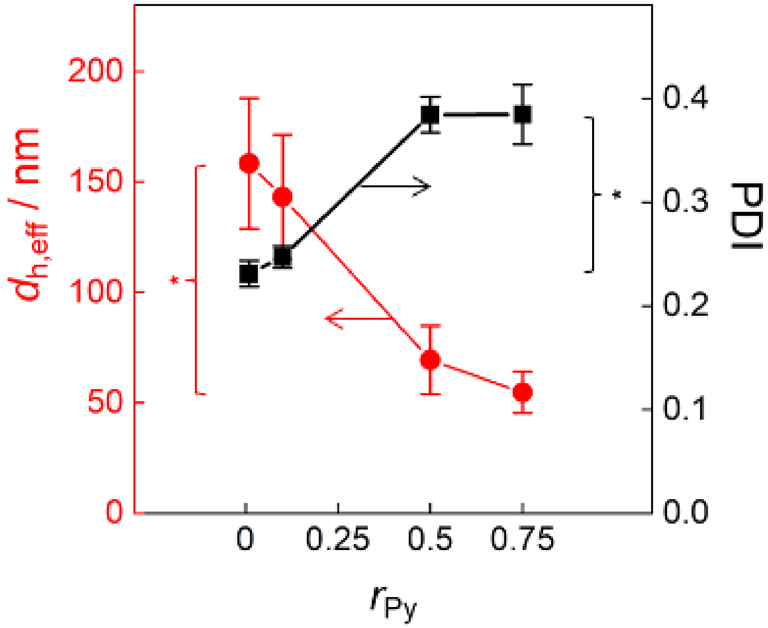

Figure 3-8. Effect of the initial Py:copolymer loading ratio (r_{Py}) on the hydrodynamic diameter (red circles) and polydispersity (black squares) of Py-PNPs determined from cumulant analysis of dynamic light scattering (DLS) measurements. All Py-PNPs were prepared from the PCL2.1k copolymer with an on-chip water content of cwc + 5 wt % and a microfluidic flow rate of Q = 200 µL/min. Error bars represent standard errors from triplicate preparations. Brackets indicate statistical comparisons between $d_{h,eff}$ and PDIs of Py-PNPs with different r_{Py} values: * indicates $p < 0.05$.

The encapsulation efficiency (EE) and dye loading (DL) show interesting trends with increasing r_{Py} (Figure 3-9). EE initially increases between r_{Py} = 0.01 and r_{Py} = 0.1 (Figure 3-9, red circles) which is attributed to a plasticizing effect of Py, which increases the fraction of amorphous PCL regions and thus increases the loading capacity of the core. Then, at higher loading ratios ($r_{Py} > 0.1$), EE drops sharply, which corresponds to a saturation of the core and a corresponding increase in the loss of excess Py as r_{Py} increases the formulation. The saturation of the core with encapsulated Py is also evident in the apparent plateau in DL_{core} (Figure 3-9, blue diamonds), indicating that the amount of Py in the core does not change significantly as more Py is added above $r_{Py} = 0.1$.

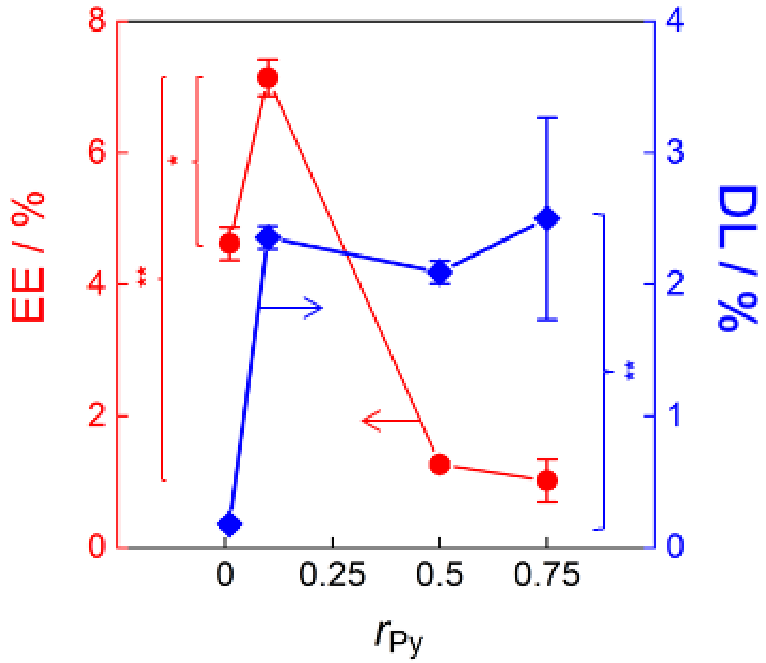

Figure 3-9. Effect of the initial Py:copolymer loading ratio (r_{Py}) on the encapsulation efficiency, EE (red circles) and dye loading, DL_{core} (blue diamonds). All Py-PNPs were prepared from the PCL2.1k copolymer with an on-chip water content of cwc + 5 wt % and a microfluidic flow rate of Q = 200 µL/min. Error bars represent standard errors from triplicate preparations. Brackets indicate statistical comparisons between EE and DL_{core} of Py-PNPs with different r_{Py} values: * indicates $p < 0.05$ and ** indicates $p < 0.005$.

The mean fluorescence intensity ratios I_1/I_3 and I_e/I_m report on the effect of the initial Py:copolymer loading ratio on the Py microenvironment within the Py-PNPs

(Figure 3-10). I_e/I_m (Figure 3-10, red squares) increases between r_{Py} = 0.01 and r_{Py} = 0.50, suggesting an increase in the local Py concentration within the core leading to increased excimer formation. It is interesting that the largest increase in excimer formation is between r_{Py} = 0.1 and r_{Py} = 0.50, even though the dye loading (DL) of the PNPs does not change significantly between the same r_{Py} values (Figure 3-9, blue diamonds). This suggests that Py molecules become more closely packed within the core as r_{Py} increases in this range, even though the amount of encapsulated Py remains unchanged. Then, as r_{Py} continues to increase from r_{Py} = 0.50 to r_{Py} = 0.75, the amount of excimer formation decreases, as evidenced by a decrease in I_e/I_m (Figure 3-10, red squares), suggesting that Py becomes less closely packed within the core, even though the amount of encapsulated Py (DL_{core}) continues to remains relatively constant (Figure 3-9, blue diamonds). This contrast between the behaviours of DL_{core} (Figure 3-9) and I_e/I_m (Figure 3-10) is an interesting result, and underlines the fact that the local environment of Py molecules reported by fluorescence properties cannot be discerned from average physicochemical properties such as DL_{core}.

The polarity of the Py microenvironment, as reported by the mean I_1/I_3 ratios, did not appear to show a strong effect on the initial Py:copolymer loading ratio, as all values (Figure 3-10, blue circles) are similar within experimental error. For all r_{Py} values investigated, the average I_1/I_3 value was 1.87, compared to 1.87 for Py in water and 0.58 for Py in hexane.[10,12,13]

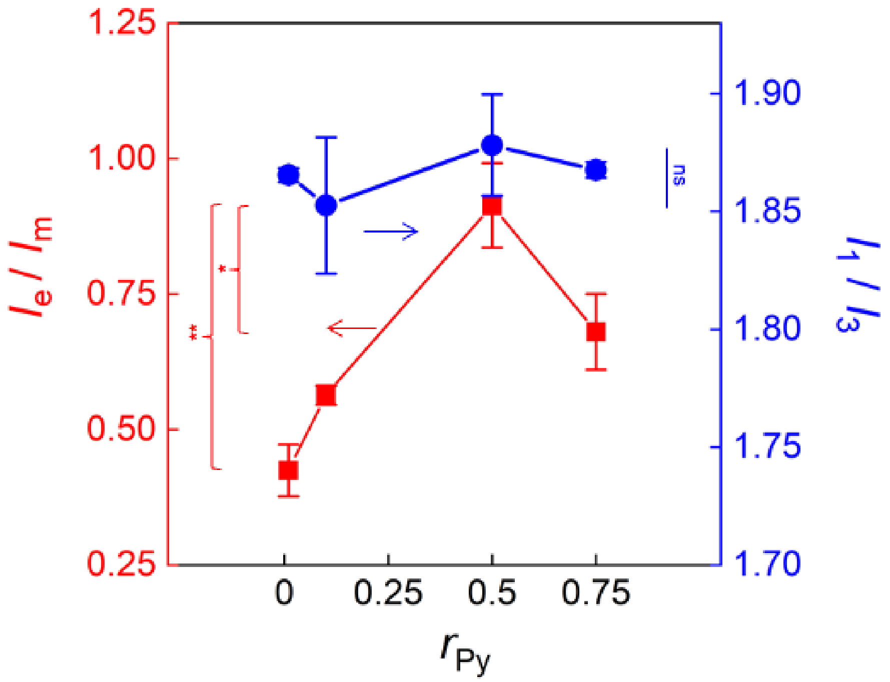

Figure 3-10. Effect of the initial Py:copolymer loading ratio (r_{Py}) on the Py fluorescence intensity ratios: I_1/I_3 (blue circles) and I_e/I_m (red squares). All Py-PNPs were prepared from the PCL2.1k copolymer with an on-chip water content of cwc + 5 wt % and a microfluidic flow rate of Q = 200 µL/min. Error bars represent standard errors from triplicate preparations. Brackets indicate statistical comparisons between I_1/I_3 and I_e/I_m of Py-PNPs with different r_{Py} values: ns indicates $p > 0.05$, * indicates $p < 0.05$ and ** indicates $p < 0.005$.

3.2.3. Effect of On-Chip Water Content

We next investigated the effect of the on-chip water content relative to the cwc (cwc + x) on Py-PNP physicochemical properties ($d_{h,eff}$, DL_{core}) and fluorescence properties (I_1/I_3 and I_e/I_m). For these experiments, we used four different on-chip water contents above the cwc, cwc + x (where x = 2, 5, 20, and 20 wt %). For all preparations, a single block copolymer (PCL2.1k) was selected. Other preparation conditions for self-assembly were also kept constant, including microfluidic flow rate (Q = 200 µL/min) and the initial Py:copolymer loading ratio (r_{Py} = 0.5). Triplicate preparations were completed for each water content to characterize the resulting Py-PNP properties. In this section, data for the cwc + 5 wt % condition is identical to the data for the r_{Py} = 0.5 condition in the previous section and is included for completeness and to provide comparison with other water contents.

The effect of on-chip water content on the hydrodynamic size and polydispersity of Py-PNPs is shown in the Figure 3-11. Mean Py-PNP size increases from $d_{\mathrm{h,eff}}$ = 37 nm to $d_{\mathrm{h,eff}}$ = 70 nm as the water content increases from cwc + 2 wt % to cwc + 5 wt %, then increases to $d_{\mathrm{h,eff}}$ = 85 nm as the water content is further increased to cwc + 10 wt % (Figure 3-11, red circles). Finally, a subsequent increase in the water content to cwc + 20 wt % leads to a drop in Py-PNP size to $d_{\mathrm{h,eff}}$ = 55 nm. This nonmonotonic change in particle size with increasing water content can be explained by a combination of thermodynamic and kinetic factors during Py-PNP formation in the microfluidic channels. As the amount of water above the cwc increases, the thermodynamic driving force for self-assembly increases as the incompatibility between the PCL blocks and the polar solvent environment increases, leading to a tendency to form larger Py-PNPs. However, at the same time, the increase in water content leads to the PCL blocks being less solvated with DMF during Py-PNP formation, leading to slower chain dynamics and a resulting kinetic impediment to micelle growth. As a result of these competing thermodynamic and kinetic factors, Py-PNP sizes are found to increase up to on-chip water contents 10 wt % above the cwc, where the thermodynamic effect is dominant, and then decrease as water contents increase beyond 10 wt % above the cwc, where the effect of slowing chain dynamics become dominant.

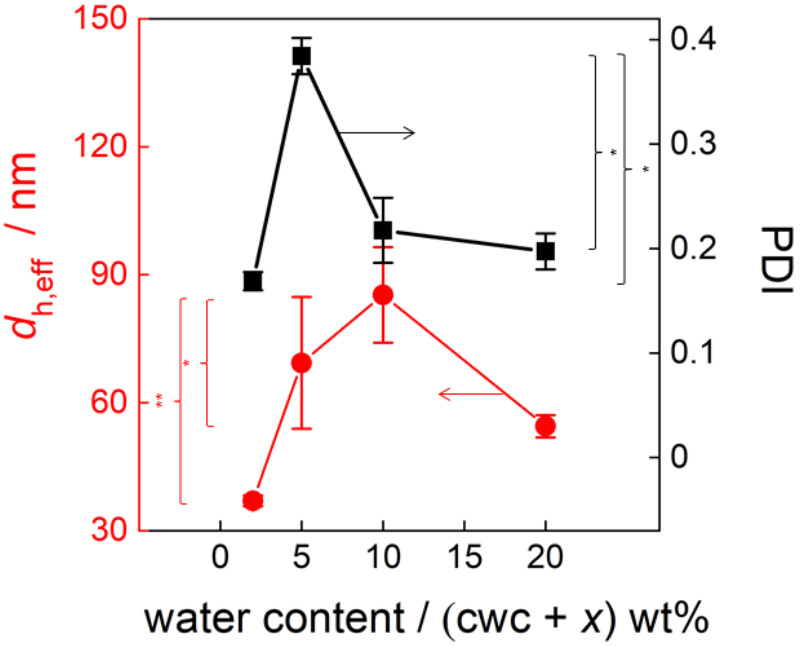

Figure 3-11. Effect of on-chip water content on the hydrodynamic diameter (red circles) and polydispersity (black squares) of Py-PNPs determined from cumulant analysis of dynamic light scattering (DLS) measurements. All Py-PNPs were prepared from the PCL2.1k copolymer with an initial loading ratio of $r_{Py} = 0.5$ and a microfluidic flow rate of $Q = 200$ µL/min. Error bars represent standard errors from triplicate preparations. Brackets indicate statistical comparisons between $d_{h,eff}$ and PDIs of Py-PNPs prepared with different on-chip water contents: * indicates $p < 0.05$ and ** indicates $p < 0.005$.

Comparing PDI values at different on-chip water contents (Figure 3-11, black squares), polydispersities are found to be similar (PDI = ~0.2) for all water contents except cwc + 5 wt % where the Py-PNPs are more polydisperse (PDI = ~0.4). The imposition of kinetic constraints on micelle growth will increase polydispersities compared to a highly dynamic system, and yet the effect of these constraints on the final PDI will depend on the driving force for micelle growth and the resulting mean particle size. Therefore, in the current series, it appears that the interplay of micelle growth and kinetic constraints at cwc + 5 wt % leads to elevated PDIs compared to the other investigated water contents.

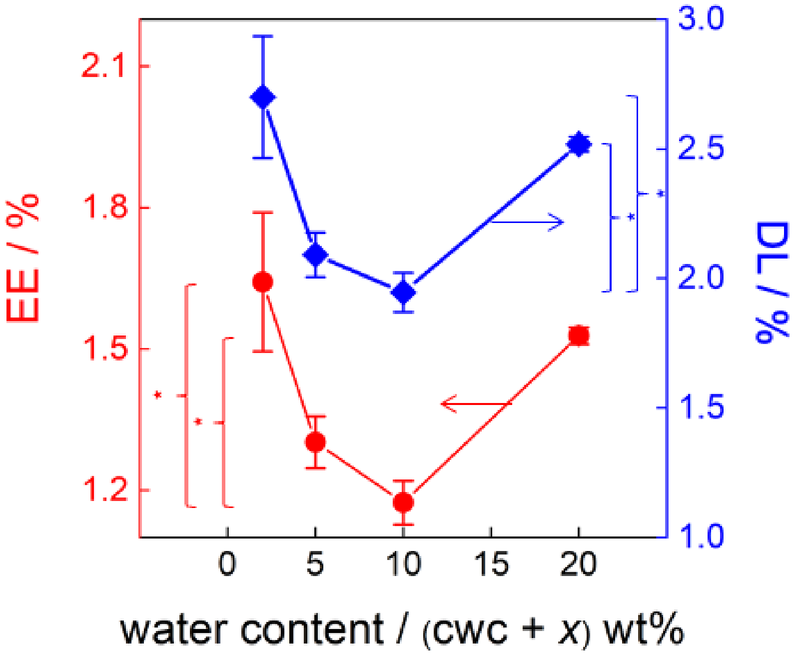

Figure 3-12. Effect of on-chip water content on the encapsulation efficiency, EE (red circles) and dye loading, DL_{core} (blue diamonds). All Py-PNPs were prepared from the PCL2.1k copolymer with an initial loading ratio of r_{Py} = 0.5 and a microfluidic flow rate of Q = 200 µL/min. Error bars represent standard errors from triplicate preparations. Brackets indicate statistical comparisons between EE and DL_{core} values of Py-PNPs prepared with different on-chip water contents: * indicates $p < 0.05$.

Considering the effect of on-chip water content on the encapsulation efficiency (EE) and dye loading of the PCL core (DL_{core}) (Figure 3-12), these parameters follow an interesting non-monotonic trend that appears counterintuitive in the context of the thermodynamics of partitioning Py into the core. As water content increases, we expect the driving force for Py entering the core to increase, and yet EE (Figure 3-12, red circules) and DL_{core} (Figure 3-12, blue diamonds) both decrease as the on-chip water content increases from cwc + 2.0 wt % to cwc + 10.0

wt %. This may be a kinetic effect, associated with a decrease in PCL chain dynamics at higher water content, leading to restricted penetration of Py molecules into the PCL cores. In addition, the mean Py-PNP size increases in the same range of water contents (Figure 3-11), resulting in lower interfacial area which may further restrict access of Py molecules to the core. Finally, EE (Figure 3-12, red circules) and DL_{core} (Figure 3-12, blue diamonds) show an increase as the on-chip water content is further increased to cwc + 20 wt %; this increase is attributed to a combination of the increased driving force for partitioning Py into the core and also increased interfacial access due to the associated decrease in mean Py-PNP size (Figure 3-11).

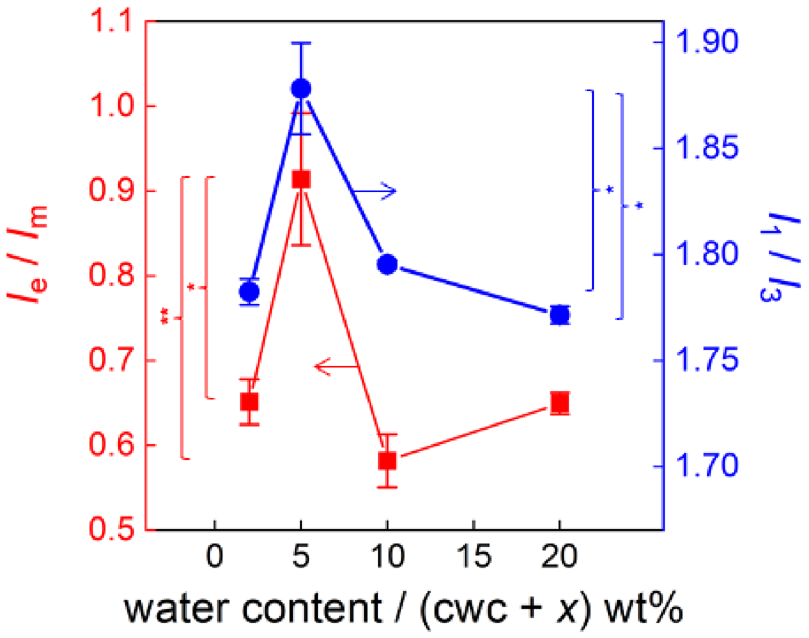

Figure 3-13. Effect of on-chip water content on the Py fluorescence intensity ratios: I_1/I_3 (blue circles) and I_e/I_m (red squares). All Py-PNPs were prepared from the PCL2.1k copolymer with an initial loading ratio of $r_{Py} = 0.5$ and a microfluidic flow rate of $Q =$ 200 μL/min. Error bars represent standard errors from triplicate preparations. Brackets indicate statistical comparisons between I_1/I_3 and I_e/I_m of Py-PNPs prepared with different on-chip water contents: * indicates $p < 0.05$ and ** indicates $p < 0.005$.

The mean fluorescence intensity ratios I_1/I_3 and I_e/I_m describe the effect of the on-chip water content on the Py microenvironment within the Py-PNPs (Figure 3-13). I_e/I_m (Figure 3-13, red squares), reporting on the mean distance between Py molecules within the core, shows a sharp increase between cwc + 2 wt % and cwc + 5 wt %, followed by a sharp decrease between cwc + 5 wt % and cwc + 10 wt %. Interestingly, I_1/I_3 (Figure 3-13, blue circles), reporting on the polarity of the Py microenvironment and thus the proximity of Py molecules to the core-corona interface, shows a very similar trend to I_e/I_m, with statistically significant variation in values between 1.77 and 1.87 with changing water content. It is important to note that neither fluorescence ratio track with the associated trend in DL_{core} (Figure 3-12), which steadily decreases in the same range of water contents.

In order to validate the method of excimer subtraction used to obtain I_1/I_3 ratios, we applied an alternative method (described in section 2.7.5.) to determine I_1/I_3 ratios for certain conditions. The I_1/I_3 mean values and associated errors using both methods were as follows: 1. For the cwc + 2.0 wt% condition: 1.78 ± 0.01 (original method); 1.78 ± 0.01 (alternative method); 2. For the cwc + 5.0 wt% condition: 1.88 ± 0.01 (original method); 1.89 ± 0.01 (alternative method). The lack of any significant difference between values obtained by these two methods supports the validity of the original method which was applied to the majority of the data.

This provides another example of the difference between the local environment of Py molecules and average Py-PNP properties such as the concentration of encapsulated Py molecules in the core (DL_{core}). We believe that the observed trend in I_1/I_3 can be explained by the competition between an increase in the thermodynamic driving force for encapsulated Py molecules to passivate the core-corona interface with increasing water content, and a decrease in the Py diffusion rate at higher water contents as DMF is forced from the core leading to a decrease in the PCL viscosity. Py molecules distributed throughout the core following encapsulation will have a tendency to diffuse to the interface, driven by the interfacial tension, and both the thermodynamic driving force and the diffusion rate will depend strongly on the water content. Based on the interplay of these competing effects, a maximum in Py localization at the interface (and associated I_1/I_3 value) is reached at an on-chip water content of cwc + 5 wt %, with a further increase in water content leading to a dominant restriction in Py diffusion and an associated drop in interface localization. The associated trend in excimer formation (I_e/I_m), which tracks very closely with that of interface localization (I_1/I_3), is simply explained by shorter mean distances between Py molecules as they become more locally concentrated in the interfacial region of the core.

3.2.4. Effect of Microfluidic Flow Rate

The previous sections demonstrated that chemical variables, including PCL block length, initial Py:copolymer loading ratio, and on-chip water content, can be used to control physicochemical properties of drug delivery PNPs prepared using microfluidics, as well as using conventional manufacturing methods.[14,16] In this section, we demonstrate the effect of microfluidic flow rate on Py-PNP physicochemical properties ($d_{h,eff}$, DL, and $\chi_{PCL,core}$) and fluorescence properties (I_1/I_3 and I_e/I_m). In these experiments, we use the PCL2.1k copolymer and the initial Py:copolymer loading ratio (r_{Py} = 0.50) and on-chip water content (cwc + 5.0 wt %) are held constant. The effects of on-chip flow rate on the size, morphology, internal crystallinity, and drug loading of

PNPs formed in segmented gas-liquid microfluidic reactors have been described in previous publications from our group.[2,6,14,17–21]

The effect of microfluidic flow rate, Q, on the hydrodynamic size and polydispersity of Py-PNPs is shown in the Figure 3-14. We find a significant increase from $d_{\mathrm{h,eff}}$ = 55 nm to $d_{\mathrm{h,eff}}$ = 167 nm as flow rate increases from Q = 50 µL/min to Q = 100 µL/min, followed by a sharp decrease to $d_{\mathrm{h,eff}}$ = 69 nm as flow rate increases to Q = 200 µL/min and a smaller decrease to $d_{\mathrm{h,eff}}$ = 67 nm as flow rate further increases to Q = 400 µL/min (Figure 3-14, red circles). Nonmonotonic changes in particle size with increasing microfluidic flow rate have been observed previously in our group and are attributed to the interplay of competing mechanisms as the maximum shear rate in the channels increases.[2,14,16,19] The following PNP shear processing mechanisms are operative within the channels following mixing with water and Py-PNP formation: (1) shear-induced particle coalescence,[18,19] (2) shear-induced particle breakup,[18,19] and (3) shear-induced core crystallisation.[2,20] The initial increase in $d_{\mathrm{h,eff}}$ is attributed to a combination of mechanisms (1) and (3), both of which serve to increase the mean particle size. As mean particle sizes increase, they become more susceptible to mechanism (2), explaining the decrease in $d_{\mathrm{h,eff}}$ at higher flow rates. We note that the initial on-set of shear-induced particle breakup (indicated by decrease in size from $d_{\mathrm{h,eff}}$ = 167 nm to $d_{\mathrm{h,eff}}$ = 69 nm between Q = 100 µL/min and Q = 200 µL/min) is accompanied by a sharp increase in particle polydispersity from PDI = 0.24 to PDI = 0.38 (Figure 3-14, black squares); further increase in flow rate to Q = 400 µL/min results in a sharp drop in PDI down to 0.27 although the mean size decreases by only a few nanometers (from $d_{\mathrm{h,eff}}$ = 69 nm to $d_{\mathrm{h,eff}}$ = 67 nm). Further insights into the role of flow-tunable shear forces on mean particle sizes and polydispersities requires consideration of Py-PNP morphologies at the various flow rates from TEM data.

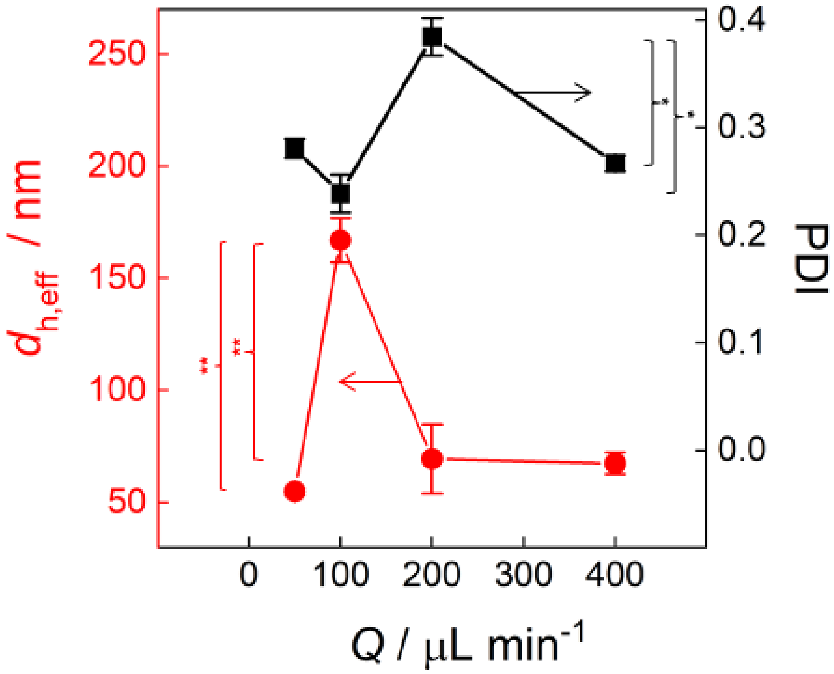

Figure 3-14. Effect of the microfluidic flow rate (*Q*) on the hydrodynamic diameter (red circles) and polydispersity (black squares) of Py-PNPs determined from cumulant analysis of dynamic light scattering (DLS) measurements. All Py-PNPs were prepared from the PCL2.1k copolymer with an initial Py:copolymer loading ratio of $r_{Py} = 0.5$ and an on-chip water content of cwc + 5 wt %. Error bars represent standard errors from triplicate preparations. Brackets indicate statistical comparisons between $d_{h,eff}$ and PDIs of Py-PNPs prepared at different flow rates: * indicates $p < 0.05$.

Representative TEM images for Py-PNPs obtained at different microfluidic flow rates are shown in the Figure 3-15. The images provide further insights into the effects of shear on the Py-PNPs indicated by trends in $d_{h,eff}$ and PDI (Figure 3-14). At the lowest investigated flow rate (Figure 3-15A, Q = 50 µL/min), the particle population consists of a mixture of spheres and filaments. A greater number of longer filaments is present after an increase in flow rate to Q = 100 µL/min, explaining the corresponding large increase in $d_{h,eff}$ between Q = 50 μL/min and Q = 100 μL/min (Figure 3-14), likely due to a combination of shear-induced particle coalescence and shear-induced crystallization.[16,19] Further increasing the flow rate to Q = 200 μL/min appears to result in the shear-induced breakup of the long extended filaments (Figure 3-15B, Q = 100 μL/min) into a polydisperse mixture of shorter cylindrical and irregularly shaped lamellar aggregates and small spheres (Figure 3-15C, Q = 200 μL/min), consistent with the corresponding sharp decrease in $d_{h,eff}$ and sharp increase in PDI determined from DLS data (Figure 3-14). Finally, the increase in flow rate to Q = 400 μL/min appears to result in a homogenization of the Py-PNP population to predominantly spheres (Figure 3-15D, Q = 400 μL/min), likely due to a combination of shear-induced breakup of short cylinders and lamellae and shear-induced coalescence of smaller spheres. This last morphological transition is consistent with the corresponding small decrease in $d_{h,eff}$ and sharp drop in PDI determined from DLS data (Figure 3-14). Taken together, the TEM and DLS results in Figure 3-14 and 3-15 demonstrate that flow rate variation in the two-phase microfluidic reactor provides an effective tool to modulate important structural features of drug delivery PNPs relevant to biological transport, targeting and cellular uptake.[22–24]

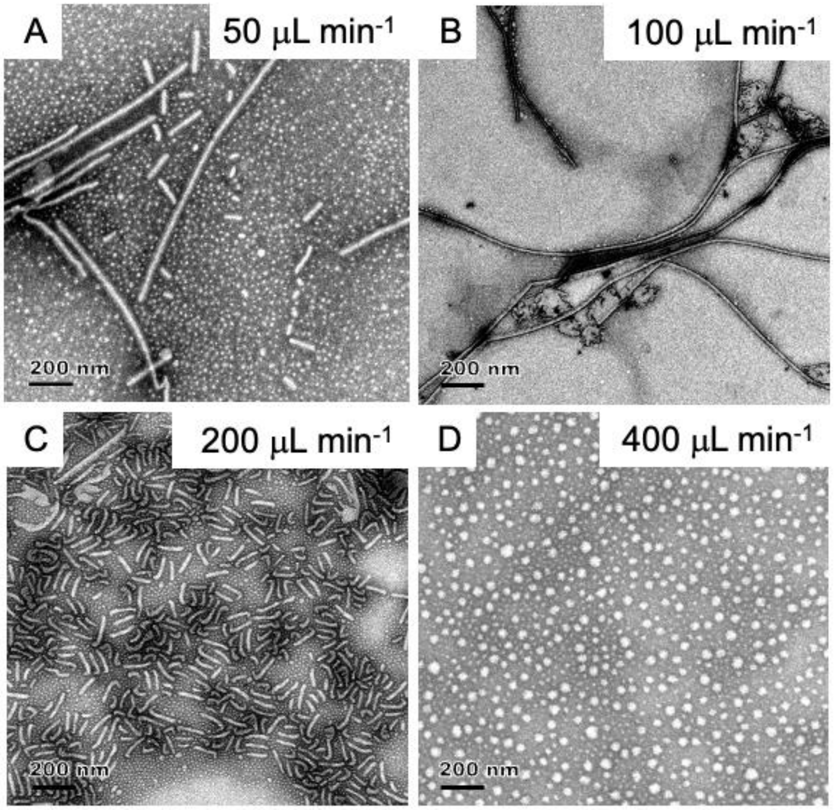

Figure 3-15. Representative TEM images showing the effect of microfluidic flow rate, Q, on the Py-PNP morphologies. All Py-PNPs were prepared from the PCL2.1k copolymer with an initial Py:copolymer loading ratio of $r_{Py} = 0.5$ and an on-chip water content of cwc + 5 wt %. All scale bars are 200 nm.

The encapsulation efficiency (EE) and dye loading (DL_{core}) values with changing flow rate Q are shown in Figure 3-16. Both EE (Figure 3-16, red circles) and DL_{core} (Figure 3-16, blue diamonds) show a similar increasing then decreasing trend to $d_{h,eff}$ (Figure 3-14), although while $d_{h,eff}$ reaches a maximum at Q = 100 μL/min, the maximum in EE and DL_{core} comes at Q = 200 μL/min. Specifically, DL_{core} shows similar values of 0.42 % and 0.41 % at Q = 50 μL/min and Q = 100 μL/min, respectively, then increases to 0.64 % at Q = 200 μL/min before decreasing to 0.48 % at Q = 400 μL/min. The maximum in DL_{core} at Q = 200 μL/min cannot be easily explained in terms of particle size, since this flow rate does not coincide with the maximum in $d_{h,eff}$ observed by DLS (Figure 3-14). We will show that the PCL crystallinities are similar for Q = 100, 200 and 400 μL/min (*vide infra*) and so the increase in DL_{core} is not explained by an increase in amorphous material within the core. Considering the TEM data in Figure 3-15C, we note that the polydisperse short cylinders and lamellae that are present at Q = 200 μL/min are not present at any other flow rate; we speculate that the corresponding maximum in DL_{core} may be due to preferential encapsulation of Py within these Py-PNP morphologies.

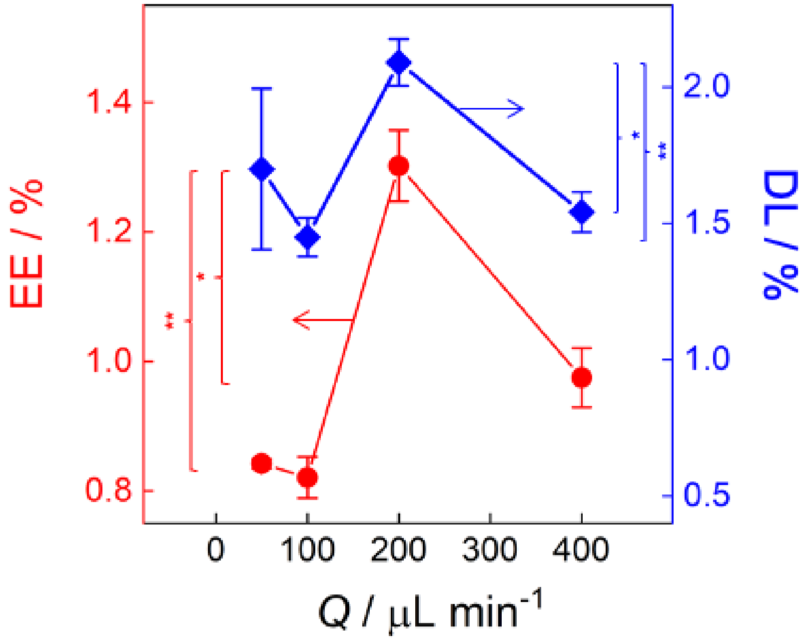

Figure 3-16. Effect of the microfluidic flow rate (Q) on the encapsulation efficiency, EE (red circles) and dye loading, DL_{core} (blue diamonds). All Py-PNPs were prepared from the PCL2.1k copolymer with an initial Py:copolymer loading ratio of $r_{Py} = 0.5$ and an on-chip water content of cwc + 5 wt %. Error bars represent standard errors from triplicate preparations. Brackets indicate statistical comparisons between EE and DL_{core} values of Py-PNPs prepared at different flow rates: * indicates $p < 0.05$ and ** indicates $p < 0.005$.

Figure 3-17 shows the effect of microfluidic flow rate on the core crystallinity of Py-PNPs. Our group has previously shown that PCL core crystallinity increases with increasing flow rate for PCL-*b*-PEO PNPs formed in a two-phase microfluidic reactor, due to shear-induced crystallization.[16,17,19] We find a similar effect in the current Py-PNPs, with an increase in $\chi_{\mathrm{PCL,core}}$ from 25 % to 38 % as the flow rate increases from Q = 50 μL/min to Q = 100 μL/min, followed by a more gradual increase at higher flow rates, with in $\chi_{\mathrm{PCL,core}}$ reaching 42 % at Q = 400 μL/min.

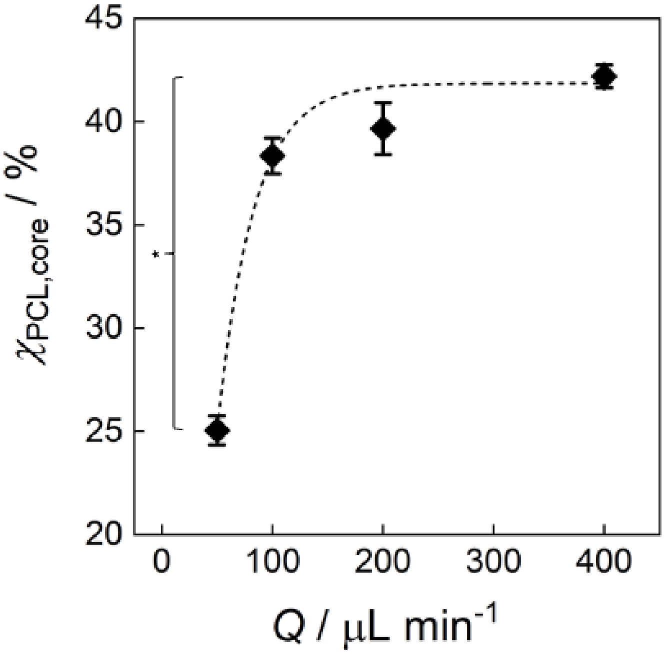

Figure 3-17. Effect of the microfluidic flow rate (Q) on the mass percentage of crystalline PCL relative to the mass of the core, $\chi_{\mathrm{PCL,core}}$. All Py-PNPs were prepared from the PCL2.1k copolymer with an initial Py:copolymer loading ratio of r_{Py} = 0.5 and an on-chip water content of cwc + 5 wt %. Error bars represent standard errors from triplicate preparations. The brackets indicate statistical comparison between $\chi_{\mathrm{PCL,core}}$ values of Py-PNPs prepared at different flow rates: * indicates $p < 0.05$.

The mean fluorescence intensity ratios I_1/I_3 and I_e/I_m report on the effect of microfluidic flow rate on the Py microenvironment within the Py-PNPs (Figure 3-

18). I_e/I_m (Figure 3-18, red squares) is found to increase as flow rate increases up to Q = 200 μL/min and then decreases between Q = 200 μL/min and Q = 400 μL/min. This trend in I_e/I_m with flow rate is found to closely track with the trends in EE and $\mathrm{DL_{core}}$ in Figure 3-16. This suggests that excimer formation increases with an increase in the amount of encapsulated Py within the PCL cores, leading to a corresponding decrease in the mean distance between Py molecules. Interestingly, we find that the trend in I_1/I_3 with flow rate (Figure 3-18, blue circles), which reports on the polarity of the local Py microenvironment, also tracks closely with the trends in EE and $\mathrm{DL_{core}}$ (Figure 3-13). This suggests that as the amount of encapsulated Py in the PCL cores increases, Py molecules experience a microenvironment of higher polarity. A possible explanation is that as the number of Py molecules in the core increases, localization of Py at the relatively polar core-corona interface becomes more favorable. We note that the maximum I_1/I_3 value of 1.87 (Q = 200 μL/min), which corresponds to a maximum $\mathrm{DL_{core}}$ value of 0.64 % for the flow rate series, is equal to the I_1/I_3 value associated with Py-saturated cores ($\mathrm{DL_{core}}$ = 0.76 %, Figure 3-9) for the series of different r_{Py} values (Figure 3-10). This further supports a correlation between relatively high $\mathrm{DL_{core}}$ values and relatively high polarity of the Py microenvironment.

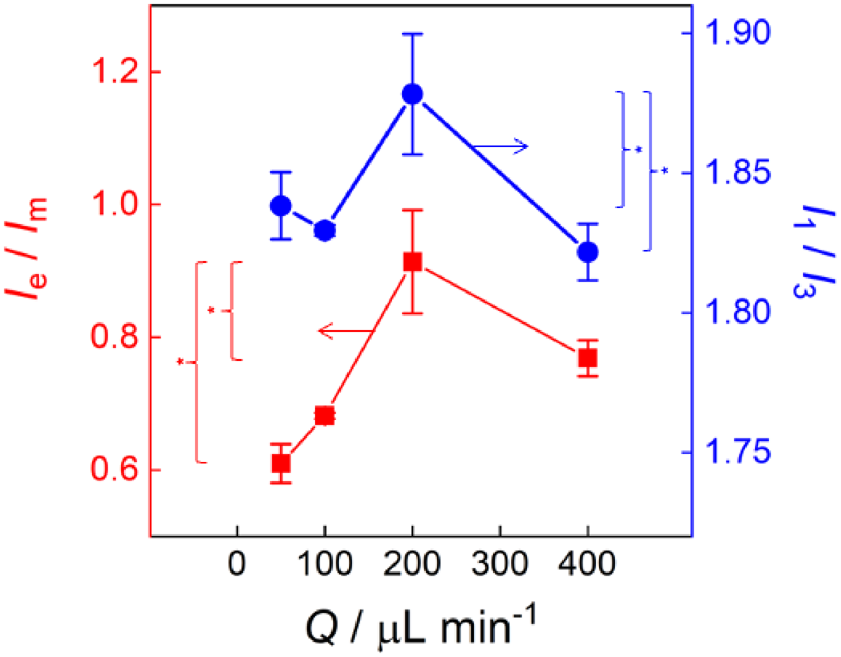

Figure 3-18. Effect of the microfluidic flow rate (Q) on the Py fluorescence intensity ratios: I_1/I_3 (blue circles) and I_e/I_m (red squares). All Py-PNPs were prepared from the PCL2.1k copolymer with an initial Py:copolymer loading ratio of r_{Py} = 0.5 and an on-chip water content of cwc + 5 wt %. Error bars represent standard errors from triplicate preparations. Brackets indicate statistical comparisons between I_1/I_3 and I_e/I_m of Py-PNPs prepared at different flow rates: * indicates $p < 0.05$.

3.2.5. Summary and Discussion of Effects of Nanoparticle Preparation Variables on Physicochemical and Fluorescence Properties of Py-PNPs

Table 3-1. Reported mean values and standard errors of measured physiochemical properties of Py-PNPs for various preparation conditions.[a]

Copolymer	r_{Py}	Q /µL min^{-1}	cwc + x / wt%	$d_{h,eff}$ / nm	PDI	EE / %	DL$_{core}$ / %	$\chi_{PCL,core}$ / %
PCL2.1k[b]	0.1	200	5	140 ± 30	0.25 ± 0.01	7.1 ± 0.3	2.4 ± 0.1	45 ± 4
PCL6k	0.1	200	5	630 ± 60	0.30 ± 0.02	5.00 ± 0.02	0.90 ± 0.01	44 ± 1
PCL12k	0.1	200	5	480 ± 12	0.28 ± 0.04	10 ± 1	1.4 ± 0.1	41 ± 1
PCL2.1k	0.01	200	5	160 ± 30	0.23 ± 0.01	5 ± 1	0.20 ± 0.03	--
PCL2.1k[b]	0.1	200	5	140 ± 30	0.25 ± 0.01	7.1 ± 0.3	2.4 ± 0.1	45 ± 4
PCL2.1k[c]	0.5	200	5	70 ± 15	0.38 ± 0.02	1.30 ± 0.05	2.1 ± 0.1	40 ± 1
PCL2.1k	0.75	200	5	55 ± 10	0.38 ± 0.03	1.0 ± 0.3	2.5 ± 0.8	--
PCL 2.1k	0.5	200	2	37 ± 1	0.20 ± 0.02	1.6 ± 0.1	2.7 ± 0.2	--
PCL2.1k[c]	0.5	200	5	70 ± 15	0.38 ± 0.02	1.30 ± 0.05	2.1 ± 0.1	40 ± 1
PCL2.1k	0.5	200	10	85 ± 11	0.22 ± 0.03	1.20 ± 0.05	2.0 ± 0.1	
PCL2.1k	0.5	200	20	55 ± 3	0.17 ± 0.01	1.50 ± 0.02	2.50 ± 0.03	
PCL 2.1k	0.5	50	5	55 ± 2	0.28 ± 0.01	1.00 ± 0.03	1.7 ± 0.3	25 ± 1
PCL2.1k	0.5	100	5	170 ± 10	0.24 ± 0.02	0.90 ± 0.04	1.40 ± 0.07	38 ± 1
PCL2.1k[c]	0.5	200	5	70 ± 15	0.38 ± 0.02	1.30 ± 0.05	2.1 ± 0.1	40 ± 1
PCL2.1k	0.5	400	5	67 ± 5	0.27 ± 0.01	0.90 ± 0.04	1.50 ± 0.07	42 ± 1

a. Effect of PCL block length (blue cells); effect of r_{Py} (yellow cells); effect of on-chip water content (green cells); effect of microfluidic flow rate (orange cells).

b. Identical data sets, included in two different series for completeness.

c. Identical data sets, included in three different series for completeness.

Table 3-2. Reported mean values and standard errors of measured steady-state fluorescence properties of Py-PNPs for various preparation conditions.[a]

Copolymer	r_{Py}	Q / µL min^{-1}	cwc + x / wt%	I_1/I_3	I_e/I_m
PCL2.1k[b]	0.1	200	5	1.85 ± 0.02	0.56 ± 0.02
PCL6k	0.1	200	5	1.88 ± 0.01	0.17 ± 0.01
PCL12k	0.1	200	5	1.89 ± 0.01	0.42 ± 0.01
PCL2.1k	0.01	200	5	1.86 ± 0.01	0.43 ± 0.05
PCL2.1k[b]	0.1	200	5	1.85 ± 0.03	0.56 ± 0.02
PCL2.1k[c]	0.5	200	5	1.87 ± 0.02	0.91 ± 0.08
PCL2.1k	0.75	200	5	1.87 ± 0.01	0.68 ± 0.07
PCL 2.1k	0.5	200	2	1.78 ± 0.01	0.65 ± 0.02
PCL2.1k[c]	0.5	200	5	1.87 ± 0.02	0.91 ± 0.08
PCL2.1k	0.5	200	10	1.79 ± 0.01	0.58 ± 0.03
PCL2.1k	0.5	200	20	1.77 ± 0.01	0.65 ± 0.01
PCL 2.1k	0.5	50	5	1.83 ± 0.01	0.61 ± 0.03
PCL2.1k	0.5	100	5	1.83 ± 0.01	0.68 ± 0.01
PCL2.1k[c]	0.5	200	5	1.87 ± 0.02	0.91 ± 0.08
PCL2.1k	0.5	400	5	1.82 ± 0.01	0.77 ± 0.02

d. Effect of PCL block length (blue cells); effect of r_{Py} (yellow cells); effect of on-chip water content (green cells); effect of microfluidic flow rate (orange cells).
e. Identical data sets, included in two different series for completeness.
f. Identical data sets, included in three different series for completeness.

These results show that experimental variables routinely used to control the structure and loading of drug-delivery PNPs can have a significant effect, not only on the physicochemical properties of PNPs that are typically and routinely characterized— particle size, polydispersity and drug loading— but also on the molecular-level microenvironment of the encapsulated hydrophobic molecules. The significant differences in pyrene fluorescence ratios reported here indicate important differences in the spatial distribution of encapsulated molecules within the core. Specifically, differences in the I_e/I_m ratio indicate differences in the mean distance between encapsulated molecules within the core, while differences in the I_1/I_3 ratio indicate differences in the microenvironment polarity, which can be interpreted in terms of the relative distance of encapsulated molecules from the more polar (PCL-PEG) core-corona interface and less polar (PCL) core center. What we have shown, therefore, is that the experimental variables used in the manufacturing of drug delivery PNP formulations can have a significant impact on the distribution of encapsulated molecules within the core, both in terms of association/aggregation between molecules and how close to the interface they reside. These factors can have a significant impact on the performance of PNP delivery vehicles in terms of their release profiles, and yet this information is generally invisible to common PNP characterization tools, including DLS, HPLC, and XRD.

An interesting observation of this study is that for experimental variables that do not affect the molecular interactions of Py molecules during self-assembly, namely the PCL block length and the flow rate, the fluorescence ratios I_e/I_m and I_1/I_3 were either unaffected by the experimental variable or else tracked closely with the concentration of encapsulated Py, DL_{core}. These experimental variables appeared to affect the spatial distribution of Py molecules primarily by changing the number of Py molecules within the PNP core. For example, changes in the PCL block length had no significant effect on I_1/I_3 (Figure 3-7) and corresponding changes in I_e/I_m (Figure 3-7) tracked closely with changes in DL_{core} (Figure 3-5). In addition, changes in the microfluidic flow rate led to significant changes in both I_1/I_3 and I_e/I_m (Figure 3-18), which both tracked closely with corresponding changes in $\mathrm{DL_{core}}$ (Figure 3-16). On the other hand, for experimental variables that affect the molecular interactions of Py molecules during self-assembly, namely the initial Py:copolymer loading ratio (r_{Py}) and the on-chip water content, the fluorescence ratios I_e/I_m and I_1/I_3 showed significant variations that were independent of variations in $\mathrm{DL_{core}}$. These experimental variables appeared to affect the spatial distribution of Py molecules through mechanisms that were independent of the number of Py molecules within the PNP core. For example, changes in r_{Py} had no significant effect on I_1/I_3 (Figure 3-10), but significant changes in I_e/I_m (Figure 3-10) occurred over a range of r_{Py} in which $\mathrm{DL_{core}}$ remained relatively constant (Figure 3-9). In addition, changes in the on-chip water content led to significant changes in both I_1/I_3 and I_e/I_m with similar trends (Figure 3-13), which did not track with the corresponding trend of $\mathrm{DL_{core}}$ (3-12). We believe these are important observations, since they indicate that for some experimental variables of PNP manufacturing, information about changes in the spatial distribution of encapsulated drug molecules may be inferred from changes in the drug loading. On the other hand, for other experimental variables, in particular chemical variables that influence the molecular interactions of the drug during PNP formation, information about changes in the spatial distribution of encapsulated drug molecules cannot be inferred from changes in the drug loading, and therefore must be determined by further testing— including *in vitro* drug release, cell culture studies, or *in vivo* experiments.

These experiments also provide a yardstick on the range of differences in the microenvironment of encapsulated drug molecules that are present (and can be measured) in the cores of drug delivery nanoparticles over a wide range of chemical and processing formulation variables. Our experiments spanned an extensive range of variables, albeit for a single copolymer type (PCL-*b*-PEO), covering the entire range of hydrophobic block lengths, drug loading ratios, and water contents that are normally applied in the literature, along with covering the entire range of flow rates applied by our group for PNP manufacturing on two-phase microfluidic reactors. For our complete set of experiments, summarized in Table 3.1 (measured Py-PNP physicochemical properties) and Table 3.2 (measured Py-PNP fluorescence properties), we observed variability in I_e/I_m between 0.17 ± 0.01 and 0.91 ± 0.08, or about a factor of 5 difference between the smallest and largest measured values. This indicates a large variability in the relative proximity of encapsulated molecules within the core over the wide range of investigated conditions. On the other hand, we observed variability in I_1/I_3 between 1.77 ± 0.01 and 1.89 ± 0.01, which is less than a 10 % difference between the smallest and largest measured values. This indicates only a small variability in the microenvironment polarity within the core over the wide range of investigated conditions; this is perhaps not too surprising, since PCL is a relatively polar hydrophobic polymer, leading to small polarity differences between the center of the core and the interface. However, despite the small dynamic range in I_1/I_3 in the current system, we were nonetheless able to measure statistically significant differences over the range of conditions investigated, suggesting that the distance from the interface of encapsulated molecules varied significantly for different formulation conditions, and also that those differences can be measured using steady-state fluorescence of a Py probe molecule.

Finally, these experiments suggest some practical formulation principles that should be useful in optimizing drug release profiles. The first of these is the apparent importance of initial drug loading ratio on the association state of drug molecules within the core, irrespective of similarities in the final drug loading. For example, as illustrated in Figure 3-19, we found that a factor of 5 increase in the initial Py loading ratio from $r_{\mathrm{Py}} = 0.1$ to $r_{\mathrm{Py}} = 0.5$ did not change the dye loading in the core $\mathrm{DL}_{\mathrm{core}}$ (Table 3-1), but nonetheless resulted in almost a doubling of excimer emission (Table 3-2), suggesting closer association of the same number of Py molecules in the core. Association or aggregation of drug molecules in the PNP core provide a means of slowing drug diffusion rates; therefore, our results suggest that the initial drug loading ratio could be an experimental handle for improving drug release profiles for some therapeutic applications. Of course, the r_{Py} values and association states described in Figure 3-19 refer to our specific experiments on Py loading, and different molecules including drugs are expected to have different tendencies to associate in a manner that will also depend on the water content and other chemical and processing variables. Therefore, the general principle revealed by these results should be characterized for specifics drugs and formulation conditions. Although fluorescence experiments are not possible for non-fluorescent drug cargo, experiments on *in vitro* release rates vs. initial drug loading may shed interesting light on this effect.

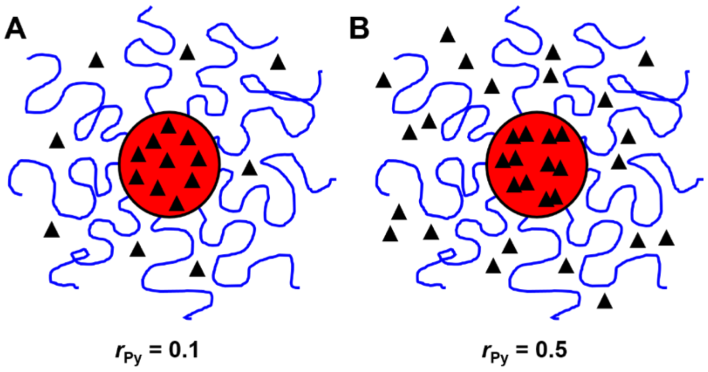

Figure 3-19. Schematic based on I_e/I_m values showing increased association of Py (black triangles) in the PCL core with increase in the initial Py:copolymer loading ratio from $r_{Py} = 0.1$ (A) to $r_{Py} = 0.5$ (B).

The second important formulation principle suggested by our results is the importance of water content during PNP formation on the localization of drug molecules at the core-corona interface. For example, as illustrated in Figure 3-20, we found that increasing the on-chip water content from cwc + 2 wt % to cwc + 5 wt % resulted in a significant drop in the dye loading in the core DL (Table 3-1) while at the same time the encapsulated molecules became significantly more localized at the interface, as indicated by a sharp increase in I_1/I_3 (Table 3-2). Localization of drug molecules at the core-corona interface, rather than a more even distribution of drug molecules throughout the core, may cause burst release and diffusion-driven release profiles that are unfavourable for drug delivery applications. Therefore, our results suggest that the water content may be an important experimental handle for minimizing interfacial localization and burst release. Again, the water content values and associated interfacial localization described in Figure 3-20 refer to our specific experiments on Py loading, and different molecules including drugs are expected to have different tendencies for interfacial localization along with different diffusion kinetics, and these will also depend on other chemical and processing variables. Therefore the general principle revealed by these results should be characterized for specifics drugs and formulation conditions, for example by investigating *in vitro* release kinetics as a function of water content during self-assembly.

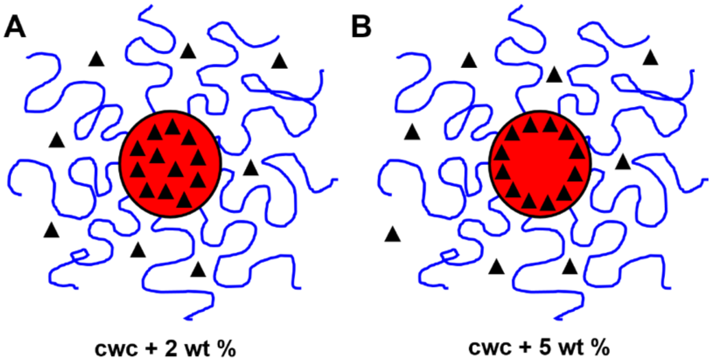

Figure 3-20. Schematic based on I_1/I_3 values showing increased localization of Py (black triangles) at the interface of the PCL core with increase in the on-chip water content from cwc + 2 wt % (A) to cwc + 5 wt % (B).

3.3. Relationships Between Fluorescence and Physicochemical Properties of Py-PNP

The results described in the previous section show that specific experimental conditions for PNP preparation can have significant effects on the microenvironment of the encapsulated molecules, both in terms of the proximity between molecules in the core (association state), reported by I_e/I_m, and their distance from the core-corona interface, reported by I_1/I_3. However, despite the obvious importance of preparation conditions, we were also interested in determining if some general trends could be determined between the Py microenvironment (I_e/I_m and I_1/I_3) and the measured physicochemical characteristics of the Py-PNPs. To do this, we use a simple linear combination approach to combine the measured Py-PNP parameters $d_{h,eff}$ (particle size) and $\mathrm{DL}_{\mathrm{core}}$ (encapsulated dye concentration in the core) within a single unitless independent variable, followed by plotting the two dependent variables I_e/I_m and I_1/I_3 against the unitless independent variable, then finally obtaining best fits with linear regression. In this exercise, we were not attempting to fit the data using physically meaningful models. Rather we were interested to determine if some general trends exist, the direction of these general trends, and whether these trends could be rationalized using a simple understanding of the system. Since we did not measure core crystallinity for all preparation conditions, we did not have sufficient data to include $\chi_{\mathrm{PCL,core}}$ in our linear combination of physicochemical Py-PNP parameters.

3.3.1. Linear Combination of Physicochemical Properties

In this section, we combine two physicochemical properties of PNPs (particle size and core loading levels) from our complete set of preparation conditions, in order to elucidate some general relationships between these properties and the core microenvironment as characterized using the Py polarity indicator ratio (I_1/I_3) and the excimer monomer ratio (I_e/I_m). The mean values of physicochemical properties (Table 3-1) and associated fluorescence properties (Table 3-2) are combined and organized to show the relationship between $d_{\mathrm{h,eff}}$, $\mathrm{DL}_{\mathrm{core}}$, and I_1/I_3 (Table 3-3), and between $d_{\mathrm{h,eff}}$, $\mathrm{DL}_{\mathrm{core}}$, and I_e/I_m (Table 3-4) for the 12 unique preparation conditions.

Using Table 3-3 and 3-4, a set of equations were formed using each conditions where the two known physicochemical parameters ($d_{\mathrm{h,eff}}$ and $\mathrm{DL}_{\mathrm{core}}$) are multiplied by a coefficient to obtain a dimensionless number with the linear combination of these dimensionless numbers equalling the corresponding Py fluorescence intensity ratio. This formed a set of 12 unique linear equations, each with two unknown coefficients

(a / nm^{-1} and b / %$^{-1}$). For instance, the two equations corresponding to condition 1 and 2 in Table 3-3 (I are as follows:

$$(143.10 \times a) + (2.36 \times b) = 1.85$$

$$(628.29 \times a) + (0.90 \times b) = 1.88$$

For each of I_1/I_3 (Table 3-3) and I_e/I_m (Table 3-4), a set of values of the unknown coefficients, a and b were solved for all possible combinations of 2 conditions from the set of 12 conditions in Excel. For each set of I_1/I_3 and I_e/I_m equations, we obtained 66 values for a and b, which were then averaged for both I_1/I_3 and I_e/I_m and used to determine the unitless independent variable $ad_{h,eff} + b\mathrm{DL}_{core}$. Plots of I_1/I_3 vs. $ad_{h,eff} + b\mathrm{DL}_{core}$ and I_e/I_m vs. $ad_{h,eff} + b\mathrm{DL}_{core}$ are plotted in Figure 3-21, A and B respectively, with best fit linear regression lines shown.

Table 3-3. Reported mean values from triplicate preparations of selected physiochemical properties for 12 unique preparation conditions and associated mean I_1/I_3 values. Associated standard errors are reported in Table 3-1 and Table 3-2.

Condition	$d_{h,eff}$ **/ nm**	**DL$_{core}$ / %**	I_1/I_3
1	140	2.4	1.85
2	630	0.90	1.88
3	480	1.4	1.89
4	160	0.20	1.86
5	70	2.1	1.87

6	55	2.5	1.87
7	37	2.7	1.78
8	85	2.0	1.79
9	55	2.50	1.77
10	55	1.7	1.83
11	170	1.40	1.83
12	67	1.50	1.82

Table 3-4. Reported mean values from triplicate preparations of selected physiochemical properties for 12 unique preparation conditions and associated mean I_e/I_3 values. Associated standard errors are reported in Table 3-1 and Table 3-2.

Condition	**$d_{h,eff}$ / nm**	**DL_{core} / %**	**I_e/I_m**
1	140	2.4	0.56
2	630	0.90	0.17
3	480	1.4	0.42
4	160	0.20	0.43
5	70	2.1	0.91
6	55	2.5	0.68
7	37	2.7	0.65
8	85	2.0	0.58
9	55	2.50	0.65
10	55	1.7	0.61
11	170	1.40	0.68
12	67	1.50	0.77

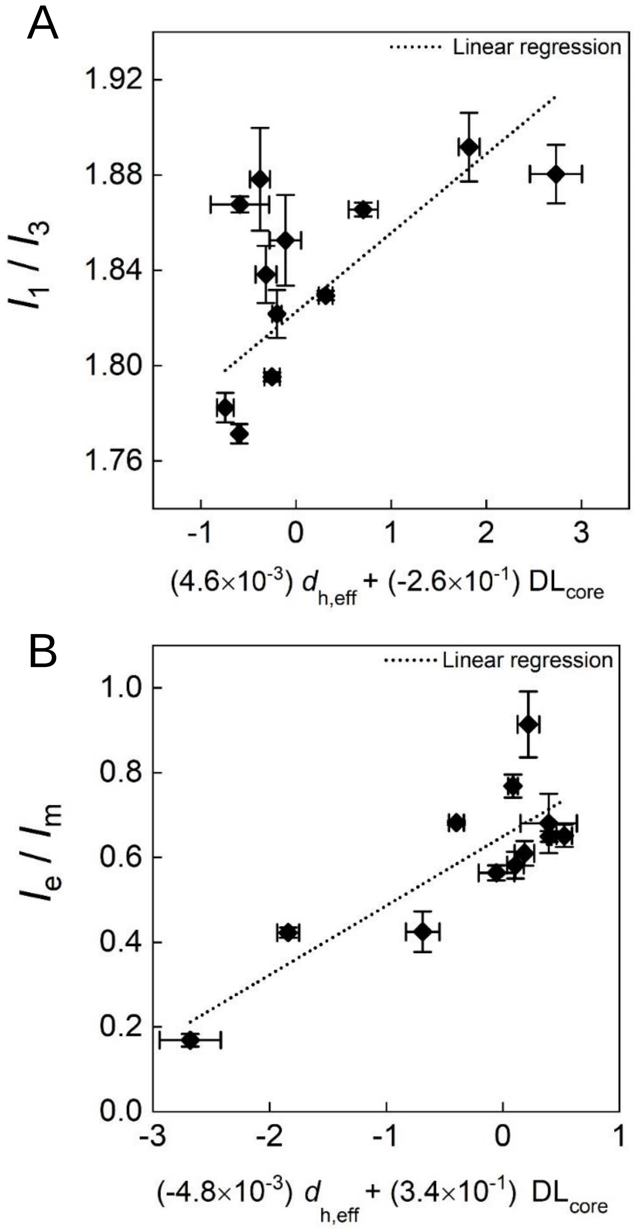

Figure 3-21. Effect of linear combinations of physicochemical properties $d_{\mathrm{h,eff}}$ and $\mathrm{DL}_{\mathrm{core}}$ on fluorescence properties I_1/I_3 (A) and I_e/I_m (B). Dotted lines indicate best fit linear trend lines.

3.3.2. Discussion of Plots of Fluorescence Ratios vs. Linear Combinations of Physicochemical Properties

For the plot of I_1/I_3 vs. $ad_{\mathrm{h,eff}} + b\mathrm{DL}_{\mathrm{core}}$ shown in Figure 3-21A, the determined a and b coefficients for $d_{\mathrm{h,eff}}$ and $\mathrm{DL}_{\mathrm{core}}$ were positive and negative values, respectively.

Since the resulting trend line gives a positive slope, these coefficients suggest that I_1/I_3 generally increases with increasing $d_{\mathrm{h,eff}}$ and that I_1/I_3 generally decreases with increasing $\mathrm{DL}_{\mathrm{core}}$. However, we note that the goodness of fit is very poor ($r^2 = 0.29$), suggesting that these general trends are probably not reliable nor physically meaningful. It is not surprising that we see poor correlation between I_1/I_3 and measured physicochemical properties, given that we have shown in the previous section that I_1/I_3 is highly dependent on various experimental variables for PNP preparation, with trends that generally do not track with corresponding trends in $d_{\mathrm{h,eff}}$ and $\mathrm{DL}_{\mathrm{core}}$. This suggests that the interfacial localization of encapsulated molecules within PNPs cannot be reliably predicted based on conventional, non-fluorescence measurements.

For the plot of I_e/I_m vs. $ad_{\mathrm{h,eff}} + b\mathrm{DL}_{\mathrm{core}}$ shown in Figure 3-21B, the determined a and b coefficients for $d_{\mathrm{h,eff}}$ and $\mathrm{DL}_{\mathrm{core}}$ were negative and positive values, respectively. Since the resulting trend line gives a positive slope, these coefficients suggest that I_e/I_m generally decreases with increasing $d_{\mathrm{h,eff}}$ and that I_e/I_m generally increases with increasing $\mathrm{DL}_{\mathrm{core}}$. We note that the goodness of fit is fair ($r^2 = 0.7$), suggesting that these general trends may be somewhat reliable for predicting the direction of changes in the association state of encapsulated molecules. The determined trend directions also appear physically reasonable: higher $\mathrm{DL}_{\mathrm{core}}$ values will result in higher concentrations of molecules in the core and therefore shorter mean distances between molecules; larger particle sizes (higher $d_{\mathrm{h,eff}}$ values) will provide greater encapsulation volumes and therefore longer mean distances between molecules. However, as described in the previous section, like I_1/I_3, I_e/I_m is highly dependent on various experimental variables for PNP preparation, with trends that do not always track with corresponding trends in

$d_{h,eff}$ and DL_{core}. Therefore, in the absence of fluorescence data, we believe that, taken together, $d_{h,eff}$ and DL_{core} could serve as a general predictor for changes in the association state of encapsulated molecules, but not a completely reliable one. Overall, our results indicate the molecular-level features of drug-loaded PNPs, including the association state and interfacial localization of encapsulated molecules, cannot be reliably predicted based on conventional physicochemical data, such that the effects of these molecular-level features on drug delivery properties, including release rates, should be carefully considered when selecting formulation conditions.

3.5. References

(1) Kumar, V.; Adamson, D. H.; Prud'homme, R. K. Fluorescent Polymeric Nanoparticles: Aggregation and Phase Behavior of Pyrene and Amphotericin B Molecules in Nanoparticle Cores. *Small* **2010**, *6* (24), 2907–2914.

(2) Bains, A.; Cao, Y.; Moffitt, M. G. Multiscale Control of Hierarchical Structure in Crystalline Block Copolymer Nanoparticles Using Microfluidics. *Macromol. Rapid Commun.* **2015**, *36* (22), 2000–2005.

(3) Mai, Y.; Eisenberg, A. Self-Assembly of Block Copolymers. *Chem. Soc. Rev.* **2012**, *41* (18), 5969–5985.

(4) Allen, C.; Maysinger, D.; Eisenberg, A. Nano-Engineering Block Copolymer Aggregates for Drug Delivery. *Colloids Surf. B Biointerfaces* **1999**, *16* (1), 3–27.

(5) Zhang, L.; Eisenberg, A. Multiple Morphologies and Characteristics of "Crew-Cut" Micelle-like Aggregates of Polystyrene-b-Poly(Acrylic Acid) Diblock Copolymers in Aqueous Solutions. *J. Am. Chem. Soc.* **1996**, *118* (13), 3168–3181.

(6) Bains, A.; Moffitt, M. G. Effects of Chemical and Processing Variables on Paclitaxel-Loaded Polymer Nanoparticles Prepared Using Microfluidics. *J. Colloid Interface Sci.* **2017**, *508*, 203–213.

(7) Du, Z.-X.; Xu, J.-T.; Fan, Z.-Q. Regulation of Micellar Morphology of PCL-b-PEO Block Copolymers by Crystallization Temperature. *Macromol. Rapid Commun.* **2008**, *29* (6), 467–471.

(8) Cowie, J. M. G.; Arrighi, V. The Crystalline State and Partially Ordered Structures. In *Polymers*; CRC Press, 2007.

(9) Cowie, J. M. G.; Arrighi, V. *Polymers: Chemistry and Physics of Modern Materials, Third Edition*, 3rd ed.; CRC Press: Boca Raton, 2007.

(10) Kalyanasundaram, K.; Thomas, J. K. Environmental effects on Vibronic Band Intensities in Pyrene Monomer Fluorescence and their application in studies of Micellar Systems, *Journal of the American Chemical Society*, **1977**, *99(7)*, 2039-2043.

(11) Birks, J. B. Photophysics of Aromatic Molecules. **1970**.

(12) Dong, D. C.; Winnik, M. A. The Py Scale of Solvent Polarities. *Can. J. Chem.* **1984**, *62* (11), 2560–2565.

(13) Glushko, V.; Thaler, M. S. R.; Karp, C. D. Pyrene Fluorescence Fine Structure as a Polarity Probe of Hydrophobic Regions: Behavior in Model Solvents. *Arch. Biochem. Biophys.* **1981**, *210* (1), 33–42.

(14) Bains, A.; Cao, Y.; Kly, S.; Wulff, J. E.; Moffitt, M. G. Controlling Structure and Function of Polymeric Drug Delivery Nanoparticles Using Microfluidics. *Mol. Pharm.* **2017**, *14* (8), 2595–2606.

(15) Rizis, G.; Ven, T. G. M. van de; Eisenberg, A. Crystallinity-Driven Morphological Ripening Processes for Poly(Ethylene Oxide)-Block-Polycaprolactone Micelles in Water. *Soft Matter* **2014**, *10* (16), 2825–2835.

(16) Bains, A.; Wulff, J. E.; Moffitt, M. G. Microfluidic Synthesis of Dye-Loaded Polycaprolactone-Block-Poly(Ethylene Oxide) Nanoparticles: Insights into Flow-Directed Loading and in Vitro Release for Drug Delivery. *J. Colloid Interface Sci.* **2016**, *475*, 136–148.

(17) Wang, C.-W.; Bains, A.; Sinton, D.; Moffitt, M. G. Flow-Directed Loading of Block Copolymer Micelles with Hydrophobic Probes in a Gas–Liquid Microreactor. *Langmuir* **2013**, *29* (26), 8385–8394.

(18) Wang, C.-W.; Sinton, D.; Moffitt, M. G. Morphological Control via Chemical and Shear Forces in Block Copolymer Self-Assembly in the Lab-on-Chip. *ACS Nano* **2013**, *7* (2), 1424–1436.

(19) Wang, C.-W.; Sinton, D.; Moffitt, M. G. Flow-Directed Block Copolymer Micelle Morphologies via Microfluidic Self-Assembly. *J. Am. Chem. Soc.* **2011**, *133* (46), 18853–18864.

(20) Xu, Z.; Lu, C.; Riordon, J.; Sinton, D.; Moffitt, M. G. Microfluidic Manufacturing of Polymeric Nanoparticles: Comparing Flow Control of Multiscale Structure in Single-Phase Staggered Herringbone and Two-Phase Reactors. *Langmuir* **2016**, *32* (48), 12781–12789.

(21) Cao, Y.; Silverman, L.; Lu, C.; Hof, R.; Wulff, J. E.; Moffitt, M. G. Microfluidic Manufacturing of SN-38-Loaded Polymer Nanoparticles with Shear Processing Control of Drug Delivery Properties. *Mol. Pharm.* **2019**, *16* (1), 96–107.

(22) Elsabahy, M.; Wooley, K. L. Design of Polymeric Nanoparticles for Biomedical Delivery Applications. *Chem. Soc. Rev.* **2012**, *41* (7), 2545–2561.

(23) Cai, S.; Vijayan, K.; Cheng, D.; Lima, E. M.; Discher, D. E. Micelles of Different Morphologies—Advantages of Worm-like Filomicelles of PEO-PCL in Paclitaxel Delivery. *Pharm. Res.* **2007**, *24* (11), 2099–2109.

(24) Geng, Y.; Dalhaimer, P.; Cai, S.; Tsai, R.; Tewari, M.; Minko, T.; Discher, D. E. Shape Effects of Filaments versus Spherical Particles in Flow and Drug Delivery. *Nat. Nanotechnol.* **2007**, *2* (4), 249–255.

Chapter 4 Conclusions and Future Directions

4.1. Conclusions

In this thesis, we investigated the effect of chemical and processing variables on the internal structure of pyrene-loaded, biocompatible, and semicrystalline PCL-b-PEO nanoparticles (Py-PNPs) prepared in a two-phase segmented microfluidic reactor. Fluorescence properties of pyrene provide an additive advantage over the conventional characterization techniques as they extract important molecular scale information which are sensitive to changes in the confined local environment (such as polarity, microviscosity, diffusion, binding affinity) surrounding the encapsulated pyrene molecules.[1–6] The steady-state emission spectra of pyrene provided two important fluorescence intensity ratios; I_1/I_3 that is sensitive to polarity of local environment (values of 1.87 in water and 0.58 in hexane) and I_e/I_m that monitors the formation of excimer in the confined core microenvironment.[3,7,8] We evaluate pyrene fluorescence intensity ratios under the action of different preparation conditions to demonstrate their influence on the internal structure, microenvironment, loading and distribution of encapsulated pyrene molecules. Moreover, we went a step further by combining all datasets obtained from the different preparation conditions to establish general relationships between physicochemical properties of Py-PNPs, including mean effective hydrodynamic diameters, $d_{h,eff}$ and drug loading of the PCL core, DL_{core}, to the Py fluorescence ratios (I_1/I_3 and I_e/I_m). This was achieved by determining the dependence of I_1/I_3 and I_e/I_m on linear combinations of $d_{h,eff}$ and DL_{core}.

One aspect of the changing microenvironment tested in this thesis is the influence of chemical and processing variables on the pyrene fluorescence intensity ratios. In chapter 3, we specifically studied the effects of PCL block length, initial Py:copolymer loading ratio, r_{Py}, on-chip water content, and microfluidic flow rate, Q on the pyrene fluorescence intensity ratios and physicochemical properties of PNPs. Firstly, we demonstrated the effect of PCL block lengths on the hydrodynamic size, loading and core microenvironment characteristics. In this case, we obtained non-monotonic trends (an increase followed by a decrease) for the majority of PNP characteristics which also followed with pyrene fluorescence intensity ratios except for PCL core crystallinity. These changes were attributed to morphological transition of nanoparticles, from smaller diameter structures (spheres), to formation of larger hydrodynamic diameter but a lower internal curvature structures (cylinders and vesicles) at longer core block lengths.[9] It was also noted that PCL2.1k block copolymer had the highest local Py concentration ($\mathrm{DL}_{\mathrm{core}}$) which also followed with the largest Py association in the PNP core (I_e/I_m). On the other hand, the polarity of microenvironment exhibited a monotonic increase of average I_1/I_3 values which were found to be insignificant, i.e., falling within experimental error.

Next, we explored the effect of initial Py:copolymer loading ratio, r_{Py}, which revealed clear impacts on the particle size, dye loading and internal microenvironment characteristics. In this case, the increase in added Py molecules during the self-assembly process, acted as plasticizer, leading to a decrease in particle size and increase in particle size distribution as tracked by polydispersity (PDI).[9] Interestingly, the increase in pyrene loading ratio (r_{Py}), however, didn’t impact the loading efficiency of pyrene as the PNP core was saturated with encapsulated pyrene concentration. More importantly, even though the PNP core was saturated with pyrene concentration, we observed more close associations of pyrene molecules (I_e/I_m) at higher r_{Py}. This an illustration showing that the internal microenvironment changes can sometimes be independent of observed physicochemical properties of PNPs.

Next, we investigated the effect of on-chip water content which showed another illustration of the difference between the local environment of Py molecules and average Py-PNP properties. In this study, we expected that increase in water content would be driving force for increase in encapsulation of hydrophobic molecules such as pyrene.[10] Contrastingly, the dye loading results showed a steady decrease in core pyrene concentration with increase in water content from *cwc* + 2.0 wt% to *cwc* + 5.0 wt%. For this case, we observed interesting feature for Py-PNPs at cwc + 5.0 wt%; even though pyrene concentration (DL_{core}) decreased, contrary to this, we observed an increase in pyrene association in PNP core. These non-monotonic trends observed with changing solvent compositions was the result of competition between thermodynamic driving force and kinetics of polymer chains and molecules during the self-assembly process.[10] The kinetic effect was found to be dominating at higher water contents that may have impacted the diffusion of encapsulated pyrene within the core of PNPs, leading to decrease in pyrene association.

The microfluidic flow rate investigations showed a complex interplay of shear induced effects on the particle size, loading and microenvironment characteristics.[10] TEM characterization of Py-PNP prepared at different flow rates showed interplay of three shear induced mechanisms: shear induced coalescence, shear induced crystallization and shear induced breakup of particles.[9,11–13] The increase in flow rate from Q = 50 μL/min to Q = 100 μL/min, lead to shear induced coalescence and shear induced crystallization of PNPs which is tracked by increase in formation of filaments, particle size, core crystallinity and steady increase in Py excimer formation. It was interesting to observe that not only does shear rate inside the microfluidic reactor impacts the multiscale features of PNPs but also modulates the internal structure characteristics. However, an increase in flow rate from Q = 100 μL/min to Q = 200 μL/min showed that PNP structural properties were dictated by the dominating shear-induced breakup mechanisms that lead to formation particles of various morphologies (such as spheres, cylinders and lamellae) marked by a decrease in particle size. It was interesting to note that even though the shear induced breakup mechanisms were dominating, they still lead to increase in pyrene excimer concentration.

All these results show that experimental variables which can be fine-tuned to control the structural properties of PNPs does impact both the physicochemical properties of PNPs and the molecular-level microenvironment of the encapsulated pyrene species. Specifically, differences in the I_e/I_m ratio indicated the differences in the mean distance between encapsulated pyrene within the PNP core. Whereas, the changes in the I_1/I_3 ratio indicate changes in the microenvironment polarity, interpreted in terms of the relative distance of encapsulated pyrene from the more polar regions to less polar regions. For our case, we assume that the core-corona interface (PCL-PEG) is more water accessible (more polar) than the PCL core center (less polar). The association and partitioning of encapsulated molecules can have a big say on the properties of drug delivery PNPs, for instance, in terms of their release profiles, in-vitro and in-vivo efficacies. Thus, this information is vital for the design of effective drug delivery nanocarriers.

In the later sections of Chapter 3, we combine all the datasets from the various preparation conditions to find a simple linear combination approach correlating the structural properties ($d_{h,eff}$, DL_{core}) with the pyrene fluorescence intensity ratios (I_e/I_m and I_1/I_3). This was achieved by forming a linear combination of a $d_{h,eff}$ + b DL_{core} to obtain a dimensionless number which is plotted against the unitless independent variable. For the plot of I_1/I_3 vs. a $d_{h,eff}$ + b DL_{core}, the determined a and b coefficients were positive and negative values, respectively. This showed that the polarity of microenvironment would generally increase with particle size but decrease with loading of pyrene. Since, the correlation coefficient or goodness of fit was poor (r^2 = 0.29), it is not possible to associate these general trends to track the changing polarity of microenvironment (I_1/I_3). The preparation condition studies also corroborated that I_1/I_3 is generally does not track with corresponding trends in $d_{h,eff}$ and DL_{core}. On the other hand, the plot of I_e/I_m vs. a $d_{h,eff}$ + b DL_{core} exhibited negative value for coefficient a and positive value for coefficient b. Since the goodness of fit is fair for this plot (r2 = 0.7), this suggests that that I_e/I_m generally decreases with increasing $d_{h,eff}$ and that I_e/I_m generally increases with increasing DL_{core}. Overall, these linear combination results indicate the molecular-level features of drug-loaded PNPs, including the association state and interfacial localization of encapsulated molecules, cannot be reliably predicted based on conventional physicochemical data.

4.2. Future Directions

This thesis provided an insight onto the correlations between the physicochemical properties of PNPs and the changing microenvironment surrounding encapsulated hydrophobic molecules. In some cases, namely the effect of PCL block length and microfluidic flow rate, we could observe a correlation of the fluorescence ratios I_e/I_m and I_1/I_3 in agreement with the physicochemical properties such as concentration of encapsulated Py, DL_{core}. On the other hand, for experimental variables that affect the molecular interactions of Py molecules during self-assembly, the fluorescence ratios I_e/I_m and I_1/I_3 showed significant variations that were independent of variations in DL_{core}.

We believe these are important observations, as they indicate that some chemical and processing variables can track information of the variations in the partitioning and association of encapsulated drug molecules. whereas other variables may be completely independent of the information about changes in the spatial distribution of encapsulated drug molecules. For the later type of variables, we need to determine the effect of partitioning and association of loaded molecules by further testing such as *in vitro* drug release studies, cell culture studies, or *in vivo* experiments. A typical in-vitro drug release tracks the release of encapsulated drug from PNPs in physiological conditions (37 ^{0}C) along with 1% PBS and albumin buffer.[9,11] These experiments can be used to understand the association of molecules with the core of PNPs, tracked by slower diffusion of higher affinity/ binding molecules and faster diffusion of lower affinity/binding molecules. Although release kinetics in such in vitro experiments have been shown to be very different from in vivo pharmacokinetics, they provide useful information on drug diffusion and nanoparticle breakup that may contribute to drug release in pharmaceutical applications.

In perspective of future studies to developing more fundamental understanding of core microenvironment of Py-PNPs, it can be achieved by utilizing time-resolved measurements and/or fluorescence quenching studies. These studies have been used to provide more detailed information on the molecular dynamics, distribution, partitioning and mechanism of excimer formation for encapsulated pyrene. In addition, there are other interesting fluorescent probes (DPH, Cyanine, etc.) that have been used because of their unique steady-state emission spectra and its sensitivity to changes in the local surrounding environment.

4.3. References

(1) Williams, D. E.; Dolgopolova, E. A.; Pellechia, P. J.; Palukoshka, A.; Wilson, T. J.; Tan, R.; Maier, J. M.; Greytak, A. B.; Smith, M. D.; Krause, J. A.; Shustova, N. B. Mimic of the Green Fluorescent Protein β-Barrel: Photophysics and Dynamics of Confined Chromophores Defined by a Rigid Porous Scaffold. *J. Am. Chem. Soc.* **2015**, *137* (6), 2223–2226.

(2) Abraham, S.; Weiss, R. G. Photochemical and Photophysical Studies of and in Bulk Polymers. In *Supramolecular Photochemistry*; John Wiley & Sons, Ltd, 2011; pp 443–516.

(3) Glushko, V.; Thaler, M. S. R.; Karp, C. D. Pyrene Fluorescence Fine Structure as a Polarity Probe of Hydrophobic Regions: Behavior in Model Solvents. *Archives of Biochemistry and Biophysics* **1981**, *210* (1), 33–42.

(4) Kumar, V.; Adamson, D. H.; Prud'homme, R. K. Fluorescent Polymeric Nanoparticles: Aggregation and Phase Behavior of Pyrene and Amphotericin B Molecules in Nanoparticle Cores. *Small* **2010**, *6* (24), 2907–2914.

(5) Zhao, J.; Allen, C.; Eisenberg, A. Partitioning of Pyrene between "Crew Cut" Block Copolymer Micelles and H2O/DMF Solvent Mixtures. *Macromolecules* **1997**, *30* (23), 7143–7150.

(6) Wu, T.; Oake, J.; Liu, Z.; Bohne, C.; Branda, N. R. Probing the Microenvironments in a Polymer-Wrapped Core–Shell Nanoassembly Using Pyrene Chromophores. *ACS Omega* **2018**, *3* (7), 7673–7680.

(7) Kalyanasundaram, K.; Thomas, J. K. Environmental effects on Vibronic Band Intensities in Pyrene Monomer Fluorescence and their application in studies of Micellar Systems, *Journal of the American Chemical Society*, **1977**, *99(7)*, 2039-2043.

(8) Dong, D. C.; Winnik, M. A. The Py Scale of Solvent Polarities. *Can. J. Chem.* **1984**, *62* (11), 2560–2565.

(9) Bains, A.; Cao, Y.; Kly, S.; Wulff, J. E.; Moffitt, M. G. Controlling Structure and Function of Polymeric Drug Delivery Nanoparticles Using Microfluidics. *Mol. Pharmaceutics* **2017**, *14* (8), 2595–2606.

(10) Mai, Y.; Eisenberg, A. Self-Assembly of Block Copolymers. *Chem. Soc. Rev.* **2012**, *41* (18), 5969–5985.

(11) Bains, A.; Wulff, J. E.; Moffitt, M. G. Microfluidic Synthesis of Dye-Loaded Polycaprolactone-Block-Poly(Ethylene Oxide) Nanoparticles: Insights into Flow-Directed Loading and in Vitro Release for Drug Delivery. *Journal of Colloid and Interface Science* **2016**, *475*, 136–148.

(12) Wang, C.-W.; Bains, A.; Sinton, D.; Moffitt, M. G. Flow-Directed Loading of Block Copolymer Micelles with Hydrophobic Probes in a Gas–Liquid Microreactor. *Langmuir* **2013**, *29* (26), 8385–8394.

(13) Wang, C.-W.; Sinton, D.; Moffitt, M. G. Flow-Directed Block Copolymer Micelle Morphologies via Microfluidic Self-Assembly. *J. Am. Chem. Soc.* **2011**, *133* (46), 18853–18864.